Rheology and Microfluidic flows of a cationic surfactant and hydrotropic salt mixture

Ya Zhao

A dissertationsubmitted in partial fulfillment of the
requirements for the degree of

Doctor of Philosophy

University of Washington

2016

Reading Committee:

Amy Q. Shen, Chair

George M. Homsy

Dayong Gao

Junlan Wang

Program Authorized to Offer Degree:
Mechanical Engineering

University of Washington

Abstract

Rheology and Microfluidic flows of a cationic surfactant and hydrotropic salt mixture

Ya Zhao

Chair of the Supervisory Committee:
Associate professor Amy Q. Shen

The widespread use of wormlike micellar solutions is commonly found in household items such as cosmetic products, industrial fluids used in enhanced oil recovery and as drag reducing agents, and in biological applications such as drug delivery and biosensors. Despite their extensive use, there are still many details about the microscopic micellar structure and the mechanisms by which wormlike micelles form under flow that are not clearly understood. We focused on studying an aqueous micellar solutions of cationic surfactant cetyltrimethylammonium bromide (CTAB) and organic hydrotropic salt 3-hydroxy naphthalene-2-carboxylate (SHNC), including linear and nonlinear rheological characterizations, flow instabilities of CTAB/SHNC solution around microfluidic cylinders. The strong hydrophobicity and naphthalene structure present in the SHNC induces significant growth of CTAB wormlike micelles and promotes stable micellar network formation. We correlated its rich rheological behavior with structural transitions of the micelle network under different deformation histories and temperature variations. Since microfluidic devices provide a versatile platform to study wormlike micellar solutions under various flow conditions and confined geometry, we are able to showcase that the influence of spatial confinement and moderate hydrodynamic forces present in the microfluidic device can give rise to a host of possibilities of microstructural rearrangements and interesting flow phenomena.

TABLE OF CONTENTS

LIST OF FIGURES

GLOSSARY

CTAB: cationic surfactant cetyltrimethylammonium bromide.

SHNC: organic hydrotropic salt 3-hydroxy naphthalene-2-carboxylate.

NASAL: organic salt sodium salicylate, with one benzene ring along with the salt.

WLM: wormlike micelles.

LAOS: large amplitude oscillatory shear flow.

FIB: Flow induced birefringence.

μ-PIV: Micron particle image velocimetry.

FISP: Flow induced structured phase.

η_0: Zero shear viscosity.

σ_P: Plateau shear stress.

G'_∞: Plateau modulus.

ACKNOWLEDGMENTS

Firstly, I would like to express my sincere gratitude to my advisor Prof. Shen for the continuous support of my Ph.D study and related research, for her patience, motivation, and immense knowledge. Her guidance helped me in all the time of research and writing of this thesis. I could not have imagined having a better advisor and mentor for my Ph.D study.

Besides my advisor, I would like to thank the rest of my thesis committee: Prof. Gao, Prof. Wang, Prof. Homsy and Prof. Cao, for their insightful comments and encouragement, which encouraged me to widen my research from various perspectives. I also want to thank Dr. Simon Haward, for his generous help on my experiments and understanding of complex fluids.

Last but not the least, I would like to thank my parents for supporting me throughout writing this thesis and my life in general.

Chapter 1

OVERVIEW OF WORMLIKE MICELLES UNDER DIFFERENT FLOW FIELDS

Surfactants are amphiphilic molecules that consist of a bulk hydrophilic head group, which can be neutrally, positively, or negatively charged, and a hydrophobic tail. When the surfactant concentration is increased above a critical micelle concentration (CMC), surfactant monomers will spontaneously self-assemble into large aggregates known as micelles (in aqueous solutions) to shield the hydrophobic tails from water[11]. The morphological variations of these micelles are dependent on the temperature, pH, concentration, salinity, surfactant packing parameter, and flow conditions. Wormlike micelles are characterized as cylindrically elongated and semi-flexible aggregates. For example, cationic surfactants such as hexadecyltrimethylammonium bromide (CTAB) or cetylpyridinium chloride (CPyCl) in aqueous solutions can form wormlike micelles under specific temperatures and concentrations. The addition of inorganic salts, such as sodium chloride (NaCl) and sodium nitrate ($NaNO_3$), or strongly binding counterions such as organic salt sodium salicylate (NaSal), have shown to considerably reduce the CMC. These salts serve to screen electrostatic repulsion of neighboring charged hydrophilic headgroups in the aqueous solution and result in a steep increase of the shear viscosity, which can be correlated with the transition from spherical to wormlike micelles in the surfactant solution[12–14]. The characteristic length scale, flexibility, and interaction between wormlike micelles largely depend on the chemical nature and concentrations of surfactants and salts[11,15–19].

Wormlike micelles are commonly found as additives in consumer hair products, drag reduction agents, and fracture fluids in oil and gas productions[20–23] because of their viscoelastic and gel-like properties[12–14,24–28]. The size and shape of wormlike micelles bear

striking similarities to those of polymer chains but with larger diameters (1∼10 nm) and longer persistence lengths (10∼100 nm)[29–31]. Thus, wormlike micelles have also been referred to as living polymers because they resemble micron sized polymeric chains weakly held together by physical interactions that constantly undergo scission and recombination. Cates' model[32], which assumes that a wormlike micellar chain can break and recombine with equal probability, predicts that the stress relief in the wormlike chains can be accomplished by brownian motion driven reptation, and reforming new end caps if the micelles break and reform faster than their reptation time scale. The linear viscoelastic response of these wormlike micellar solutions can be described by the Maxwell model that characterizes fluid viscosity and elasticity as a spring and dashpot. Shikata et al.[33–35] characterized wormlike micellar solutions as either linear and partly entangled or highly entangled and branched micellar networks. They observed that the weakly interacting and short wormlike micellar system could be described by the Cates' model (with reversible chain recombination and scission)[32]. However, when a considerably stable and longer micellar network is formed (i.e., an equal molar CTAB:NaSal system), the micelles become too long and stable to reptate. Instead, the micelles exhibit scission and recombination at their entanglement points, with Sal^- ions serving as catalysts[33,35]. By using both traditional bulk rheometry and microfluidic approaches[2,3,5,36–46], the study of wormlike micellar solutions under flow has been ongoing for the past few decades with increasing understanding of their linear and non-linear rheological behavior, microstructural transitions, and higher-ordered structural formations under various external conditions (see reviews[20,47–54]).

Microfluidics has emerged in recent years as a versatile method of handling fluids at small length-scales, in particular, for generating and manipulating complex fluids with controllable size, tailored structure and functionality[55,56]. Microfluidics has been employed to study effects of confined geometry on fiber deformations[57], dynamics of DNA molecules[58,59], and bacteria motion[60–62] at low-Reynolds numbers (see reviews on microfluidics and their applications in[63–65]). More recently, microfluidic systems have been exploited as microfluidic-rheometers[3,38–41,43–46,66] or as tools to study and generate new microstructures and new flow

phenomena[3,7,38–41,43–46,67–71]. Traditional shear rheometry, with typical rheometer gap sizes at least one order of magnitude greater than the intrinsic length scale of the material microstructure, is generally used for measuring fluid responses to shear with gap sizes of O(1 mm) and deformation rates in the range of O($10^2 \sim 10^3$ s^{-1})[41,45,46]. Although rheometers with parallel plate geometries and gap sizes in the range of $10 \sim 500$ μm can be used to access high deformation rates (up to 10^2 s^{-1}), it requires careful alignment of the plates and identifying zero gap error[36,37]. Additionally, when the deformation rate reaches 10^4 s^{-1} or higher, complications with edge fracture, secondary flow, and viscous heating become significant for complex fluids[41,45,46,66]. By taking advantage of the micron length scales present in microfluidics, higher deformation rates ($\geq 10^5$ s^{-1}) can easily be achieved with negligible inertial or viscous heating effects[46]. A comprehensive review of microfluidic rheometry on capillary, stagnation, and contraction flows has been reported by Pipe and Mckinley[45,46]. A complementary review on extensional flow fields within the context of microfluidic rheometry can be found in Galindo et al.[72]. In addition, microfluidics have recently been used to probe the influence of spatial confinement on wormlike micelles[3,7,38–41,43–46,68–71] and to provide a robust and efficient path to study the flow of wormlike micelles in geometries similar to the ones found in porous media flow, oil recovery, and drug delivery applications[7,8,70,71,73–76].

1.1 Wormlike micelles under shear flows

1.1.1 Shear banding of wormlike micellar solutions in Couette flow

Under simple shear flow, such as in a Couette Cell shown in Fig. 1.1(A), homogeneous flow of wormlike micellar solutions can become unstable and separate into coexisting shear bands with different local viscosities and internal structures[30,77,78], above a critical shear rate or shear stress $\dot{\gamma}_1$. Rehage and Hoffmann[30] first reported the rheological behavior of the stress plateau in reversible giant wormlike micellar solutions experimentally with the micelles being slightly oriented and maintained homogeneous when $\dot{\gamma} < \dot{\gamma}_1$. When $\dot{\gamma}_1 < \dot{\gamma} < \dot{\gamma}_2$, the flow becomes unstable with two stable branches containing different viscosities coexisting

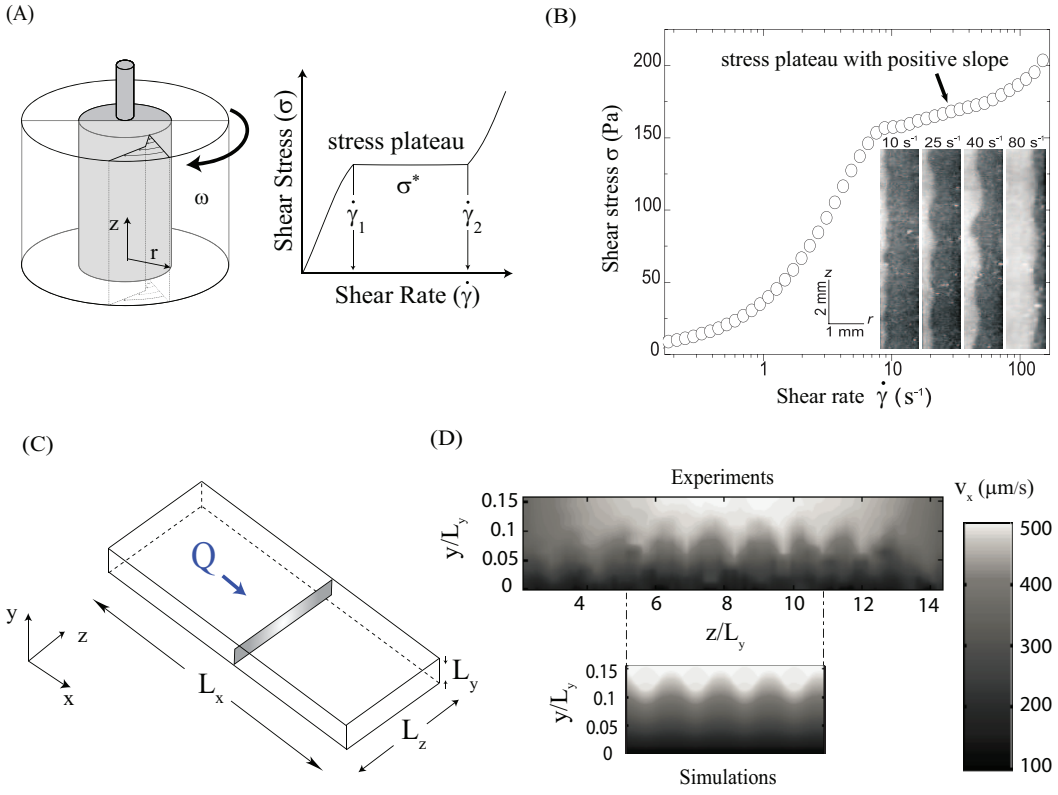

Figure 1.1: (A) Schematic of shear banding flow in a Couette cell and the corresponding shear stress versus shear rate curve; (B) Plot of shear stress σ versus shear rate $\dot{\gamma}$ of wormlike micellar solutions in a Couette flow (adapted from Fardin et al.[1]), the inserted images are snapshots of interfacial instabilities of shear bands at different shear rates in the $r-z$ section of the Couette cell; (C) Schematic of microchannel showing the channel height (L_y), a typical ($L_y \times L_z$) cross-section for particle image velocimetry shown in Fig. 1.1(D), where y direction is perpendicular to the horizontal plane, and z is along the vorticity direction; (D) Instability image of shear bands in a straight microchannel (adapted from Nghe et al.[2]). The upper gray scale in the image shows velocity component v_x in the channel cross sections ($y-z$ plane) where the instability is fully developed. The bottom image is the corresponding snapshot of numerical simulations of the fully developed flow pattern at the same position of the microchannel.

at the constant stress σ^* regime. When $\dot{\gamma} > \dot{\gamma_2}$, a homogeneous fluid phase is recovered and the micelles are again strongly aligned in the flow direction. Macroscopic rheology coupled with the local measurements such as nuclear magnetic resonance[79,80], dynamic light scattering[81], PIV[82], high frequency ultrasonic velocimetry[83,84], rheo-optics[54] and other techniques[1,48,78,85–98] have been widely used to explore the complex dynamics of the internal structure of the fluid and flow at the shear plateau regime. For example, employing a shear rheometer coupled with flow birefringence and small angle neutron scattering (SANS), Cappelaere et al.[78] showed an isotropic to nematic phase transition of a CTAB based wormlike micellar system under shear flow, by spatially resolved the shear bands in the flow-vorticity plane and convoluted across the structures of both bands. Liberatore et al.[93,99] probed the microstructure evolution of similar CTAB based shear banding solutions in a Couette cell, by using a combination of dynamic rheology, rheo-optics, and small angle neutron scattering (SANS). Compared with the results from Cappelaere et al.[78], spatially-resolved SANS measurements in the flow-gradient plane provided more insights towards both segment orientation and degree of alignment of micelles in low and high shear bands. Subsequently, Helgeson et al.[100,101] used the same shear cell SANS setup to study two CTAB solutions with similar values of λ_0, G_0, and ξ, one shear thinning (15.6 wt% CTAB in D_2O) and one shear banding (16.7 wt% CTAB in D_2O). In contrast to a weak distortion of scattering patterns in the non shear banding system, a high degree of scattering anisotropy was observed in the shear banding solution after reaching a critical shear rate. By quantitatively coupling anisotropy data with the Giesekus constitutive model with stress diffusion, Helgeson et al. proposed a critical anisotropic parameter α that corresponded to the critical level of segment orientation and alignment required for shear banding. Berret et al.[85–87] also observed the isotropic to nematic phase transition induced by shear flow in CPyCl/NaSal in 0.5M NaCl aqueous solution with the surfactant CPyCl concentration ranging from 1% to 30% by bulk rheometry. They proposed that the characteristic transient behavior in the coexisting isotropic/nematic region was driven by nucleation and one-dimensional growth process in different phase branches after the onset $\dot{\gamma}$ of shear banding, which could be validated by

Spenley and Cates' theoretical predictions[102]. For dilute or semidilute surfactant solutions in which concentrations are smaller than the phase transition regime, the shear induced phase transitions are unlikely to happen in the system[82]. Instead, a more viscous (less aligned but more entangled micelles) and a more fluidic phase (more aligned micelles and less viscous) of different viscosities coexist when $\dot{\gamma}_1 < \dot{\gamma} < \dot{\gamma}_2$, accompanied by complex spatio-temporal dynamics in the heterogeneous structures. This is the phenomenon we are going to discuss in detail next.

Fluctuations in concentration and orientation between the adjacent shear bands have been demonstrated in experimental studies in a macroscale Couette cell geometry[1,82,94,95,97,98,103]. Miller and Rothstein[94] used a Couette cell to capture the spatial and temporal existence of shear bands with μ-PIV in both steady and start-up flows with aqueous CPyCl:NaSal:NaCl solutions at four different concentrations. Point-wise FIB was also applied to study the onset of shear banding and visualize the evolution of diffusive deformation and orientation of micelles at the shear band interface. These FIB images[94] were resolved at short time scales ($\sim$ 1 s or less) which suggested the existence of dynamic elastic waves affecting the undulation of the interface within the shear bands. Fardin et al.[1,95,97,98,103] experimentally studied the dynamics of shear bands in the flow vorticity (θ-z) and velocity gradient (r-z) planes by using particle image velocimetry (PIV) in a transparent Couette cell, for a semi-dilute aqueous wormlike micellar solution containing 11wt% CTAB and 0.405M $NaNO_3$. Fig. 1.1(B) shows a shear stress plateau with a positive slope obtained for the solution under steady state shear flow in a Couette cell[1]. Along the positive stress plateau, shear bands were generated with an undulating interface along the vorticity direction. The inset in Fig. 1.1(B) are snapshots taken along $(r-z)$ plane at various times. Fardin et al.[1] observed that at $\dot{\gamma} = 40\ \mathrm{s}^{-1}$, flow was no longer ortho-radial with the appearance of secondary flow shown as an irregular undulation wave at the shear band interface. When the $\dot{\gamma}$ increased further to 80 s^{-1}, emergence of taylor-vortices led to three dimensional flow and elastic turbulence[95,104]. However, since the dynamics of Taylor vortices was strongly correlated with the interfacial instability and inertia of the shear bands, it was difficult to determine the primary driving force for the

observed phenomena. Fardin et al.[1] further proposed that the instability of shear bands in a Couette cell originated from both curvature and large first normal stresses effects in the high shear bands. They summarized the onset of bulk and interfacial instability mechanisms with respect to a critical Weissenberg number (Wi) for different curved geometries in a single phase diagram. For the same wormlike micellar solution (CTAB and $NaNO_3$), Alexandre et al.[105] performed non-axisymmetric linear stability analysis using the modified Johnson-Segalman model with a diffusion term based on experimental observations of interfacial instability by Lerouge et al.[106]. Alexandre et al.[105] proposed that the instability evolution at the shear stress plateau depended on applied shear rates, where the interfacial undulation drove the instability at the beginning of the stress plateau at low shear rates, with the bulk instability in the high shear bands dominating at high shear rates.

1.1.2 Shear banding of wormlike micellar solutions in microfluidic shear flows

Planar microchannel flow was recently exploited to illustrate the interfacial undulation among the shear bands without complications from the bulk instability and secondary flow that originated from the curvature effects present in a Couette cell (discussed above). Unlike the bulk instability of high shear bands that originated from both curvature effects and normal stress difference, linear stability analysis of planar shear banded flow predicts that the instability at the shear banding interface in a planar geometry is driven by the normal force jump across the shear bands[48,107]. Nghe et al.[2] first reported experimental observations of interfacial instability of shear banding flow in a semi-dilute wormlike micellar solution ([CTAB]=33 mM; [$NaNO_3$]=20 mM) in a straight microchannel (dimensions as L_x=5 cm, L_y=64 μm, L_z= 1 mm, see Fig. 1.1(C)). They recorded velocity along x-direction v_x at the cross section ($y-z$ plane) by using 3D velocity imaging with fluorescent particles, as shown in the upper left image of Fig. 1.1(D), where y direction is perpendicular to the horizontal plane, and z is along the vorticity direction. The right side bar represents the magnitude of v_x. The dark areas correspond to the high shear phase close to the bottom wall and the brighter areas correspond to the low shear phase at higher L_y. Similar to previous observations

in Couette cell geometries, spatial interfacial undulations downstream were observed when the flow was fully developed, but this instability is driven by the normal force jump rather than the curvature effect. The quantification of the wave vector q_z, which was obtained from the multiplication of fully developed undulation wavelength and the channel height, agreed with the numerical studies from the linear stability analysis coupled with a diffusive Johnson-segalman (DJS) model, shown in the lower image of Fig. 1.1 (D). The analysis also predicted the appearance of vortices at higher pressure drops that could not be reached in the experiments[2].

Dhnot[108] introduced a "non-local" stress diffusion term in a linearized Navier-Stokes equation with a Maxwell constitutive model to "smooth" out the strong inhomogeneity in shear rate $\dot{\gamma}$ and normal stress jump across the shear band interface. A correlation length l involved in this process was proposed to capture the structure induced by the concentration fluctuation in high shear bands due to "non-local" effects, when the geometric dimension from the device became comparable with l. For example, a typical microchannel has a characteristic length $\sim 100\ \mu m$ while traditional cone-plate geometries render gap sizes on the order of 0.5–1 mm. Experiments showed that the correlation length l was very sensitive to experimental conditions and ionic environments. For example, Masselon et al.[40] studied shear banding behavior in a straight microchannel with two different wormlike micellar solutions: [CTAB]=300 mM/[$NaNO_3$]=405 mM and 6wt% CPyCl/NaSal ([NaSal]/[CPyCl]=0.5) in a 0.5M NaCl brine. They found that the CPyCl/NaSal system exhibited a sharp interface between shear bands with l ranging from 3–20μm, which was deduced from constitutive equations with experimental boundary conditions, described as follows. The applied boundary condition involved a shear rate value determined from the linear fit of the last three points in the velocity profile (due to large stress gradient) and the slip velocity. Viscosity $\eta(\dot{\gamma})$ was obtained by fitting the constitutive equations with experimental data. The correlation length l can thus be deduced from $l = \sqrt{D/\eta(\dot{\gamma})}$, where D is the micelle diffusivity. However, the high shear bands of CTAB/$NaNO_3$ system in the y-z plane showed comparatively both darker and brighter areas that resulted in a blurred interface. Masselon et al.[40]

proposed that this complex interfacial phenomenon might be caused by the smaller range of correlation lengths l in CTAB/$NaNO_3$ when compared with the CPyCl/NaSal system, which led to higher concentration fluctuations at the interface. The correlation length $l \sim O(\mu m)$ from Masselon et al.[40] was similar to the measurements from Lerouge et al.[109] and Ballesta et al.[110] in a Couette cell, but much larger than the quantity $l \sim$ O(nm) measured by Nghe et al.[2] and Radulescu et al.[111], for similar wormlike micellar solutions. These discrepancies might be caused by the following factors: 1D approximate analysis of the Couette flow resulted in a much thinner interface despite actual spatial variations within the interface[109], or the difficulty in separating the displacement of the interface (including the destabilization, reconstruction, and propagation of the interface)[40,106]. Therefore, further work is required to verify these arguments.

1.2 Wormlike micelles under extensional flows

1.2.1 Background

The behavior of wormlike micellar solutions in extensional flows is qualitatively different from that of shear flows, involving various microstructural modifications[112–114] and pure elastic flow instabilities[3,4,38,44,115]. Under extension, wormlike micelles exhibit an increase in the elastic tensile stress and extensional viscosity due to the stretching and possible growth of wormlike micelles[114]. Above a critical elongation rate, the extensional viscosity decreases due to the scission of micelles and rapid end cap formation[114]. This mechanism was verified by Chen and Warr[112] with light scattering measurements and more recently by Rothstein[113] by quantifying scission energy of filament rupture of wormlike micelles under elongation. Bhardwaj et al.[116] showed that a highly entangled and interconnected micellar network experienced different structural changes when different elongation fields were imposed by filament stretching and capillary breakup rheometers. A comprehensive review of strong extensional flows of wormlike micellar solutions and applicaitons has been provided by Rothstein[113].

The onset of strain thinning or hardening in extensional flow is often characterized by

the Deborah number (De) that characterizes the strength of elastic effects and the Reynolds number (Re) that is defined as the ratio of inertial to viscous effects. The strong viscoelastic effects on the dynamics of wormlike micelles often occur at high De or Wi, which usually take place at the midplane in the rheometer and are accompanied by the breakup of wormlike micellar networks. These strong viscoelastic effects can be further enhanced as the characteristic length scale of the geometry is reduced. Therefore, the impact of strong viscoelastic effects at large Wi or De can be easily achieved in microchannels, with minimum gravitational and inertial effects that are otherwise present in filament stretching and break up rheometers. Thus, macroscale extensional rheometers may not be a good candidate for both qualitative observations and quantitative measurements of weakly viscoelastic solutions with low elastic number El, defined as the ratio of Wi to Re numbers.

1.2.2 Wormlike micellar solutions in 4-roll mills and cross-slot flows

Recently, microfludic four-roll mills[117], cross-slots[3,4,38,44,115], and contraction geometries[118,119] have been used to study rheological and microstructural behavior of wormlike micelles under different extensional flow fields. Stagnation flows can be described by two opposing fluid streams flowing through a cross slot that produces an extensional flow at the stagnation point[44]. The flow kinematics in a cross slot is comparable to the four-roll mill flow designed by Taylor, which has been extensively used to generate pure extensional and rotational flows or a mixture of both flows with different speeds and rotational directions of the four cylinder rolls[120]. Four-roll mill flow has been widely used for studying polymer chains conformations[121–123] with flow induced birefringence and direct visualization of DNA tumbling dynamics by tracking fluorescent DNA molecules[124,125]. However, it has been proved extremely challenging to develop an analog microfluidic four-roll mill[117,126,127]. Hudson and co-workers[126,127] designed a microfluidic device with intersecting channels with asymmetric baffles. A stagnation point can be created in the center by choosing appropriate flow rates, but a pure rotational flow field can not be obtained due to the flow asymmetry. Muller and co-workers[117] later proposed an improved microfluidic four roll design to generate flow types

from pure rotational to pure extensional flow field, with four inlet and four outlet streams that were paired and arranged symmetrically about a central cavity. As an alternative, the cross-slot device, consisting of orthogonal bisecting channels with opposing inlets and outlets, can generate a planar extensional flow along the symmetric plane with a stagnation point at the center of the cross[128]. Due to its vorticity-free state, the largest extensional deformation and orientation in the microstructure can be achieved near the stagnation point[3]. Compared with the four-roll mill, the cross-slot geometry is much easier to build and control[44] and has been widely used to study dynamics of complex fluids under extensional flows. For example, Gardner[129] used the cross slot device to observe polymer stretching with extensional flow. This work was extended by Keller et al.[130] and Odell et al.[131] by coupling a cross slot device with flow induced birefringence to visualize the strain rates of highly stretched polymer molecules in localized regions. By quantifying birefringence strength and tracking the velocity profile with μ-PIV, the stability of the flow field and molecular orientation can be recorded simultaneously[3,4,38,132–136].

Pathak and Hudson[44] first used a cross-slot microfluidic device, with a channel height of 500 μm and an aspect ratio (height/width) of $\sim$0.53, and measured flow-induced birefringence to study the elastic instability of two different wormlike micellar solutions ([CTAB] = 33 mM/[NaSal] = 240 mM and [CPyCl] = 100 mM/[NaSal] = 60 mM) with cross-polarizers. They established the existence and evolution of both birefringence and transmittance bands of wormlike micelles at the stagnation point for different Wi numbers. Since the residence time within the channel is much larger than the scission and relaxation time of micelles, the micellar chains were able to disentangle near the stagnation point at each examined flow rate. This led to a high degree of alignment and formation of highly birefringent bands that broadened with increasing flow rates. They also observed an asymmetric flow transition and proposed that this transition was induced by elastic instabilities. Haward et al.[3,38] studied the same wormlike micellar solutions with the same geometry as Pathak and Hudson[44] but with a deeper channel ($\sim$1 mm in depth and an aspect ratio of channel height/width $\sim$5) to provide a wider Wi range and achieve an approximately 2D flow. In their study,

complete flow asymmetry, equivalent to the flow bifurcation observed by Pathak and Hudson[44], was observed at a different critical Wi. This observation was considered to be a consequence of the different channel dimensions and possible 3-D effects. Haward et al.[3,38] established an instability map according to the local Wi number with three broad categories (see Fig. 1.2(A)): a stable flow regime at low Wi, an intermediate Wi between a stable and unstable flow regime, and large Wi when flow became time dependent and three dimensional. Pseudo color retardance birefringence images shown in Fig. 1.2(A) illustrate the evolution of the stagnation flow.

More recently, Dubash et al.[4] mapped out a similar stability phase diagram as shown in Fig. 1.2(B) for CTAB:NaSal solutions with different surfactant concentrations and salt to surfactant concentration ratios: strongly viscoelastic ([CTAB]=100 mM; [NaSal]=32 mM), shear thinning ([CTAB]=75 mM; [NaSal]=24 mM), weakly viscoelastic ([CTAB]=75 mM; [NaSal]=18 mM), and shear thickening ([CTAB]=50 mM; [NaSal]=16 mM). Similarly, Dubash et al.[4] also observed a steady symmetry breaking instability and the appearance of a secondary flow, with formation of lip vortices (as shown in the upper inserted image in Fig. 1.2(B)) along the channel walls for the strongly viscoelastic solutions. They found that a critical Wi and Re were necessary for the onset of symmetry-breaking instability and the formation of vortices were in an opposite trend both from Haward et al.'s experimental work[3,38] and numerical predictions by Afonso et al.[132,137]. Although neither Haward et al.[3,38] nor Afonso et al.[132,137] reported the appearance of lip vortices, the experimental work by Rodd et al.[134] had similar trends as Dubash et al.[4]. Therefore, the formation of lip vortices may have an impact on the onset of symmetric breaking instabilities. It is worth noting that the environment of the micellar system such as the specific binding and unbinding salt, salt concentration, and surfactant types should be taken into consideration for the reported differences in the onset of instability among various research groups. The CPyCl:NaSal:NaCl micellar solutions used by Haward et al.[3,38] have longer micellar chains that require greater hydrodynamic forces to be fully stretched in contrast with shorter micellar chains studied by Dubash et al.[4]. Furthermore, CTAB micellar breakage can lead to different instabilities, especially under

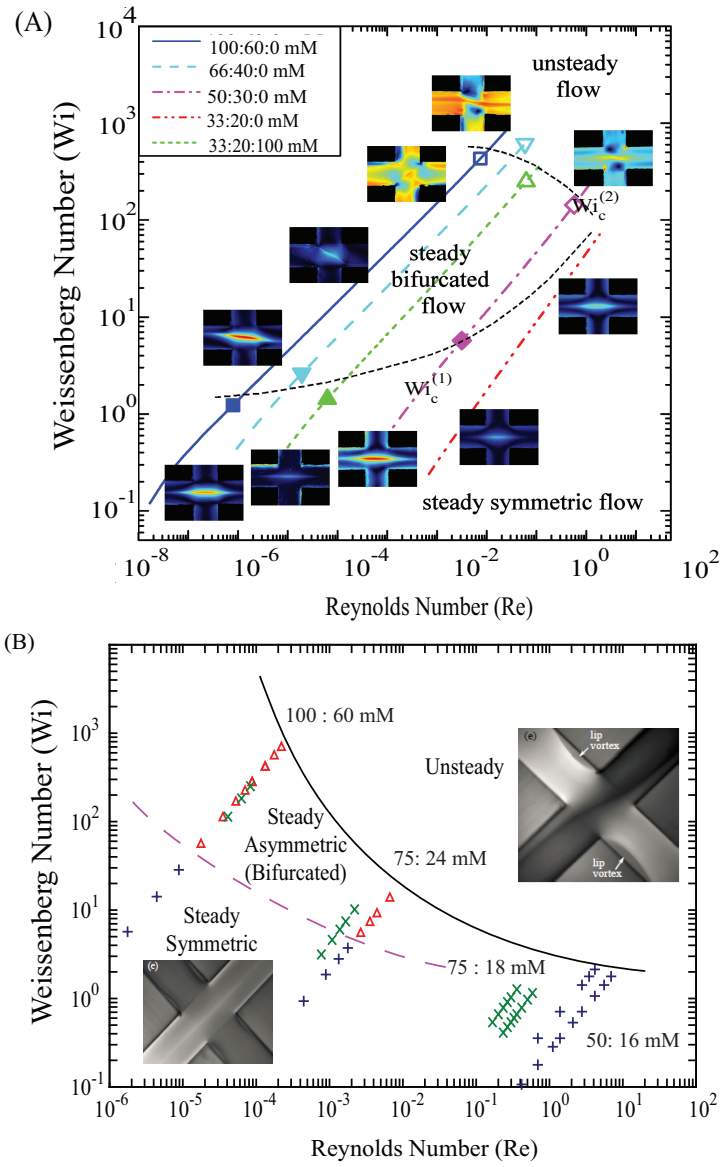

Figure 1.2: (A) Stability diagram in Wi–Re space shows the boundaries between elastic instabilities with the 4 different CPyCl:NaSal:NaCl wormlike micellar fluids (adapted from Haward and McKinly[3]); (B) Stability diagram in Wi–Re space shows the steady symmetric flow region, the asymmetric flow region, and the unsteady flow region pertaining to the symmetry-breaking instability. The inserted images are the steady symmetric flow and unsteady flow with lip vortices for [CTAB]=100 mM/[NaSal]=60 mM solution (adapted from Dubash et al.[4]).

strong shear or extensional flow[138–140]. For example, Gladden and Belmonte[140] flowed a wormlike micellar solution composed of [CTAB]=200 mM/[NaSal]=100 mM past a cylinder and showed a transition from fluid-like to solid-like fracture in the wake of cylinder after reaching a critical elongation rate. Numerical simulations by Hsieh et al.[141] showed that in a cross-slot, micellar chain breakage was localized near the stagnation point or the upstream of the corner, which is consistent with the experimental observation of lip vortices formation from Dubash et al.[4]. Thus, it is possible that the micellar breakage played an important role in affecting the onset of instability. Additionally, to simplify the calculations and comparison with numerical models, the magnitude of Re was based on the zero shear rate viscosity of the fluids and not the true local viscosity at different shear rates. At flow rates where shear thinning becomes important, Re varies with the local viscosity while the relaxation time in the Wi number shows a rate dependent decrease, which reflects the local change of the ratio of elastic normal stress to viscous shear stress under flow. This behavior is responsible for the different critical Wi and Re for symmetry-asymmetry transitions for different shear thinning solutions reported in literature.

1.2.3 Wormlike micellar solutions in contraction and expansion flows

Microfluidic contraction and expansion flows have also been widely used to generate extension dominated flow to impose large deformation rates for complex fluids without interference from inertia. The fluid travels with a positive strain rate upstream of the contraction and a negative strain rate downstream of the expansion[142–144]. The desired extensional deformation is realized by adjusting the geometry of the contraction and applied flow rates. Such devices introduce a shear dominated flow near the wall and extensional dominated flow at the channel centerline. The earlier studies with converging geometries have been performed with abrupt contraction-expansion geometries with both Newtonian and polymer solutions[145–147]. By determining the excess pressure drop across the contraction-expansion region, the extensional rate in the contraction flow device can be controlled. However, a main drawback of such devices is that the strain rate in the center line of the channel is not a constant. To

address this issue, a hyperbolic contraction is preferred by imposing a nominally constant extension rate along the centerline without upstream vortices. Even though entrance and wall effects cannot be completely ignored[5], the effective lubrication layers at the channel wall formed by the shear bands of wormlike micelle solutions enabled a plug-like flow in the core of the fluid that resulted in a greater homogeneous extensional flow field along the contraction region. Nystrom et al.[146] performed numerical simulations with a Finitely Extensible Nonlinear Elastic-Chilcott Rallison (FENE-CR) model to study Boger and Newtonian fluids in a contraction geometry. By simulating the flow and analyzing the strain and shear rate profiles with different axisymmetric contractions, they proposed an optimal contraction geometry design for achieving a constant uniaxial extensional flow with little impact from the shear flow in the system.

Both experimental and computational studies of wormlike micelle solutions flowing through microfluidic contraction and expansion geometries have also been reported[5,145,148–150]. Fig. 1.3 (A) shows a microfludic contraction geometry designed by Ober et al.[5] to characterize flow kinematics of wormlike micellar solutions as an extensional viscometer, coupled with pressure sensors (solid squares in Fig. 1.3(A)).The pressure drop at the contraction region δP_c can be related to the pressure drop δP_{23} normalized by δP_{14}. The elongation rate $\dot{\epsilon_a}$ at the contraction middle plane can be deduced from the slope via linear regression to the centerline axial velocity profile mapped out from μ-PIV. Coupled with the total Hencky strain ϵ_H, given by $\ln \frac{w_u}{w_c}$ where w_u and w_c are the widths of the large and narrow sections of the hyperbolic contraction, respectively, the elongational viscosity can be determined by $\frac{1}{\epsilon_H}\frac{\delta P_e}{\dot{\epsilon_a}}$, where δP_e represents the elongational contributions in the total pressure drop δP_c. The experimental results showed good agreement with theoretical predictions of the extensional viscosity in a homogeneous extensional flow with a shear thinning exponential Phan-Thien/Tanner (PTT) fluid model. The first normal force difference (N_1) can be estimated by $\frac{\delta P_c}{\dot{\epsilon}}$ and confirmed with quantitative FIB measurements (as shown in the low half of Fig. 1.3 (B)), from which the optical anisotropy of wormlike micelles can be obtained and related to stress through the stress optical rule[151].

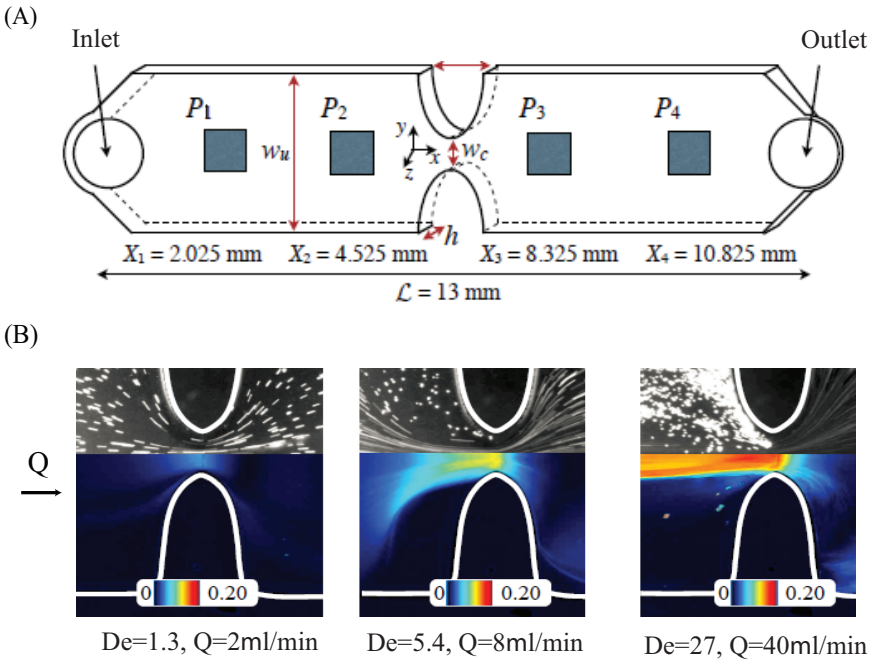

Figure 1.3: (A) Schematic of hyperbolic planar contraction microfluidic device used as an extensional rheometer with solid squares representing pressure sensors (adapted from Ober et al.[5]); (B) Streakline embedded with fluorescence particles (upper half) and pseudocolor retardance maps of flow induced birefringence (lower half) for [CPyCl]=100 mM/[NaSal]=60 mM flowing through a microfluidic hyperbolic contraction geometry (adapted from Ober et al.[5]).

1.3 Wormlike micelles under complex flows

The characterization of wormlike micelle solutions under shear and elongation has exhibited a wealth of interesting new flow dynamics and rheological responses. "Pre-conditioning" (including pre-shearing and small amplitude oscillatory straining) prior to stretching has been applied to monodisperse and bidisperse polystyrene solutions[152], dilute DNA solutions[153], polymer solutions[154–157], and wormlike micellar solution[113,158]. Bhardwaj et al.[158] reported that by pre-shearing wormlike micellar solutions prior to stretching, the onset of strain hardening was significantly delayed. The need for the micelles to either rotate from the pre-sheared direction to the stretched direction, or to compress its equilibrium conformation before stretching caused this strain hardening delay. Since the maximum elastic tensile stress decreases dramatically with increasing pre-shear rate, a pre-sheared step might also reduce the size of the wormlike micelles, or change the interconnectivity of the micellar network before stretching.

Motivated by these existing reports, well controlled investigations of wormlike micelles in complex flow fields would offer further insight on new flow dynamics as well as microstructural evolution. Compared with traditional rheometry, microfluidic devices offer a robust and convenient approach to study the behavior of wormlike micelles under complex flow field due to their flexibility in design. Previous studies of wormlike micellar solutions in the complex geometries involved macroscopic investigations up to the millimeter scale, such as flow past cylinders with or without confined boundaries around the cylinder[138,139], falling spheres[159], bubbles, and porous media flow[73–76,160–165]. Ruckenstein and co-workers[161] studied equimolar cationic surfactant hexacyltrimrthylammoniumsalicylate (C16MTA-Sal) and NaBr mixture flowing through randomly packed glass beads (diameter of 392 μm, a porosity of 0.38 and a hydraulic radius around 40 μm). They studied the relationship between the Reynolds number and the resistance coefficient Λ ($\Lambda = f * Re$, where f is the friction factor and Re is the Reynolds number, Λ can also be interpreted as a dimensionless apparent viscosity[166]). In Newtonian fluids, Λ is a constant in a wide range of Re ($5 * 10^{-5} < Re < 500$) before

reaching turbulent flows. In the shear thickening surfactant solutions, a sharp increase in Λ beyond a critical Re was observed and followed by a decrease in Λ with increasing Re. Brunn and Vorwerk[75,76] mapped out Λ as a function of Re at different temperature and concentration for the same cationic surfactant system. A good similarity between Λ – Re curve and η – $\dot{\gamma}$ in viscometric flow was observed: the onset of sudden increase in $\Lambda(Re)$ corresponded to the onset of shear thickening in $\eta(\dot{\gamma})$. The characteristic shear stress τ^* in porous media flow can also be represented as a function of hydraulic radius R_h and pressure drop ΔP[162]. It was suggested that shear played an important role in the analogous flow behavior in porous media: shear induced structure formation in porous medium is similar to the SIS formed under pure shear flow. The association and dissociation of the structures depended on the velocity gradient, ionic environment, temperature, and flow characteristics in porous media flow[73–76,161]. More recently, Rojas et al.[164,165] investigated porous media flow (with a disordered packed glass spheres of 1.13 mm in diameter and a porosity of 0.38, a characteristic length of the pore-scale is around 60 μm) of wormlike micelles solutions formed by oppositely charged surfactant mixture cationic cetyl trimethylammonium p-toluene sulfonate (CTAT) and anionic sodium dodecyl sulfate (SDS). Compared with viscometric shear flow, the increase of resistance coefficient Λ was substantially larger than the viscosity η increased in shear thickening region. They pointed out besides shear, the extensional component in the local pore regimes promoted the entanglement of wormlike micelles, which could yield stronger cooperative structures, leading to enhanced viscoelasticity in the solution. Müller et al.[167] studied a concentration range of 0.05 wt% to 0.23 wt% shear thickening CTAT aqueous solutions under pure shear, pure elongation, and porous media flow. They proposed that the magnification of shear thickening in porous media flow was a synergistic effect from both shear and elongation impacting on the microstructure of wormlike micelles. Different from strong extensional flow alone, the elongation component in the porous medium was strong enough to promote the increasing interactions between micelles with shear flow without completely breaking and deconstructing structures. These macroscopic porous media flow can generally provide a shear rate up to O(10^3 s^{-1}) but the data at higher shear rates

were usually accompanied by flow instabilities and turbulent flows when Re exceeds 10[75,76]. It is important to note that studies on complex macroscale flow field may not be completely comparable to wormlike micelles solutions under complex flow field in microfluidics due to the high strain $O(10^4)$ and strain rate $O(10^4\ s^{-1})$ with vanishing inertia effects present in the microchannel. In this section, we highlight wormlike micelles in porous media simulated flow in microfluidics to illustrate how spatial confinement in microfluidics influences the rheology and microstructure of wormlike micelles.

It is well documented that in certain dilute wormlike micellar solutions, under simple shear flow above a critical shear rate, a more viscous phase is formed with highly aligned and locally concentrated micellar strings that have been termed as shear induced structures (SIS) or shear-induced phases (SIP) in literature[6]. In the SIS state, the solutions are birefringent and exhibit strong anisotropic light and neutron scattering. Fig. 1.4(A) shows light scattered from the formation of SIS as observed by Liu and Pine[6], described as "gel-like fingers", within a transparent Couette cell under shear. Experiments have shown that the formation of SIS does not permanently change the local micellar structure and were found to disintegrate after cessation of flow[6]. However, Vasudevan et al.[70] recently reported the formation of a long-lived flow-induced structured phase (FISP) by flowing a series of semi-dilute CTAB:NaSal solutions (termed precursors) through a microfluidic tapered channel packed with glass beads ($20 \sim 100\ \mu m$ in diameter). The packed glass beads simulated porous media flow capable of achieving a total strain of $O(10^4)$ with a combination of shear and elongation deformation rates of $O(10^4\ s^{-1})$. Dubash et al.[71] later introduced a new microfluidic device by embedding microposts that generated the same irreversible FISP without the use of glass beads (see Fig. 1.4(B)). The micropost device with gap sizes around 15 μm was able to achieve similar high strain and strain rates for precursors, with Fig. 1.4(C) showing the FISP flowing out of the microposts. Using a technique termed microrheology[168], they found that the zero shear viscosity η_0, plateau modulus G_o, and relaxation time λ in the FISP were one order of magnitude larger than those of the precursor. Cheung et al.[7] later visualized the formation and concentration variations of wormlike micelles in the micropost device using a

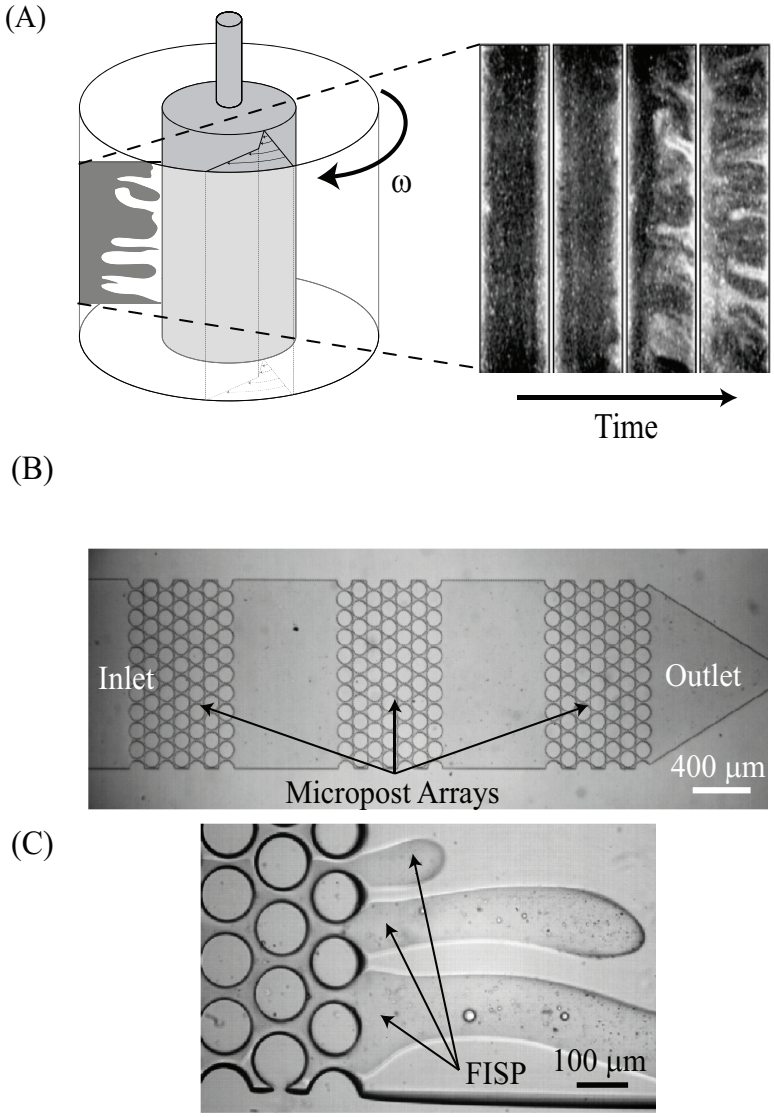

Figure 1.4: (A) Visualization of shear induced structure (SIS) generated and buildup after commencement under pure shear flow in a Couette cell (adapted from Liu et al.[6]); (B) The microfabricated PDMS micropost arrays used for the generation of the flow induced structured phase (FISP); (C) An in-situ image of FISP generation from microposts with deformation rates of O(10^4 s^{-1}) and total strain of O(10^4) (adapted from Cheung et al.[7]).

fluorescent Nile Red dye that preferentially bound to the micelle interior and interface. The fluorescence intensity was found to be linearly dependent on the CTAB concentration and allowed determination of local concentration fluctuations within the channel during flow[7]. This micropost configuration was shown to generate local micellar concentration variations $\sim 25\%$ higher than that in bulk flow, crucial for creating FISP.

Cardiel et al.[8] later used a similar micropost design to form the FISP and utilized electron microscopy imaging to visualize the multiconnected micellar networks with three-fold junctions and branches as shown in Fig. 1.5. Similar multiconnected micellar networks were reported in ionic micellar solutions in the literature but at very high salt concentrations[169,170]. Cardiel et al.[8] proposed that the transition from rodlike micelles in semidilute precursors to multiconnected networks in FISP was induced by the spatial confinement (or gap spacing) between microposts (5-15 μm), with deformation rates of O(10^4 s^{-1}) and total strain of O(10^4). When rodlike micellar bundles were stretched and aligned under flow between the microposts, the bending energy of micelles was reduced which allowed flexible micelles to fuse and form junctions and branches with other surrounding micelles, see Fig. 1.5. Note that these phenomena were only reported with microfluidics with a spatial confinement down to 15 μm. When the spatial confinement was enlarged up to 100 μm and greater, only SIS was observed that disintegrated after cessation of the flow, which is consistent with the results from traditional rheometry[6]. These irreversible FISP have shown great potential in enzyme encapsulation, environmental sensing, and other applications due to their highly nanoporous scaffold structures[171].

1.4 Thesis Outline

In this thesis, we focused on an aqueous micellar solution of cationic surfactant cetyltrimethyl ammonium bromide (CTAB) and organic hydrotropic salt 3-hydroxy naphthalene-2-carboxylate (SHNC) in the semidilute regime. Different from NaSal with one benzene ring, the strong hydrophobicity and naphthalene structure present in the SHNC induces significant growth of CTAB wormlike micelles and promotes stable micellar network formation. We first sys-

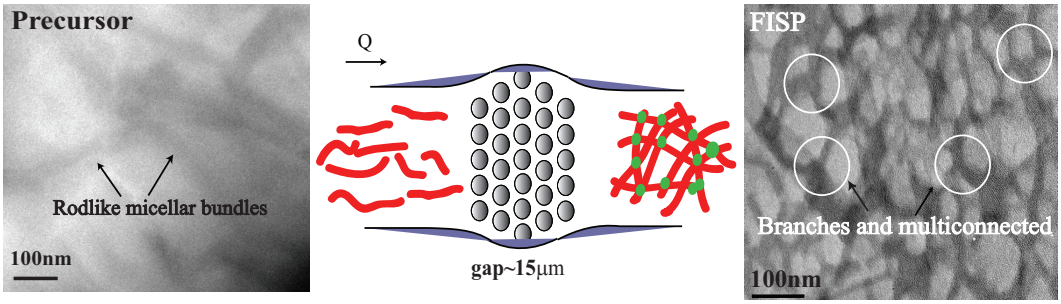

Figure 1.5: Microstructural evolution of a semi-dilute wormlike micellar solution flowing through a microdevice with microposts. The precursor ([CTAB]=50 mM; [NaSal]=16 mM) contains randomly distributed rodlike micellar bundles, while the corresponding FISP generated from microposts shows multiconnected micellar branches indicated by white circles (adapted from Cardiel et al.[8]).

tematically studied the rheological behavior of the CTAB/SHNC mixture at different concentrations and under thermal variations, compared with CTAB/NaSal micellar system at the same concentration. With a thorough understanding of the rheological behavior of the micellar system, we then moved forward to study how the WLM behaved under complex flow fields, by utilizing confined microfluidic cylinder devices with three different cylinder blockage ratios. A variety of flow phenomena revealed by flow visualization techniques are quite different from that with Newtonian and polymer solutions. We associate the onset of instability upstream of the cylinder with the compression at the leading edge of the cylinder and the growth of viscoelastic stresses generated by the squeezing flow into the the narrow gaps between the cylinder and the channel walls. The instability downstream of the cylinder is associated with stresses generated at the trailing stagnation point and the resulting flow modification in the wake, coupled with the onset of time-dependent flow upstream and the asymmetric division of flow around the cylinder.

Chapter 2

WORMLIKE MICELLAR SOLUTION OF CTAB/SHNC MIXTURE

In this chapter, we investigated the linear and nonlinear rheology of CTAB/SHNC mixture in the semi-dilute regime. We correlate the rich rheological behavior with structural transition of the micelle network under different deformation histories with temperatures in the range 20 °C $< T <$ 40 °C. Viscous dissipation dominates at low temperature, while short range interactions among micellar head groups, reformation and re-organization of micellar networks play important roles at higher temperatures, leading to complex stress responses under large deformations. The influence of double benzene rings on the response of transient and large amplitude oscillatory shear flows in the system was further elucidated by comparing the rheological behavior of CTAB/SHNC and CTAB/NaSal at the same salt and surfactant concentrations. Our studies distinguished SHNC as a stable hydrotrope in a semi-dilute cationic surfactant system under thermal variations, with potential applications such as drag reduction and fracturing fluids in oil recovery.

2.1 Introduction

Hydrotropic salts are a class of amphiphilic compounds that cannot form micellar aggregates, but can solubilize organic molecules in water. Structurally similar to surfactants, hydrotropic salts can act as strong "binding" additives and reduce surface tension in an aqueous solution. A number of organic hydrotropic salts such as NaSal[13,33], SHNC by Mendes et al.[172,173], p-toluene sulfonate by Soltero et al.[174], chloribenzoate by Carver et al.[175], and naphthalenesulfonate by Brown et al.[176] have been studied in combination with cationic surfactants because these mixtures can reduce the charge density of surfactant micellar aggregates sig-

nificantly, enhancing ion pairing and surface activity of the micelles above a minimum hydrotropic concentration (MHC), and promoting growth of wormlike micelles at a much lower salt/surfactant ratio in comparison to other salts[177–180]. In addition, Schubert et al.[181] reported that adding hydrotropic salts NaTosylate (0.25 wt%) could screen the electrostatic interactions and reduce the micellar surface charge in a mixed cationic/anionic wormlike micellar solution consisting of cetyl trimethylammonium tosylate (CTAT, 0.5–4.0 wt%) and sodium dodecyl benzyl sulfonate (SDBS), with CTAT/SDBS = 97/3.

In particular, the hydrotropic organic salt SHNC has drawn considerable attention as HNC^- ions have exhibited sensitive responses with varying temperatures, ionic strength, and flow conditions. In addition, mixtures of cationic surfactant and excess amount of SHNC have shown pronounced birefringence phenomena lasting from milliseconds up to even hours after the flow stoppage[10,182]. Recent studies have used light scattering, flow birefringence, electron microscopy, and rheometric techniques to investigate the material properties of SHNC and cationic surfactant mixtures. Mishra et al.[10,183] reported the phase behavior of the mixture of cationic surfactant cetyltrimethylammonium bromide (CTAB) and SHNC. By fixing the CTAB concentration at 60 mM and gradually increasing the CTAB/SHNC molar ratio, the CTAB/SHNC mixture underwent phase transitions from small micellar aggregates to a positively charged gel phase, followed by a liquid crystalline lamellar phase, then precipitated into a multi-lamellar vesicle phase at equi-molar surfactant/salt concentration. In particular, when the concentration ratio of SHNC over cationic surfactant exceeds 1.0, SHNC was observed to inhibit growth or entanglement of micelles by negatively charging micelle surfaces[10,183–185]. When the temperature increases or the solution is further diluted, the HNC^- ions can actually desorb from the micelles and decrease the surface charge of micelles, which in turn promotes growth of wormlike micelles and enhances the viscoelasticity of the solution. Notably, the rich phase behavior of CTAB/SHNC mixture is similar to that of the mixture of cationic-anionic surfactant system (CTAB/Sodium dodecyl sulfate (SDS)) as described by Kaler et al.[186]. SHNC is thus considered as an anionic surfactant similar to SDS but with a shorter hydrophobic tail (around 4 nm[187–189]).

Interestingly, the phase behavior of CTAB/SHNC and CTAB/NaSal shows distinct differences even though SHNC and NaSal are both hydrotropic organic salts that possess the same chemical elements. With fixed CTAB concentration, addition of NaSal also promotes the aggregation of CTAB micelles by screening the electrostatic interaction between surfactant micelles, thereby yielding long and flexible threadlike micelles[13,33]. When the concentration ratio of CTAB/NaSal reaches 1.0, the most stable and rigid micelles are formed in the solution and the linear viscoelasticity of the resulting fluid can be described by a single mode Maxwell model. As the concentration of NaSal increases further, a branched micellar network is observed, with no precipitation or vesicle formation[13,33].

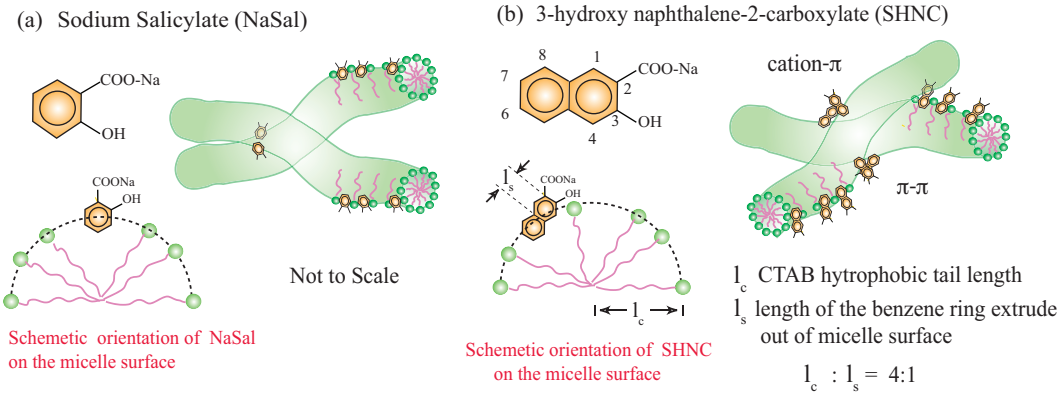

Figure 2.1: Chemical structures and schematic representation of the orientation of (a) NaSal and CTAB/NaSal micelles[9]; (b) SHNC and CTAB/SHNC micelles[10]. The numbers represent positions around naphthalene ring where carboxyl and hydroxyl can be substituted. The green dots represent hydrophilic headgroups of CTAB while purple lines represent its hydrophobic tails I_c. The green tubelike entities represent wormlike micelles in solution. In CTAB/SHNC micelles, extra intramolecular forces are introduced by π–π and cation–π interactions.

Figure 2.1 illustrates a side-by-side comparison of the chemical structure of two hydrotropic salts: NaSal and SHNC, and their respective interactions with cationic surfactant CTAB. NaSal has one benzene ring while SHNC has two fused benzene rings (termed as the naphthalene ring). The numbers shown in Fig. 2.1(b) represent positions around the naph-

thalene ring where carboxyl and hydroxyl groups can be substituted. The green threadlike entities represent wormlike micelles in the solution. Due to closer proximity and better interactions between carboxyl (position 2) and hydroxyl (position 3) groups in SHNC molecules, stronger bonds from $\pi - \pi$ and cation $- \pi$ interactions can be formed in SHNC-cationic surfactant micelles, yielding changes in the size and shape of micellar aggregates in the solution by Gravsholt et al.[190]. To validate this argument, HNMR spectra show that one of the benzene rings strongly adsorbs on the surface of cationic micelles with the other one connected with carboxyl and hydroxyl groups protruding out of the micelles, serving as an extra "tail" because its length is comparable with that of CTAB tails by Mishra et al.[10] (see Fig. 2.1). The length of the benzene ring extruding out of the micelle surface was reported to be $\sim$0.4 nm and the hydrotrophobic tail length of CTAB is $\sim$ 1.7 nm[10]. The spontaneous curvature of micelles changes significantly when SHNC is mixed with CTAB solution, in comparison to that of CTAB/NaSal mixtures. As a result, CTAB/SHNC mixtures have shown complex rheological behavior that is associated with higher surface activity and extra intramolecular interactions of micelles[191,192].

The position of the carboxyl and hydroxyl groups in the naphthalene ring of the salt molecule can also play an important role in the wormlike micellar system due to different hydrophobicity. Comparing with SHNC (3,2 HNC), 6-hydroxy-naphthalene-2-carboxylate (6,2 HNC) shares the same chemical compounds as those of SHNC but the carboxyl and hydroxyl groups in the naphthalene ring reside in position 2 and 6 respectively (see Fig. 2.1(b)). For 6,2 HNC and CTAB at equal molar concentrations, multilamellar precipitates were not observed by Abdel et al.[15]. Brown et al.[176] studied the mixture of CTAB and sodium naphthalene sulfonate, in which one of the positions in the naphthalene rings was substituted by a single sulfonate ion. The aqueous solution exhibited similar phase behavior and viscoelasticity as those in the mixture of CTAB/NaSal, which remains aqueous in a wide range of salt concentrations[17,33,176]. It was proposed that the combination of the naphthalene structure and the strong hydrophobicity of HNC^- was responsible for the unique phase behavior in SHNC-cationic surfactant mixtures[15,193].

Most of the existing literature investigated SHNC/surfactant systems with molar ratios R=[salt/surfactant] being 1/1 or greater in cationic surfactant systems. Since semi-dilute micellar solutions usually possess weak viscoelasticity, they are more desirable for oil recovery and encapsulation related applications with higher mobility. Moreover, cationic surfactant solutions with organic salts in the semi-dilute regime have shown not only interesting rheological behaviors[33,194,195], but also exhibited unique capabilities in forming irreversible nanostructured phases[8,70,71,196] for encapsulation and sensing applications[171,197]. Motivated by the temperature sensitive nature of SHNC and the advantage of semi-dilute wormlike micellar solutions, this work focused on the rheological behavior of aqueous CTAB/SHNC mixtures in the semi-dilute regime, in which micelles are positively charged and isotropically distributed. Moreover, since we have existing rheological data of CTAB/NaSal system at R = [NaSal/CTAB] = 0.32[71], studying CTAB/SHNC systems at R = 0.32 allows us to understand the influence of double benzene ring (SHNC) versus the single benzene ring (NaSal) on the rheological properties of CTAB/salt systems. We performed detailed linear and nonlinear rheological characterizations of CTAB/SHNC solution with [CTAB]=75 mM ($R = 0.32$), at different temperatures. The influence of double benzene rings on the response of transient and large amplitude oscillatory shear flows in the system was further elucidated by comparing the rheological behavior of CTAB/SHNC and CTAB/NaSal at the same salt and surfactant concentrations.

2.2 Materials and Methods

2.2.1 Materials

Cationic surfactant CTAB and organic hydrotropic salt NaSal were purchased from Sigma-Adrich (Saint Louis, MO) and organic hydrotropic salt 3-hydroxy naphthalene-2-carboxylate (SHNC) was purchased from TCI America (Portland, OR), all used as received. The solutions were prepared by adding the appropriate amount of CTAB and SHNC (or NaSal) to deionized water and mixing vigorously for a minimum of 24 hours, and left to equilibrate for 1 week.

Four different solutions were examined in this work: CTAB concentrations at 40 mM, 60 mM, and 75 mM with fixed molar ratio of $R = 0.32$. An aqueous solution containing [CTAB] = 75 mM and NaSal with the molar ratio $R = 0.32$ was also studied as a comparison.

2.2.2 Rheological measurement principles and methods

Linear viscoelasticity of wormlike micelles

Micelles can break and reform continuously. When the kinetic process of micellar breaking and reforming dominates over the timescale for reptation, the micellar solution shows Maxwellian behavior with a single-dominant relaxation time[12,198]. The elastic modulus (G') and loss modulus (G'') of the wormlike micellar solution can be described by the Maxwell model with a single stress relaxation time λ_r,

$$G'(\omega) = \frac{G_0(\omega\lambda_r)^2}{1+(\omega\lambda_r)^2}, \quad G''(\omega) = \frac{G_0\omega\lambda_r}{1+(\omega\lambda_r)^2}, \tag{2.1}$$

where ω is the angular frequency and the stress relaxation time λ_r can be obtained either as the reciprocal of the ω at the crossover of G' and G'', or from the above single Maxwell model. Plateau modulus G_0 is extracted by fitting the experimental measurements with a single Maxwell model and can be related to the micellar mesh size as[199]

$$\xi_m \simeq \sqrt[3]{\frac{k_BT}{G_0}}, \tag{2.2}$$

where k_BT corresponds to the thermal energy.

On the other hand, when the micelle breakup time is long compared with its reptation time, dynamic properties of these entangled micelles are dominated by reptation by Cates et al.[198]. In the reptation process, stress relaxation is induced by the gradual disentanglements of micellar chains along the curvilinear tube environment, leading to deviations from the single Maxwellian behavior and displaying multi-mode relaxation times. Shikata et al.[35] reported that if the micelles were too long and unstable to reptate (i.e., for an equal molar concentration of CTAB and NaSal solution), wormlike micelles could form networks with finite extensibility and sticky temporal cross-links at entanglement points. These temporal

crosslinks can contact and clash with each other with salts serving as catalysts. Granek et al.[200] further proposed a Poisson renewal model to study wormlike micellar systems with short breakup times, while the relaxation process is dominated by breathing and local Rouse motion rather than reptation. The effects from breathing and Rouse motion were characterized by an upturn of both $G'(\omega)$ and $G''(\omega)$ at higher frequencies in the oscillatory shear flow, exhibiting a dip of minimum value G''_{min} in the Cole-Cole plot, in which the viscous modulus $G''(\omega)$ is normalized by the plateau modulus G_0 and plotted against the normalized elastic modulus $G'(\omega)$. The depth of G''_{min} found in the Cole-Cole plot can be used to estimate the entangled chain length in wormlike micellar solutions, where the entanglement length is much longer than the persistence length of the micelle. The ratio of the local dip value of G'' (i.e., G''_{min}) with respect to the plateau modulus G_0 can be used to estimate the average length of the entangled micelles as[199,200]:

$$\frac{l_e}{\bar{l}} \approx \frac{G''_{min}}{G_0}, \tag{2.3}$$

where $\bar{l}$ represents average micelle length in the micellar system, and l_e is the length of micellar chains between entanglement points that can be estimated by[199,200]

$$l_e \simeq \xi_m^{5/3}/l_p^{2/3}, \tag{2.4}$$

where l_p presents the persistence length of micelles. The persistence length l_p can be obtained from small-angle neutron scattering measurements. Since ξ_m can be obtained from Eq.(2.2), the length of micellar chains between entanglement points l_e can be estimated by Eq.(2.4), and the average micelle length $\bar{l}$ can then be approximated from Eq.(2.3). For a wormlike micellar system when $\lambda_b \sim \lambda_{rep}$, Eq.(2.3) is not applicable but provides an upper bound of $l_e/\bar{l}$. Hence, the calculated $\bar{l}$ can be used as a lower bound for the estimation of the averaged micellar length.

Large amplitude oscillatory shear (LAOS)

In the linear viscoelastic regime, the material response is related to the intrinsic properties of the material and is independent of the strain and frequency input. In the nonlinear regime, where the linear viscoelastic model is no longer valid, the evolution of the micellar microstructures under large deformations plays an important role in determining the transient rheological response. Although linear viscoelasticity is useful for understanding the relationship between the microstructure and rheological properties of complex fluids, the linear viscoelastic moduli (G' and G'') are limited by the first harmonic Fourier coefficients of G' and G'', which are insufficient to describe the nonlinear material response with a distorted sinusoidal stress response. The large amplitude oscillatory shear (LAOS) procedure has been employed to provide more detailed information on the viscoelastic response of materials under nonlinear regimes, by capturing higher harmonic Fourier coefficients or Chebyshev coefficients[201,202] of stress responses, or fitting experimental data with different viscoelastic models[203–208], by applying different flow procedures[202,209,210]. In fact, materials containing microstructures can exhibit different stress waveforms in the nonlinear regime[211–213]. For example, Hyun et al.[214] compared the rheological response of a linear structured polymer solution with a branched polymer solution under large amplitude oscillatory shear, and observed two different distorted sinusoidal stress waveforms. A Pipkin diagram was built to illustrate the microstructure evolution of complex fluids (such as biopolymer gels, polymer networks, chewing gums, and wormlike micellar solutions) under different strains and frequencies in the nonlinear regime[201,202,215]. The interpretation of nonlinear stress response was based on Chebyshev orthogonal functions correlated with the distinctive response from viscoelastic materials. Comprehensive reviews of interpreting rheological behavior under large amplitude oscillatory shear flow can be found in the literature[202,212,216,217].

In oscillatory shear flows, the material deformation can be described by

$$\gamma = \gamma_0 \sin(\omega t), \tag{2.5}$$

where ω is the angular frequency, t is the time, and γ_0 is the input strain amplitude. In the

linear viscoelastic regime, the stress response is sinusoidal and corresponds to an elliptical stress curve with respect to the strain. When the strain reaches the nonlinear regime, the stress curve starts to become asymmetric and deviate from the sinusoidal shape. Accordingly, the stress (σ) versus strain (γ) curve (also known as Lissajous-Bowditch curve) would be distorted from the elliptical shape due to the stress contributions at higher harmonics. The normalized higher harmonics represent the degree of distorted stress signals and quantify the nonlinear response. To quantify the degree of the stress distortion, a half-sided (only odd parts for the sine function) discrete Fourier transform can be applied to the stress signal as

$$\sigma(t) = \sum_{n=1,odd} \sigma_n \sin(n\omega t + \phi_n), \tag{2.6}$$

where σ_n and the phase angle ϕ_n depend on the imposed γ_0 and ω[218]. Neidhofer et al.[219] substituted time $t = t' - \phi/\omega$ to obtain the following relation:

$$\sigma(t) \propto \sin(\omega t') + I_3 \sin(3\omega t' + \phi_3') + I_5 \sin(5\omega t' + \phi_5') + I_7 \sin(7\omega t' + \phi_7'), \tag{2.7}$$

where $\phi_n' = \phi_n - n\phi_1$ is the relative phase angle relating to the shape of the stress signal. The odd coefficients, I_3, I_5, I_7 correspond to 3rd, 5th, 7th harmonic coefficients normalized by the first harmonic respectively that can be calculated to analyze the nonlinearity of the shear stress under large deformations. Assuming higher harmonic coefficients (i.e, I_5, I_7) are negligible, ϕ_3' is the relative phase angle that determines the shape of stress versus time curve, with $\phi_3' = 0°$ corresponding to a normalized stress curve as a function of time[220]. At $\phi_3' = 90°$, the stress versus time curve has backward tilted tendency, while the curve returns to the sinusoidal shape at $\phi_3' = 180°$, eventually evolving to a "forward tilted shoulder" at $\phi_3' = 270°$[204]. Similar patterns were observed in our experiments. The even harmonics of Fourier series (0th, 2nd, and 4th) have been suggested to be associated with the nonlinearity of normal stress coefficients[202,221]. Giacomin et al.[221] derived analytical expressions for 0th, 2nd, and 4th harmonics of the second normal stress difference in LAOS by using a non-linear co-rotational model and matched their results with the co-rotational Maxwell model. Ewoldt[202] pointed out that even harmonics of Fourier series (related to the first normal stress

difference) in LAOS strongly depended on the input strain representation (whether sine or cosine function). Therefore, we neglect the even harmonics and focus on the odd harmonics in the stress response for the quantification of LAOS responses in this work.

Measurements

The viscoelastic properties of the wormlike micellar solutions were characterized by using a stress controlled rheometer (Anton Paar MCR 502). All measurements were performed by using a stainless steel cone and plate geometry (50 mm diameter and 2° angle) with a truncation gap of 59 μm. Experiments were performed at temperature between 20 °C and 40 °C. The Anton Paar MCR 502 employs a Peltier element within the base plate and the temperature is maintained stable within ± 0.1°C. We wait 10 min after loading the sample in order for temperature to reach equilibrium before measurements. Considering potential artifacts in the large amplitude characterizations, all measurements were repeated 3 times and verified by a roughened plate-plate geometry (25 mm in diameter) with a gap size of 500 μm. A solvent trap was used to prevent drying effects.

2.2.3 Dynamic light scattering

Dynamic light scattering (DLS) provides a convenient method to probe the dynamic properties of wormlike micellar solutions in a large range of concentrations[198,222–228]. In the semi-dilute regime of a wormlike micellar solution where a viscoelastic network is formed by entangled and overlapped wormlike micelles, the diffusion coefficient D characterizing the local cooperative diffusion motion in the network[227], can be determined from the measurement of auto-correlation functions of the scattered light $g^{(2)}(l,q)$ as

$$g^{(2)}(l,q) = A(1 + b|g^1(\lambda,q)|^2), \tag{2.8}$$

where A is the experimental baseline, b is the spatial coherence factor that depends on the number of coherence areas generating the signal ($0<b<1$), q is the scattering vector that can be expressed as $q = \frac{4\pi n}{l}\sin(\frac{\theta}{2})$, with l being the incident laser wavelength, n and θ

being the refractive index of the scattering medium and the scattering angle, respectively. In the dilute regime, $g^{(1)}(l,q)$ is a single exponential function with a characteristic time inversely proportional to q^2, which characterizes a diffusive behavior. In a polydispersed system with several relaxation times, $g^{(1)}(l,q)$ can be analyzed by a constrained regularized CONTIN method[229,230] to yield information on the normalized distribution of the decay constant $G(\Gamma)$ as

$$g^{(1)}(l,q) = \int_0^\infty G(\Gamma)\exp(-\Gamma t)d\Gamma. \tag{2.9}$$

This method can be applied to determine the average relaxation time λ of $g^{(1)}(l,q)$ by

$$\lambda = \frac{\int G(\Gamma,q)\Gamma d\Gamma}{\int G(\Gamma,q)d\Gamma}. \tag{2.10}$$

Thus, the diffusion constant D can be calculated from[198]

$$D = \frac{1}{q^2\lambda}, \tag{2.11}$$

which can be further related to the hydrodynamic correlation length ξ_H, which estimates the mesh size of the micellar network[198,223–225]

$$\xi_H = \frac{k_BT}{6\pi\eta_sD} = \frac{k_BTq^2\lambda}{6\pi\eta_s}, \tag{2.12}$$

where k_BT is the thermal energy and η_s is the solvent viscosity at absolute temperature T.

In our work, the hydrodynamic correlation length ξ_H was measured by a dynamic light scattering (DLS) apparatus, equipped with a He-Ne laser (Zetasizer Nano ZS, Malvern). The time correlation function measured by DLS was analyzed by a Laplace inversion program (CONTIN)[229–231]. Experiments were carried out with temperature ranging from 20 °C to 40 °C, at a scattering angle of 173° and the wavelength at 633 nm under vacuum setting. Each sample was equilibrated for 20 minutes before measurements for a given temperature. The correlation length ξ_H of the micellar solution was obtained to evaluate the diffusivity coefficient D of each sample.

We also obtained the polydispersity of the solution from dynamic light scattering measurements (Zetasizer Nano ZS, Malvern). In particular, the polydispersity index was calculated from the cumulants analysis of the DLS-measured intensity autocorrelation function[229–231]. In the cumulants analysis, a single particle size mode is assumed and a single exponential fit is applied to the autocorrelation function and the polydispersity describes the width of the assumed Gaussian distribution.

2.3 Rheological characterizations

To understand the influence of strong bindings of naphthalene rings present in the CTAB/SHNC micellar system, we first examined the linear viscoelasticity of CTAB/SHNC solutions at 25 °C by varying the CTAB concentration while keeping the salt to surfactant concentration ratio fixed at $R = 0.32$, coupled by dynamic light scattering measurements. Next we focused on the semi-dilute CTAB/SHNC solution at [CTAB]=75 mM with salt to surfactant (CTAB/SHNC) concentration ratio at $R = 0.32$, and performed linear, transient, and nonlinear rheological characterizations at varying temperatures. Finally we compared both linear and nonlinear rheology behavior of CTAB/SHNC solution with that of CTAB/NaSal at the same salt and surfactant concentration ([CTAB]=75 mM), to shed more insight on the double benzene ring effect.

2.3.1 Linear and nonlinear rheology at 25 °C with varying CTAB concentrations

The rheological characterizations for micellar solutions at [CTAB] = 40 mM, 60 mM, and 75 mM with [SHNC]/[CTAB] molar ratio $R = 0.32$ were performed by using a stress controlled rheometer (Anton Paar MCR 502) with a cone and plate geometry, under steady shear and small amplitude oscillatory shear procedures at 25 °C, see Fig. 2.2. The rheological parameters are summarized in Table 2.1. For 60 mM and 75 mM CTAB/SHNC solutions, the plateau modulus G_0 and relaxation time λ_r (cross over of G' and G'') were determined directly from the frequency sweep data. For 40 mM CTAB/SHNC solution, G_0 and λ_r were obtained by fitting the experimental data to a single mode Maxwell model (see detailed fit

information in the supporting information).

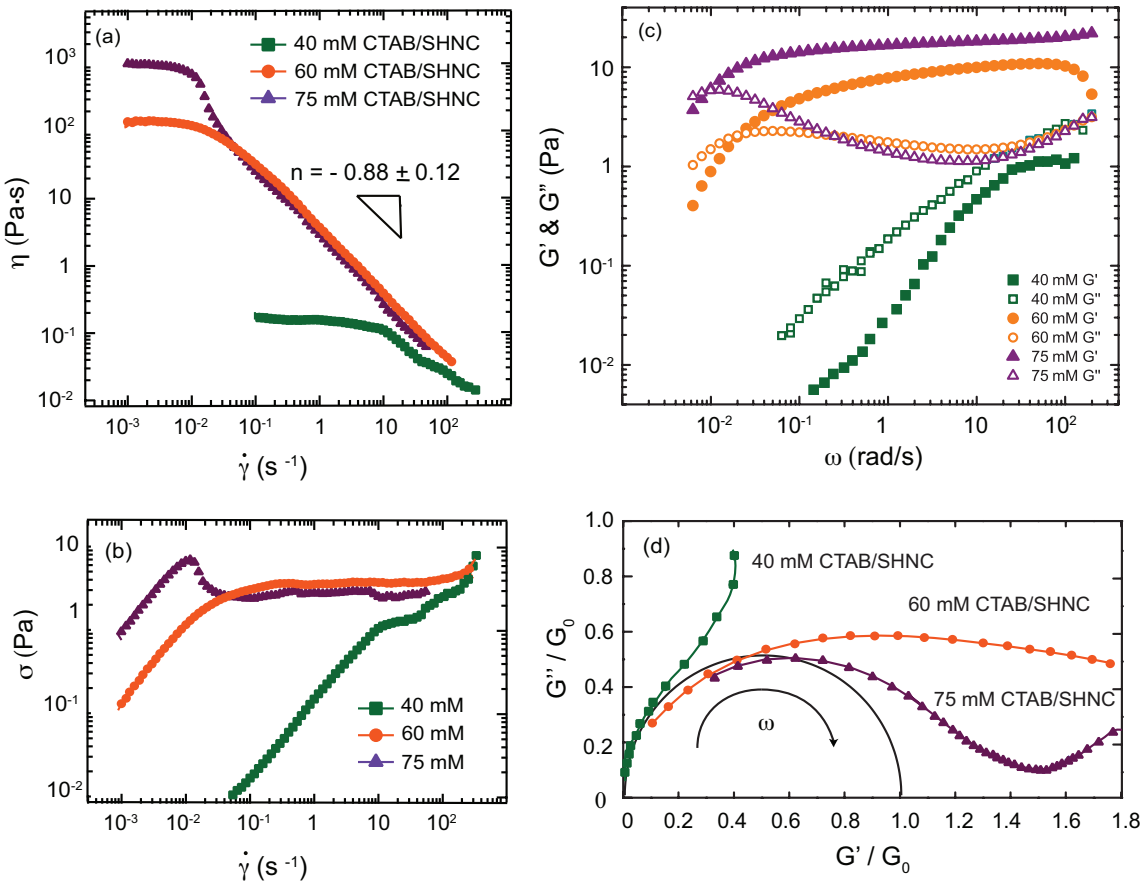

Figure 2.2: All three CTAB/SHNC solutions at 25 °C: (a) Shear viscosity and (b) shear stress as a function of shear rate under steady shear procedure; (c) The elastic modulus (G', filled symbols) and viscous modulus (G'', open symbols) are plotted as a function of frequency under small amplitude oscillatory shear at 10 % strain in a cone and plate geometry; (d) Normalized Cole-Cole plots.

In Fig. 2.2 (a), a dramatic increase in zero shear viscosity η_0 at [CTAB]= 60 mM (∼100 Pa.s) and 75 mM (∼1000 Pa.s) was observed by Khatory et al.[232] when compared with that of 40 mM CTAB/SHNC solution, indicating a substantial length increase of worm-like micelles at higher surfactant concentrations. In particular, CTAB/SHNC solutions at [CTAB]= 60 mM and 75 mM exhibited strong shear thinning behavior in more than 3

decades of shear rates and $\eta(\dot{\gamma})$ was well fitted by a power law relation with the power index $n = -0.88 \pm 0.21$. In the shear stress versus shear rate curves (Fig. 2.2 (b)), a stress plateau was observed for 40 mM CTAB/SHNC solution over a narrow shear rate range, while 60 mM CTAB/SHNC solution exhibited typical shear banding behavior with a shear stress plateau σ_p extending between low and high shear rates branches in the wormlike micellar solution[54,85,86,88,96,109,233,234]. In contrast to the 60 mM solution, 75 mM CTAB/SHNC solution achieved a σ_{max} much larger than the stress plateau σ_p at a low shear rate $\dot{\gamma}_1$ before reaching the shear stress plateau. Grand et al.[235] suggested that the appearance of a stress maximum was indicative of the existence of a transient branch with a stress larger than σ_p. It was proposed that the maximum shear stress could be estimated by $\sigma_{max} = 0.67G_0$ (G_0 the plateau modulus), occurring at a shear rate of $\dot{\gamma}_1 = 2.6/\lambda_r$ for an ideal Maxwell fluid[85,235,236]. Since our 75 mM CTAB/SHNC solution is not an ideal Maxwell fluid, we observed that $\sigma_{max} \sim 0.64G_0$ and the critical shear rate for the maximum stress was around $\dot{\gamma}_1 \sim 1.1/\lambda_r$ ($\lambda_r = 100.4$ s) (see Fig. 2.2 (b)). Nevertheless the product of $\dot{\gamma}_1 \times \lambda_r = 1.1$ lies within the range of (0.94–1.53), consistent with the range of values reported for wormlike micellar systems with non-ideal Maxwellian behavior[235]. Fig. 2.2 (c) shows the elastic modulus G' and viscous modulus G'' being plotted against the frequency ω in the linear viscoelastic regime at 10 % strain for all three solutions, at 25 °C. The stress relaxation time λ_r for 60 mM and 75 mM CTAB/SHNC solutions can be obtained from the crossover frequencies while 40 mM CTAB/SHNC solution showed weakly viscoelastic response without a crossover in the frequency range tested. Normalized Cole-Cole plots for all three solutions are shown in Fig. 2.2 (d) with the solid black curve corresponding to the single-mode Maxwellian linear viscoelastic model. Fig. 2.2 (d) illustrates that viscoelastic 75 mM CTAB/SHNC solution does not follow the single-mode Maxwellian model, while 40 mM and 60 mM CTAB/SHNC solutions deviate even further from the semicircle and no obvious G''_{min} is observed. Shikata et al.[237] argued that the deviation from the single Maxwell model behavior is caused by the low salt to surfactant molar ratio and low surfactant concentrations, with wormlike micelles in varying lengths in solutions (see Table 2.1), leading to a spectrum of relaxation times.

Compared with the linear rheological characterizations at 25 °C performed by Dubash et al.[4] with the same surfactant [CTAB] = 75 mM and 100 mM with [NaSal]/[CTAB]=0.32, a similar trend of increasing viscoelasticity with increasing CTAB concentration was observed, see Table 2.1. We observed that both the zero shear viscosity η_0 and relaxation time λ_r were 3 orders of magnitude higher in the 75 mM CTAB/SHNC solution than those of 75 mM CTAB/NaSal solution, while the plateau modulus G_0 was only two times higher. In the entangled regime, plateau modulus G_0 only depends on the entanglement mesh size, thus, the difference in these rheological parameters would be indicative of micelle persistence length difference in CTAB/NaSal and CTAB/SHNC systems. Note that the 75 mM and 100 mM CTAB/NaSal solutions reached a non-monotonic shear stress plateau without any stress maximum[4], which is consistent with the argument that the counterions from the salt at the micelle surface may change the micelle stiffness and interactions between the neighboring micelles[10,183]. On the one hand, the extra tail in CTAB/SHNC reduces the curvature of CTAB micelles more significantly when compared with the CTAB/NaSal micelles, facilitating elongated micelle formation with smaller packing parameters in CTAB/SHNC micelles. On the other hand, the naphthalene structure in CTAB/SHNC micelles is more hydrophobic than the salicylate ions in CTAB/NaSal micelles. In order to shield themselves from water, the HNC^- ions tend to form either $\pi - \pi$ bonds with another naphthalene ring or cation$-\pi$ bonds with adjacent hydrophobic CTAB headgroups, as illustrated in Fig. 2.1. These non-covalent bonds are much stronger than hydrogen bonds, and can increase the shear viscosity and micelle relaxation time of CTAB/SHNC solutions significantly. This argument can be applied to another set of sample parameters: the η_0 and G_0 in 60 mM CTAB/SHNC solution are comparable with those in 100 mM CTAB/NaSal solution, but the relaxation time λ_r in 60 mM CTAB/SHNC solution is much longer when compared with that of 100 mM CTAB/NaSal solution, due to stronger interactions between noncovalent bonds and high viscosity in the CTAB/SHNC solution that hinder the breakup of micelles in the system[191].

The diffusivity constant D and hydrodynamic correlation length ξ_H for all three CTAB/SHNC solutions were obtained by performing DLS (see section II for experimental details), as shown

Table 2.1: Rheological properties of CTAB/SHNC and CTAB/NaSal solutions at 25 °C

Samples	η_0 (Pa.s)	G_0 (Pa)	λ_r (s)	ξ_m (nm)
40mM(S)	0.20±0.02	1.2±0.5	0.3±0.1	202±12
60mM(S)	100±5	10±1	50.3±0.5	74.4±7.5
75mM(S)	1000±9	13±2	101±2	68.1±7.6
75mM(N)[4]	2.5±0.3	6.0±0.6	0.21±0.03	88.2±8.9
100mM(N)[4]	126±2	12±2	6.4±0.7	60.3±5.9

in Table 2.2. Nemoto *et al.*[223–225] reported that the diffusion coefficient D depended on both surfactant concentration C_d and salt to surfactant concentration ratio R in an aqueous CTAB/NaSal solution. When a small amount of salt was added, the wormlike micellar network would entangle while the electrostatic repulsion would increase the diffusivity D and suppress the hydrodynamic correlation length ξ_H, see Eq.2.12. Cates and Candau[198] suggested that scaling prediction of hydrodynamic correlation length ξ_H on surfactant concentration could be inferred from the scaling of micelle mesh size ξ_M, if the average micelle size was large compared with the network mesh size. However, this argument was not valid in CTAB/SHNC solutions with low salt concentration, which exhibit polydispersity in micelle length and deviation from the single Maxwell model (see the polydispersity information in Table 2.2). Cates et al.[198] also proposed that the monotonic decrease of ξ_H with increasing surfactant concentrations implied strong interactions among micelles, either through entanglements or the formation of micelle crosslinks. Since the crosslink formation in CTAB/SHNC system is not favorable with a low decreasing exponent of ξ_H ($\sim$0.1), the entangled micelle network is likely to be more dominant in our CTAB/SHNC solutions.

Among the three CTAB/SHNC solutions examined, a distinct stress bump was observed for 75 mM CTAB/SHNC solution (see Fig. 2.2 (b)), implying possible transient behavior induced by double benzene rings in the system. To further investigate the binding stability of naphthalene micelles in 75 mM CTAB/SHNC solution, we conducted systematic linear,

Table 2.2: Diffusivity of CTAB/SHNC and CTAB/NaSal solutions at 25 °C

Samples	ξ_H (nm)	D (10^{-10} m^2/s)	Polydispersity
40mM(S)	14.5±1.9	0.15±0.03	0.33±0.06
60mM(S)	12.5±1.5	0.17±0.03	0.32±0.05
75mM(S)	11.3±1.2	0.19±0.04	0.28±0.04
75mM(N)[4]	10.0±1.3	0.21±0.04	0.29±0.04
100mM(N)[4]	7.8±0.9	0.27±0.05	0.26±0.02

transient, and nonlinear rheological characterizations with temperatures varying from 20 °C to 40 °C, with comparisons to that of 75 mM CTAB/NaSal solution, see details below.

2.3.2 Rheological characterizations of 75 mM CTAB/SHNC solution

Linear rheology with elevating temperatures

Steady shear flow and small amplitude shear oscillations were performed on 75 mM CTAB/SHNC solution at temperatures between 20 °C and 40 °C. Comparison in steady shear flow behavior was made between CTAB/SHNC and CTAB/NaSal solutions ([CTAB] = 75 mM) at selected temperatures (see Table II). Fig. 2.3 (a) shows that CTAB/SHNC solution shear thinned and $\eta(\dot{\gamma})$ can be fitted by a power law index of $n = -0.88 \pm 0.21$ for all temperatures. Even though zero shear viscosity η_0 dropped dramatically with increasing temperatures, η_0 remained above 10 Pa.s at 40 °C and exhibited shear thinning at higher shear rates. On the contrary, the single benzene ring system (75 mM CTAB/NaSal solution) was sensitive to temperature variations (see inset in Fig. 2.3(a)), with η_0 reducing to ≤ 0.01 Pa.s at 40°C and behaving like a Newtonian fluid. Table II tabulates all the key rheological parameters from these measurements. The relative stability at high temperatures for the CTAB/SHNC system can be attributed to the long relaxation time of micelles with strong non-covalent interactions from the naphthalene ring. In addition, HNC^- ions became less hydrophobic

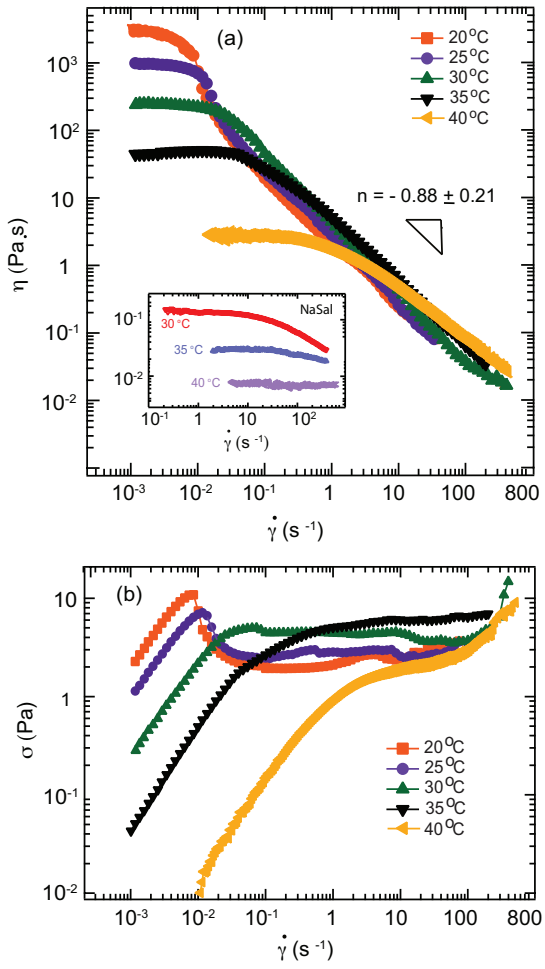

Figure 2.3: (a) Shear viscosity as a function of shear rates for 75 mM CTAB/SHNC solution at different temperatures under steady shear, with inset showing the viscosity variations in 75 mM CTAB/NaSal system. (b) Shear stress as a function of shear rates for 75 mM CTAB/SHNC solution at different temperatures under steady shear.

at higher temperatures, adapting to a closer binding to the micellar surface to prevent micelle breakup. In Fig. 2.3(b), a maximum shear stress was observed at 20 °C and 25 °C around shear rates $\dot{\gamma}_1 \sim 1.1/\lambda_r \approx 0.01$ 1/s, followed by a shear stress plateau. At higher temperatures, stress overshoot was significantly diminished before reaching a shear stress plateau.

The shear stress overshoot of aqueous CPyCl/NaSal (100 mM/60 mM) system has been reported by Grand et al.[235] in the temperature range of 20 °C – 25 °C. The steady state shear rate $\dot{\gamma}$ in the low shear band corresponded to the largest shear stress σ. This stress overshoot was termed as "top–jumping", in which case a transient branch exists with a stress larger than the shear stress plateau σ_p. The time scale to relax this transient state to a "truly" steady state flow is much longer than the Maxwell relaxation time of the micellar solution. Grand et al.[235] estimated this time scale $\sim (\dot{\gamma} - \dot{\gamma}_c)^{-p}$, with p depending on the chemical composition and temperature of the solution. Berret et al.[85] also observed stress overshoot in a 0.5 M NaCl solution containing CPyCl and NaSal ($R = 0.5$ with total surfactant concentration of 12%). Their stress overshoot was due to the nucleation and growth of a shear induced nematic phase, which is not applicable to our low weight fraction ($\phi < 5\%$) surfactant system. More discussion can be found in the section of transient rheology on page 24.

In Fig. 2.4 (a), we plot the elastic modulus G' and viscous modulus G'' versus the angular frequency ω in the linear viscoelastic regime with 10% strain, for 20 °C – 40 °C. The stress relaxation time λ_r was then determined from the first crossover regime of G' and G'' curves and a descending trend was observed with increasing temperatures. The plateau modulus G_0 was obtained as the plateau value of G' from Fig. 2.4 (a), listed in Table 2.4. The key rheological parameters (i.e., η_0 and λ_r) were very sensitive to temperature variations and could be described by the Arrhenius relations in[198]

$$\lambda_r = A \exp(\frac{E_a}{\bar{R}T}) \quad and \quad \eta_0 = G_0 \exp(\frac{E_a}{\bar{R}T}) \tag{2.13}$$

where E_a is the flow activation energy, $\bar{R}$ the gas constant, and T the absolute temperature. The inset in Fig. 2.4 (a) showed that both λ_r and η_0 could be linearly scaled with $1000/T$ with

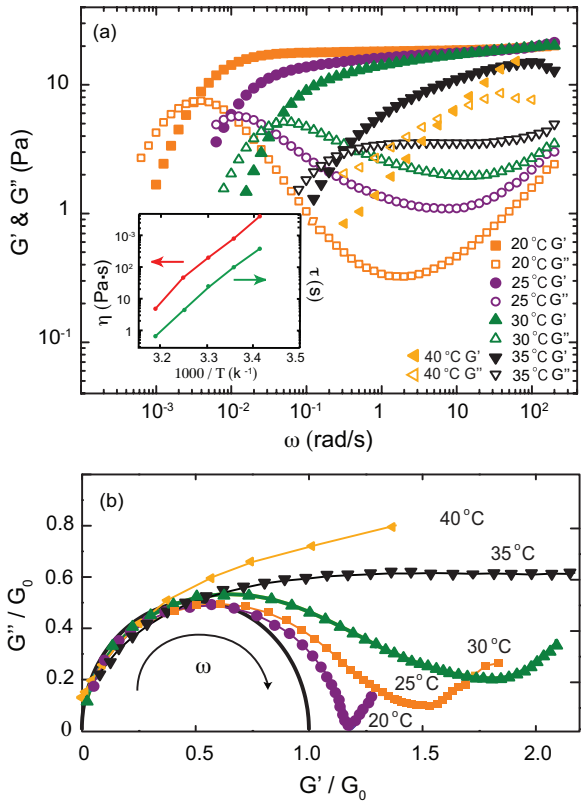

Figure 2.4: (a) The storage modulus (G', filled symbols) and loss modulus (G'', open symbols) as a function of frequency for 75 mM CTAB/SHNC solution at different temperatures under small amplitude oscillatory shear flow. The inset exhibited the Arrhenius relations for λ_r and η_0. (b) Normalized Cole–Cole plots for 75 mM CTAB/SHNC solution at different temperatures.

similar slopes. The flow activation energy E_a obtained from the λ_r Arrhenius relationship yielded E_a ∼192.3 kJ/mol, while the η_0 Arrhenius relationship resulted E_a ∼206 kJ/mol. These two estimated E_a values are within 7% difference and are also consistent with previous reported range of E_a values (70-300 kJ/mol) by Han et al.[238]. The plateau modulus G_0 extracted from the Arrhenius relation (G_0 ∼13 Pa) is also consistent with the frequency sweep measurements at varying temperatures, indicating that although the average micelle length decreased in the system as a function of temperature, the micelles stayed mostly intact with consistent flow activation energy.

Table 2.3: Rheological properties of 75 mM CTAB/SHNC solution at different temperatures

T (°C)	η_0 (Pa.s)	G_0 (Pa)	G''_{min} (Pa)	$\frac{G''_{min}}{G_0}$	λ_r (s)
20	3920±40	13±2	0.30±0.04	0.02±0.03	317±3
25	1000±9	13±2	1.1±0.3	0.09±0.01	101±2
30	240±21	13±2	2.0±0.3	0.15±0.02	25.2±3.3
35	47±5	12±2	3.6±0.5	0.30±0.04	3.2±0.6
40	1.8±0.2	11±1	5.0±0.5	0.45±0.03	0.41±0.04

Table 2.4: Characteristic length of 75 mM CTAB/SHNC solution at different temperatures

T (°C)	ξ_m (nm)	l_e (nm)	$\bar{l}$ (μm)	ξ_H (nm)	D (10^{-10} m^2/s)
20	67.8±7.5	185±15	9.3±1.5	12.6±1.3	0.16±0.03
25	68.1±7.6	187±15	2.1±0.2	11.3±1.2	0.19±0.04
30	68.5±7.9	189±17	0.95±0.13	9.8±1.1	0.23±0.05
35	70.8±8.2	199±19	0.62±0.06	8.7±0.9	0.26±0.05
40	73.2±8.9	211±20	0.41±0.03	8.2±0.9	0.30±0.06

Normalized Cole-Cole plots for 75 mM CTAB/SHNC at four different temperatures are shown in Fig. 2.4 (b) with the solid black curve corresponding to the single mode Maxwell

model. All curves agree well with the semi-circle at low frequencies, but display an increasing deviation from the semi-circle with increasing frequencies, accompanied by an apparent dip of G''_{min} and an upturn of G'', which are related to Rouse and breathing modes by Granek et al.[200]. The depth of G''_{min} in the experimental data provides a semiquantitative estimate of the ratio of $l_e/\bar{l}$ by Eq.2.3, where $\bar{l}$ represents average micellar length in the system and l_e is the length for micellar chains between entangled points. At 20 °C and 25 °C, the ratio of G''_{min}/G_0 is 0.02 and 0.09 respectively, suggesting that the average chain length $\bar{l}$ is much longer than the micelle entanglement length, consistent with the fact that η_0 and relaxation time λ_r are higher at the 25 °C. When the ratio of G''_{min}/G_0 increased further, the dip of G''_{min} got shallower at 30 °C and finally disappeared at 35 °C and 40 °C, in which case the micelle chains were only a few times of the entanglement length and the micelle break up time became comparable with the entanglement time.

Following the Poisson renewal model, we estimated the entanglement mesh size ξ_m from Eq.2.2 and further obtained the entanglement length l_e and average micelle length $\bar{l}$ of 75 mM CTAB/SHNC solution from Eq.2.3 and Eq.2.4 respectively, see Table 2.4. Note that a significant decrease of $\bar{l}$ and λ_r was observed while the entanglement mesh size ξ_m was not strongly affected by elevating temperatures, implying that entangled micellar network almost remained intact even though the micelles were easier to break and reform at high temperatures. This observation is consistent with the hydrodynamic correlation length obtained from DLS measurements. A monotonic increase in micelle diffusivity D implies increasing thermal agitation of micelles, while the corresponding ξ_H remained $\sim 10 \pm 1.5$ nm for all temperatures tested, suggesting that the hydrodynamic properties in the CTAB/SHNC solution were not strongly affected in the temperature range we investigated[225]. However, the competition between various time scales under elevating temperatures can yield interesting transient and nonlinear rheological behaviors, see details below.

Transient rheology

Hydrophobic HNC^- ions have shown sensitive temperature responses: HNC^- ions can desorb from the micellar surface, where $\pi-\pi$ and cation$-\pi$ bonds between micelles become weakened with increasing temperatures with excessive HNC^- in a micellar solution by Kalur et al.[191]. Here we employed both startup shear and shear hysteresis flow procedures to probe the transient rheology behavior of 75 mM CTAB/SHNC solution.

Start up shear: Since a pronounced stress overshoot of 75mM CTAB/SHNC solution was observed at 20 °C (orange curve in Fig. 1.2 (b)), shear stress σ was plotted against shear strain γ at different shear rates ($\dot{\gamma} = 0.0005-10$ s^{-1}) at 20 °C, see Fig. 2.5. In the upper inset we plotted shear stress versus shear rate from the steady shear flow procedure and was divided into 2 regimes. Regime 1 is the low shear rate branch/elastic deformation regime where shear rate $10^{-3} \leq \dot{\gamma} \leq 0.01$ s^{-1}. Regime 2 is the shear banding regime where $0.01 \leq \dot{\gamma} \leq 10$ s^{-1}. In the shear banding regime, homogeneous flow of wormlike micellar solutions can become unstable and separate into coexisting shear bands with different local viscosities and internal structures[30,77,78]. Macroscopic rheology coupled with local measurements such as nuclear magnetic resonance[79,80], dynamic light scattering by Salmon et al.[81], PIV by Hu et al.[82], high frequency ultrasonic velocimetry[83,84], rheo-optics by Lerouge et al.[54], spatially-resolved SANS measurements in the flow-gradient plane[93,99,239,240], and a combination of different techniques have been widely used to explore the complex spatio-temporal dynamics in the heterogeneous structures at the shear plateau regime[48,78,85–91,94–97,241].

Lower shear rates ($\dot{\gamma} = 0.001$ and 0.005 s^{-1}) were chosen in the low shear rate regime prior to shear banding. The maximum shear stress σ increased monotonically with imposed strain γ and continuous shear deformation. When the shear rate exceeds the reciprocal of the relaxation time $1/\lambda_r$ ($\dot{\gamma} \sim 0.01$ s^{-1}), σ reaches a maximum, then decreases over time. Shear rate $\dot{\gamma} = 0.01$ s^{-1} corresponds to the onset of the shear banding plateau, and $\dot{\gamma} = 10$ s^{-1} corresponds to the tail portion of the shear banding regime. Within this shear rate range, the stress versus strain curves for all chosen shear rates exhibit a similar slope before

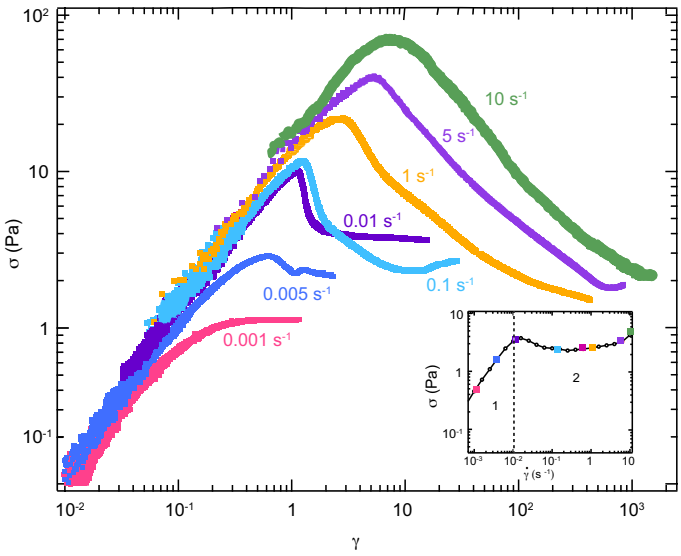

Figure 2.5: Transient shear stress plotted as a function of shear strain from the start-up experiments. The inset shows shear stress versus shear rates in the steady flow and was divided into 2 regimes. Regime 1 is the elastic deformation regime where shear rate $10^{-3} \leq \dot{\gamma} \leq 0.005$ s^{-1}. Regime 2 is the shear banding regime where $0.01 \leq \dot{\gamma} \leq 10$ s^{-1}.

reaching the maximum shear stress, and the shear stress would eventually approach a value that is consistent with the shear stress plateau σ_p, at different time scales for different shear rates (see light blue and gold curves). The relatively long time scale (longer than the stress relaxation time) to reach σ_p value is potentially related to micelles slowly relaxing back to a shear banding state, or caused by the chain alignment and orientation induced by shear deformation by Lu et al.[242].

Since start up experiments are susceptible to wall slippage[82,243–245], and flow heterogeneities in shear banding flow by Mewis et al.[246], nonlinear rheological characterizations were required to shed more insight.

Shear hysteresis: Shear hysteresis characterizations have been widely studied in gel-like fluids with thixotropic and viscoelastic properties[246–249]. The shear rate usually starts from a maximum value before being swept down to 10^{-3} 1/s, and ramped up to the original

maximum value. Transient shear stress can be plotted as a function of the shear rate and a hysteresis loop can be formed due to the lag between the shear stress and shear rate. The shape and area of the hysteresis loop are dependent on the shear history of a given material by Mewis et al.[246]. We investigated the shear hysteresis behavior for 75mM CTAB/SHNC solution at 20 °C, 25 °C, and 35 °C respectively, see Fig. 2.6. The initial shear rate was set to be $\dot{\gamma}_{up}$= 10 s^{-1}, then swept down to a low shear rate $\dot{\gamma}_{down} = 10^{-3}$ s^{-1} (red filled symbols), and subsequently increased back to $\dot{\gamma}_{up}$ (black filled symbols). Various time steps related to micelle relaxation times (approximately the same or half of or 1/10 th of) were chosen at different temperatures, see Fig. 2.6. The maximum shear rate (10 s^{-1}) was selected to ensure samples were not expelled from the geometry gap in any of the measurements.

Shear hysteresis with a geometry with a higher roughness: The data in Fig. 2.6 was collected by using a 50 mm and 1° smooth cone-plate geometry. In order test whether slip occurs on the geometry surfaces, we carried out shear hysteresis tests for 75 mM SHNC/CTAB solution with a rough geometry and confirmed that neither slip nor the shearing sequence (down–up and up–down) affected the results from similar testing using a 25 mm roughened parallel plate, see Fig. 2.7. In our laboratory, the only rough geometry we have available is a 25 mm parallel plate for our stress-controlled rheometer. We conducted a number of hysteresis experiments using a 25 mm smooth plate and the 25 mm roughened plate and the results were comparable with each other and with those presented in the manuscript (performed using a 50 mm smooth cone-plate). We showed shear hysteresis curves at two time stamp: δt = 50 s and δt = 10 s under 25 °C as an example, see Fig. 2.7. The difference is very minor, therefore we do not believe slip on the geometry surfaces is a major concern in most of our results performed with smooth cone-plate geometries. The following discussions would then focus on the shear hysteresis curve obtained in Fig. 2.6.

Referring to Table 2.4, the stress relaxation time of 75 mM CTAB/SHNC solution is around 317 s at 20 °C. By employing the slowest ramping rate $\delta t \sim \lambda \sim 300$ s, shear stress σ decreased sharply with decreasing shear rates first (red curve in Fig. 2.6 (a_1)), indicating an initial quenching/alignment of micelles under high shear rates. However, a slow recovery

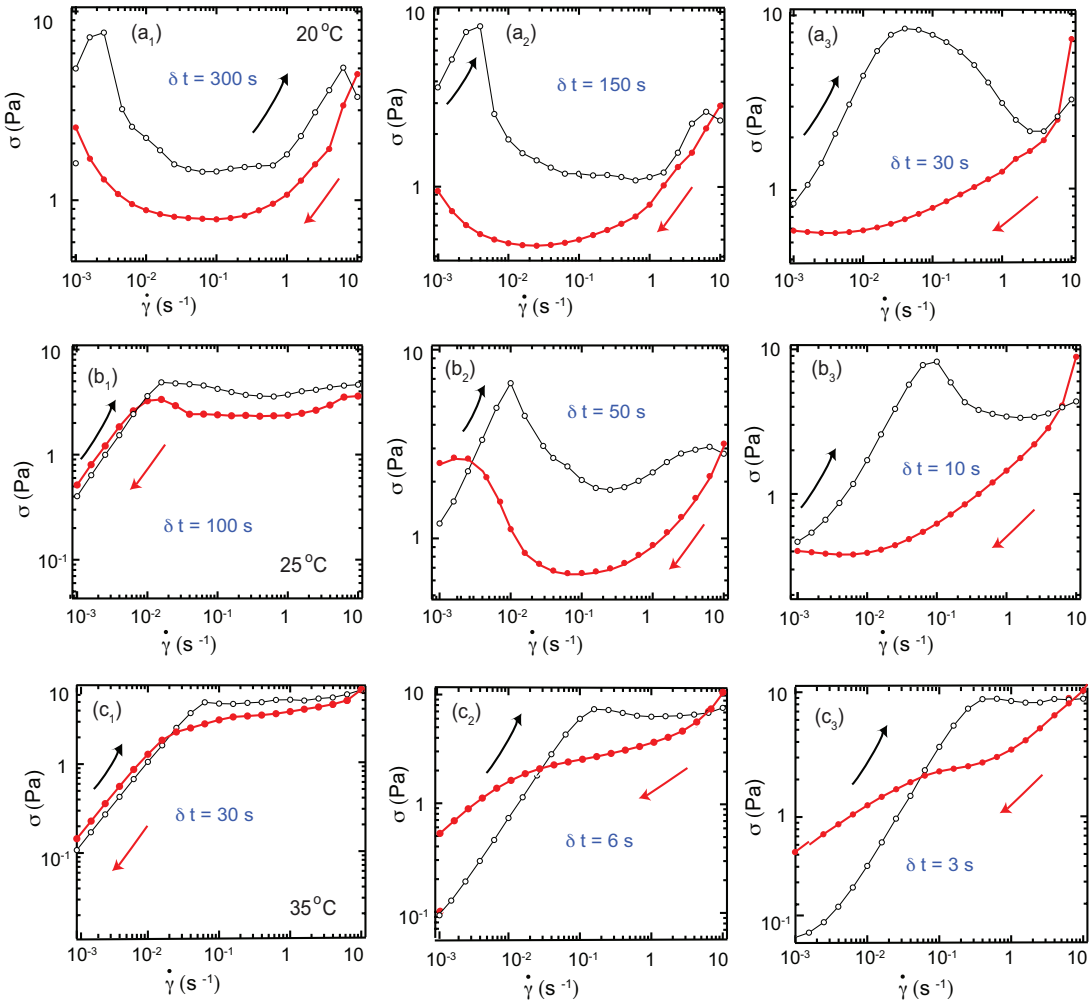

Figure 2.6: Flow curves of σ vs. $\dot{\gamma}$ of 75 mM CTAB/SHNC by ramping down the shear rate from $\dot{\gamma}_{up} = 10$ s^{-1} to $\dot{\gamma}_{down} = 10^{-3}$ s^{-1} (red symbols) and ramping up from $\dot{\gamma}_{down}$ to $\dot{\gamma}_{up}$ (black symbols) at (a_1-a_3) 20 °C; (b_1-b_3) 25 °C; (c_1-c_3) 35 °C. Different shear ramp durations related to the stress relaxation time at each temperature were marked with blue colors.

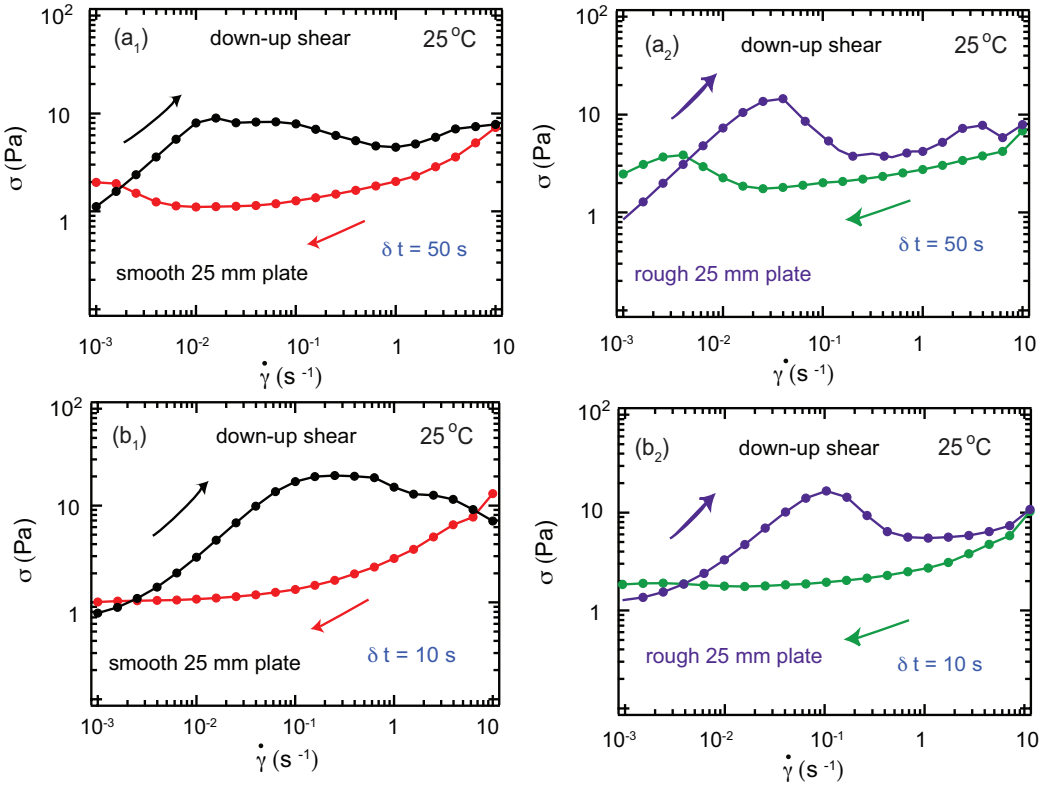

Figure 2.7: Flow curves of σ vs. $\dot{\gamma}$ of 75 mM SHNC/CTAB by ramping down the shear rate from $\dot{\gamma}_{up} = 10$ s^{-1} to $\dot{\gamma}_{down} = 10^{-3}$ s^{-1} (black and green dots) and ramping up from $\dot{\gamma}_{down}$ to $\dot{\gamma}_{up}$ (red and purple dots) for 25 mm smooth (a_1 and c_1)and rough parallel plate geometry (b_1 and d_1).

of shear stress appeared when $\dot{\gamma}_{down} < 0.01$ s^{-1}, with possible reconstruction of the micellar network since the ramping rate δt was very close to the micelle relaxation time. A stress overshoot emerged when the shear rates ramped up again, around 0.005 s^{-1}, which likely originated from heterogeneous shear bands. At faster ramping rates (δt = 150 s and δt = 30 s), the recovery of shear stress when ramping down was much less significant compared with δt = 300 s (see Fig. 2.6 (a_2) and (a_3)), since the micelles did not have time to restructure the gel network. However, the stress overshoot in the ramp up segment was still observed at higher shear rates with an increasing area of stress hysteresis loop.

At 25 °C, the stress relaxation time of 75 mM CTAB/SHNC solution is around 100 s. We again selected three distinct ramping rates corresponding to 1×, 0.5×, and 0.1× of the stress relaxation time. The stress overshoot and evolution trend at 25 °C are similar to those shown at 20 °C, but the stress was almost fully recovered when the ramping rate was equal to the micellar relaxation time at δt = 100 s, see Fig. 2.6 (b_1). Micelle contour length fluctuations[250,251], micelle chain stretch and convective constraint release (CCR) mechanism[155,252,253] have been widely studied to complement Doi-Ewards's tube model from Doi et al.[199] and Poisson renewal model from Granek et al.[200] by illustrating the transient stress response for shear thinning fluids. In our case, the micelles were initially stretched at high shear rates, the decrease of shear rates not only led to the stretch relaxation in the entangled network, but also enhanced the influence of the constraint release (the relaxation of oriented anisotropic micelles). The intramolecular interactions of non-covalent $\pi - \pi$ and cation–π bonds became less favorable at 25 °C and entangled micelles can be relaxed and re-oriented more easily.

At 35 °C, shear hysteresis patterns are different from those at 20 and 25 °C. The structures were able to fully recover at the slowest ramping rate δt = 30 s. When the ramping rates increased to 6 s shown in Fig. 2.6 (c_2) and 3 s in Fig. 2.6 (c_3), the residual stress increased rapidly with $\dot{\gamma}_{up}$, as the stress accumulated with the deformation before inducing breakage of micellar structures. This type of hysteresis loop has been reported in suspensions, foams and granular materials by Cruz et al.[254]. The shear hysteresis loop revealed an apparent

transition from strong thixotropic behavior at low temperatures to shear thinning property at higher temperatures in CTAB/SHNC wormlike micellar system.

Down-up and up-down shear hysteresis: In order to investigate whether there is a big difference from down-up and up-down shear hysteresis, We have performed both down-up shear hysteresis for a few tests. Shear hysteresis curves at two time stamp: δt = 50 s and δt = 10 s under 25 °C were presented below as an example, see Fig. 2.8 and the difference between up-down and down-up experiments is minor or negligible. Therefore, the hysteresis should still be observed when up-down shear tests are performed as we performed in the experiments.

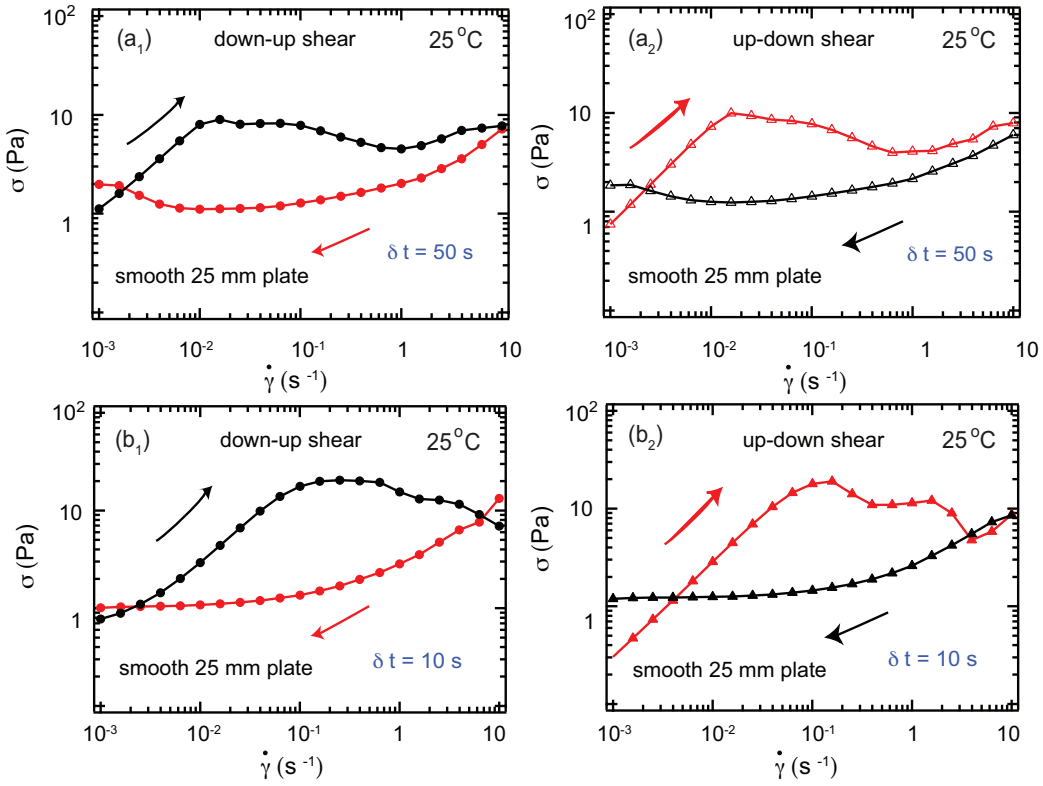

Figure 2.8: Flow curves of σ vs. $\dot{\gamma}$ of 75 mM SHNC/CTAB at 25 °C by ramping down the shear rate from $\dot{\gamma}_{up} = 10$ s^{-1} to $\dot{\gamma}_{down} = 10^{-3}$ s^{-1} and ramping up from $\dot{\gamma}_{down}$ to $\dot{\gamma}_{up}$ for (a_1) δt = 50 s; (b_1) δt = 10 s; ramping up from $\dot{\gamma}_{down}$ to $\dot{\gamma}_{up}$ first and ramp down from $\dot{\gamma}_{up}$ to $\dot{\gamma}_{down}$ for (a_2) δt = 50 s; (b_2) δt = 10 s.

Small angle light scattering (SALS) under transient shear flow

We have conducted Small angle light scattering (SALS) to investigate shear induced microstructure changes in coupled with our rheological measurement to illustrate the transient behavior. The experiments were carried out by Anton-Parr MCR 502 Rheo-SALS setting up, equipped with a 43 mm in diameter and a 1 mm in gap transparent parallel plate. The SALS laser light is emitted by a small laser diode and directed towards the sample by a prism, the scattering patterns during shear flow are recorded by a CCD camera. The birefringence index and dichroism are measured by He-Ne wavelength is 632.8 nm and the beam diameter of the He-Ne laser is 0.81 mm. Birefringence index represents the degree of micelle alignment and dichroism that indicates the turbidity that originate from new formed structures that absorb the light. When anisotropic structures are induced by shear or deformation forces, direct visualization showed the formation of turbid shear bands would be observed with enhanced intensity patterns oriented parallel and perpendicular to the flow direction Since we don't have enough time available to do a good job of this and it will be the subject of a more detailed study later on, we only presented the information we have so far.

In order to get a glimpse of shear induced transitions for SHNC/CTAB system 25 °C, we incrementally increased shear rates within 10^{-3} $s^{-1} \sim 10$ s^{-1} and recorded the birefringence index δn and dichroism, along with the real time images showing the changes of intensity with flow. At low shear rates where the shear rates are not high enough to align the micelles, the birefringence index is close to 0 and no measurable scattering is obtained from the sample, suggesting no large-scale structures were formed in the fluid. However, when the shear rate $\dot{\gamma}$ reaches to the critical $\dot{\gamma}_c$ where shear banding occurs, a bright streak was developed along the flow direction, indicating elongated structures aligned during the direction of the flow. We held each shear rates for around 1000 s, but no typical "butterfly" pattern that indicates the coupling of concentration fluctuation with scattering was observed. Instead, the micelles were aligned with flow directions first, forming a bright streak in the flow direction, another bright streak that oriented perpendicular to the flow appeared later. Both streaks existed

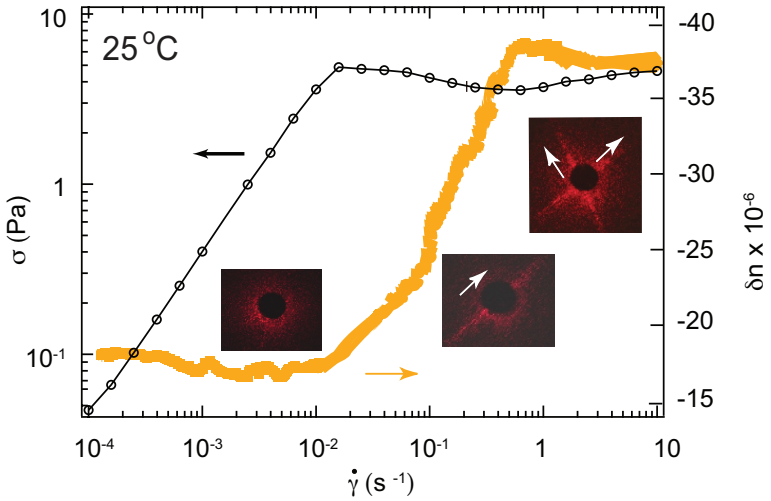

Figure 2.9: Plot of shear stress (left vertical axis) and birefringence index (right vertical axis) versus the shear rates. The inserted black images also shows that, the scattering pattens appear along the flow direction first and then develops in vertical flow direction as well in the shear banding regime

and the intensity of the streaks was enhanced and decreased periodically (see Fig. 2.9). Almost all the $\dot{\gamma}$ in the shear banding regime follow this pattern but the streak intensity increased and the period $\dot{\gamma}$ of reappearing decreased for higher $\dot{\gamma}$. Besides this, a periodically changed of dichroism also indicates the change of absorbance of light due to the formation of elongated structures. Therefore, SHNC/CTAB micelles exhibit strong elastic behavior under shear flow and it was the stretching and stress-orientation of micelles that dominated over the diffusion and concentration fluctuation of micelles during shear flow.

Nonlinear rheology: Large amplitude oscillatory shear flow (LAOS)

Since linear rheology provides limited information related to microstructural transitions in wormlike micellar solutions under flow, we conducted nonlinear rheological characterizations with large amplitude oscillatory shear flows (LAOS) to further reveal the naphthalene ring influence in micellar solutions under oscillatory flow field. LAOS employs accurate sinu-

soidal strain input to probe the microstructural transitions in a sample without causing edge failure of the sample by Blackwell et al.[208]. Accompanied by the results from linear and transient rheology procedures, LAOS illustrates a comprehensive picture of how wormlike micelles are affected by the cyclic switching on and off of the flow. As discussed earlier, the naphthalene ring can easily form stable non-covalent bonds that "arrest" micelles under simple shear flows and small deformations by Frounfelker et al.[182]. We envision that non-covalent bonds in CTAB/SHNC wormlike micellar solutions can be potentially decomposed under large deformations and thermal agitations. We focused on 75 mM CTAB/SHNC solution for the LAOS characterization in this section not only because of its strong viscoelastic properties, but also because its rheological properties can be compared with those of 75 mM CTAB/NaSal solution.

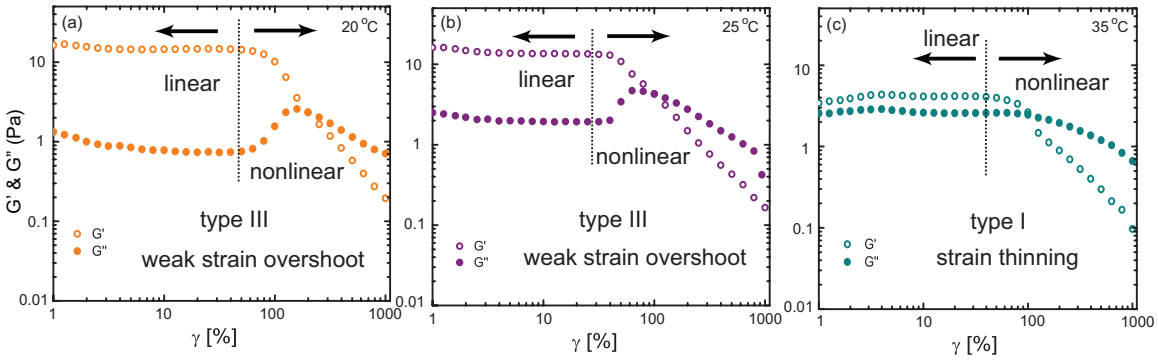

Figure 2.10: Strain Sweep for 75 mM CTAB/SHNC at (a) 20 °C; (b) 25 °C; (c) 35 °C from $\gamma = 1\% - 1000\%$ of strain and a frequency of 0.07 rad/s.

First, a strain sweep of strain $\gamma = 1\% - 1000\%$ for 75mM CTAB/SHNC solution from 20 °C to 35 °C was performed in order to identify its linear/nonlinear viscoelastic regimes, shown in Fig. 2.10. Hyun et al.[204,216] classified four types of LAOS response of complex fluids based on the strain sweep procedure: type I, strain thinning (both G' and G'' decreasing with increasing strains); type II, strain hardening (both G' and G'' increasing); type III, weak strain overshoot (G' decreasing, G'' increasing followed by decreasing); type IV, strong strain overshoot (G' and G'' both increasing followed by decreasing). There was a weak

overshoot of G'' at both 20 °C and 25 °C, corresponding to type III response. At 35 °C, the strain overshoot was smoothed out with a decrease in both G' and G'', corresponding to type I behavior. This strain sweep measurement provides limited insight of microstructure transition in the nonlinear regime. For example, the overshoot of G'' in type III response could be either due to the breakup and reformation of microstructures, or the viscous dissipation among microstructural clusters in the material by Hyun et al.[204,216]. Thus, even though type III behavior was observed for both 20 °C and 25 °C, further information in the nonlinear viscoelastic regime is needed to capture the microstructure evolution under flow by using LAOS measurements.

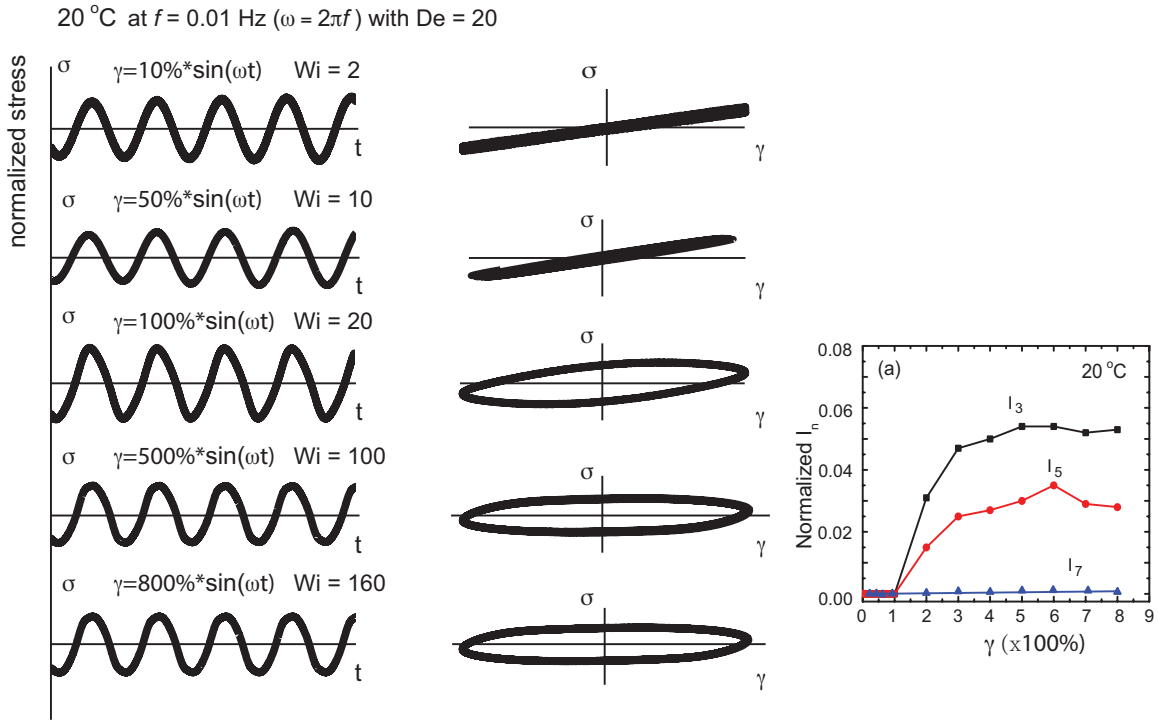

Figure 2.11: For 75 mM CTAB/SHNC solution at 20 °C, $f = 0.01$ Hz, $\omega = 2\pi f$ with De= 20: (a) stress response as a function of time; (b) Lissajous stress curves; (c) normalized high harmonic Fourier coefficients (I_3, I_5, I_7) under LAOS.

For 75 mM CTAB/SHNC solution, LAOS measurements were conducted by applying sinusoidal strain signals at γ of 10%, 50%, 100%, 500%, 800% at a fixed angular frequency

$\omega = 0.07$ rad/s, for three different temperatures (20 °C, 25 °C, 35 °C). The Deborah number De is defined as $De = \lambda_r \times \omega$, and the Weissenberg number $Wi = \gamma \times De$. Fig. 2.11(a) shows the shear stress (σ) response as a function of time and Lissajous normalized shear stress σ versus shear strain γ curves (Fig. 2.11(b)) at 20 °C. At $\gamma = 10\%$ and 50%, σ versus γ plots show a linear trend with a phase angle $\sim 4°$, consistent with the linear viscoelastic response shown in Fig. 2.10 (a). At higher strains $\gamma = 100\%$, 500%, 800%, the viscoelastic response becomes evident with an increase in the phase angle, reflected by a sinusoidal stress response with time (Fig. 2.11(a)) and elliptical Lissajous curves (Fig. 2.11(b)). To quantify the degree of nonlinearity in the stress response, higher order Fourier harmonic coefficients I_n (using Eq. (6 & 7)) were calculated by Fourier transforms of stress in the frequency domain and normalized by the first harmonic coefficient $I(\omega_1)$, see Fig. 2.11(c). The magnitude of these normalized coefficients can quantify the nonlinearity of the shear stress under large deformations. With increasing strain γ, I_3 and I_5 reached an asymptote with magnitudes less than 0.06 and a vanishingly small coefficient I_7.

At 20 °C, the stress relaxation time obtained from the SAOS measurement ($\lambda_r \sim 317$ s, see Table 2.4) is greater than the deformation time ($1/\omega \sim 100$ s) from the LAOS oscillation, hence the micelles were continuously deforming without being completely relaxed. It has been proposed that entangled wormlike micellar networks would "yield" when the time scale introduced by the flow is shorter than the intrinsic time scale (relaxation time λ_r) of the system. The "yield like" behavior exhibited in these systems is due to the entangled/disentangled micelle chains by Tapadia et al.[255,256], especially under periodic flow at large amplitudes. The imbalance of two forces, the elastic retraction force from shear, and the extension force from the entanglement points can induce disentangled chains, accompanied by the homogeneous elastic deformation within wormlike micellar networks by Wang et al.[257]. In our case ($\lambda_r > 1/\omega$), with increasing strain γ, the micellar networks kept on yielding and the stress was more likely to accumulate and relax in the entangled network, accompanied by the viscous dissipation during the deformation period.

At higher temperature 25 °C, linear viscoelastic response in 75 mM CTAB/SHNC solution

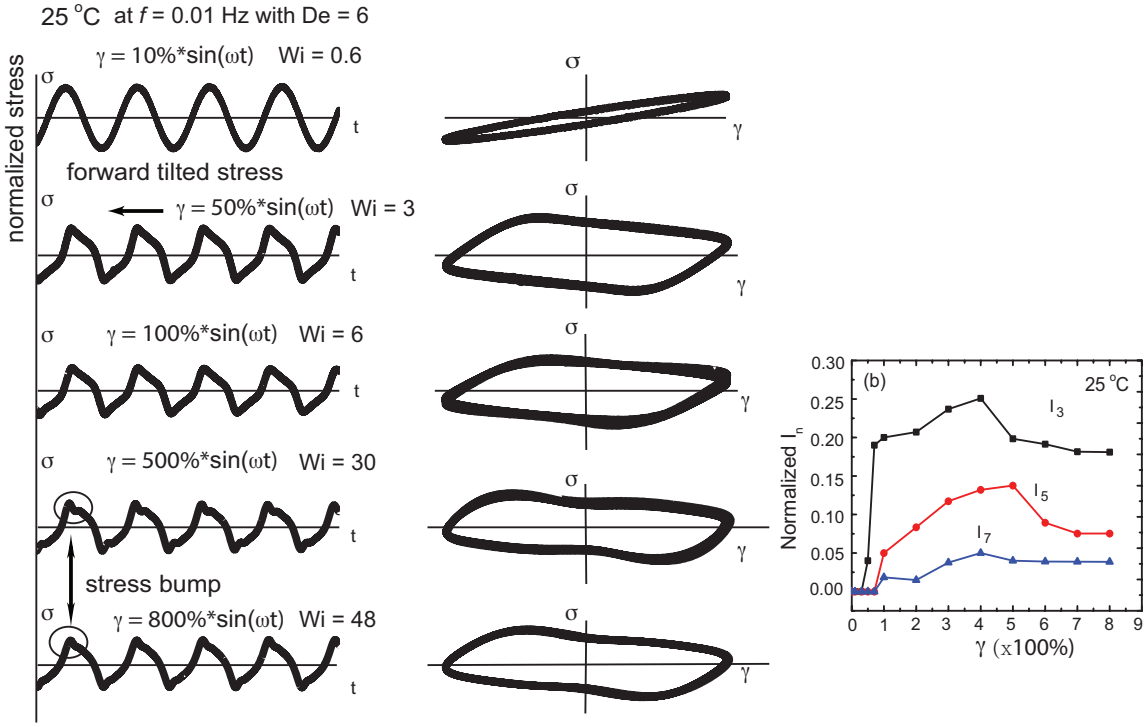

Figure 2.12: For 75 mM CTAB/SHNC solution at 25 °C, $f = 0.01$ Hz, $\omega = 2\pi f$ with De= 6: (a) stress response as a function of time; (b) Lissajous stress curves; (c) normalized high harmonic Fourier coefficients (I_3, I_5, I_7) under LAOS.

was observed at $\gamma = 10\%$ from the LAOS measurement. However, the micellar solution exhibited high nonlinearities with tilted stress curves (marked in Fig. 2.12) when $\gamma \geq 50\%$, showing a nonlinear viscoelastic response with distorted sinusoidal shaped stress versus time curve (forward tilted stress) and deformed elliptical shape of the Lissajous curve. Hyun et al.[214] observed similar deviations from sinusoidal shaped stress versus time response in a 4 wt% aqueous Xanthan gum solution. They proposed that the "forward tilted stress" was related to the linear chain structures that were isotropically distributed in the Xanthan gum solution, which may also align and associate to form a structured gel. The sharp increase in the stress signal in the Lissajous curve, termed as the "sticking" stress by Hyun et al.[214], was caused by short range potentials between two charged headgroups of polymer chains. At $\gamma = 500\%$ and 800%, we also observed stress bumps in the stress versus time curves,

see Fig. 2.12. Rogers et al.[209] also reported a stress bump for a soft colloidal solution under LAOS. They proposed the concept of the "cage" strain causing the stress bump: the colloidal glass system displayed an elastic response and sustained the deformation before reaching the "cage" strain. The stress buildup and breaking of microstructures consequently led to the stress bump. This "stick-slip" system would flow again when the strain rate reached zero, until the "cage" reformed and another stick-slip cycle began.

For our CTAB/SHNC solution at 25 °C, the structured micellar network was first deconstructed due to large deformation γ. However, since the deformation time scale $1/\omega \sim$100 s is very close to the longest micelle relaxation time, new noncovalent bonds could be formed when γ ceased during the cycle, accompanied by a significant reorganization of the micellar network due to the flow. In addition, short range interactions (electrostatic repulsions of positively charged CTAB headgroups, local frictions between micelles from the extra tail) between adjacent micelles could induce nonlinear stresses at large amplitude of strain, where rearrangements of $\pi - \pi$, cation$-\pi$ bonds all played important roles in short range interactions, generating "sticky" bumps observed in the stress curve. These short-range interactions between micelles that periodically decomposed and reformed within the oscillatory cycle played a significant role in the distorted rheological response.

High harmonic Fourier coefficients were calculated at 25 °C, shown in Fig. 2.12(c). Similar to the case at 20 °C, the normalized I_n (n = 3, 5, 7) increased with increasing strains due to entangled micellar networks, then reached an asymptote at higher strains, potentially caused by the viscous dissipation that smoothed out the nonlinearity. The harmonic coefficients at 25 °C were much higher than those I_n at 20 °C, implying that short-range electrostatic interactions and thermal agitations between micellar headgroups at higher temperatures played important roles in intensified nonlinearity. It can be inferred from Table 2.4 that at lower strain amplitudes, mesh size ξ_m remained unchanged, but the zero shear viscosity η_0 and relaxation time λ_r at 25 °C were much smaller compared with those of 20 °C. Thus, at large strain amplitudes, the micellar networks were easier to disintegrate into smaller clusters with a balance between viscous dissipation and intramolecular interactions during oscillatory

cycles.

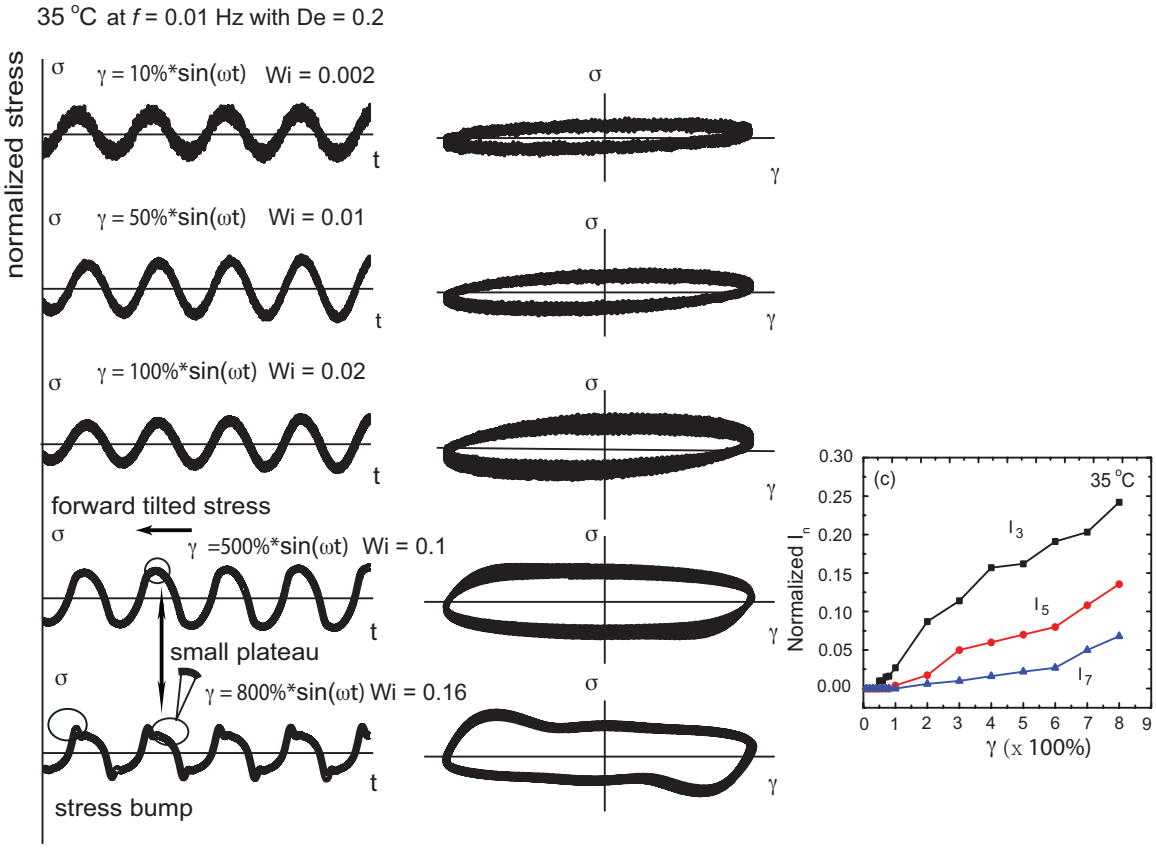

Figure 2.13: For 75 mM CTAB/SHNC solution at 35 °C, $f = 0.01$ Hz, $\omega = 2\pi f$ with De= 0.2: (a) stress response as a function of time; (b) Lissajous stress curves; (c) normalized high harmonic Fourier coefficients (I_3, I_5, I_7) under LAOS. $De = \lambda \times \omega$, and $Wi = \gamma \times De$.

With increasing temperature at 35°C, stress versus time curves showed a linear viscoelastic response for γ between 10% and 100%, followed by emergence of small plateaus and "forward tilted stress" at $\gamma = 500\%$ and $\gamma = 800\%$ (see Fig. 2.13), similar to the stress pattern observed at 25 °C with a $\phi_3 = 270°$, which appeared at relatively lower strains (i.e., $\gamma = 50\%$). Since the system at 25 °C and 35 °C exhibited distinct differences from both linear viscoelastic (Fig. 1.2) and strain sweep (Fig. 2.10 (c)) procedures, we propose that the underlying mechanism for the "forward tilted stress" observed in stress time curves was different at these two temperatures. At 35°C, deformation time ($1/\omega \sim 100$ s) was much slower

than the stress relaxation time ($\lambda_r \sim 3.2$ s) of the entangled micellar networks ($1/\omega >> \lambda_r$), meaning micellar networks have sufficient time to relax during the oscillation cycle. Clusters of micelles at large strain γ can then interact and break into small clusters at the maximum γ and reform continuously when γ was reversed, which corresponded to the stress bump observed in the stress curve periodically (see Fig. 2.13). In addition, small stress plateaus accompanied by the development of stress bumps were observed at 35°C, under $\gamma = 500\%$ and $\gamma = 800\%$ (see Fig. 2.13). This phenomenon is potentially related to "sliding" layers between micelles by Hyun et al.[214]: clusters can align and slide between each other under the flow direction before micellar networks break and reform, yielding a small plateau before the appearance of stress bumps. The normalized I_n (n = 3, 5, 7) at 35°C were also calculated and plotted in Fig. 2.13(c). There was a monotonic increase in I_n with increasing γ, indicating an increasing nonlinearity at this temperature, owing to the continuous break and reform of micelle clusters with higher thermal diffusivity. The hydrophobicity of HNC^- ions decreased with elevating temperatures, leading to weakened $\pi-\pi$ and cation$-\pi$ bonds. As a result, each extra benzene ring protruded out of micellar headgroups freely, adding frictions and interactions between micelles during flow that led to increased nonlinearity.

We have also conducted some preliminary tests at fixed value De= 20 under 20 °C ($f =$ 0.01 Hz), 25 °C ($f = 0.03$ Hz), and 35 °C ($f = 1$ Hz). The strain amplitudes for the LAOS are applied at $\gamma = 10\%$, 50%, 100% , 500% and 800%. Compared with the LAOS results for 20 °C at De = 20, the solution did not exhibit a nearly pure elastic response at 25 °C and 35 °C at low strain amplitudes $\gamma = 10\%$ and 50%. At higher strains $\gamma = 100\%$, 500%, 800%, the viscoelastic response became more evident for all three temperatures, reflected by more elliptical shaped Lissajous curves. These preliminary results show interesting features that deserve further investigation, which will be the topic of future work.

Dimitriou et al.[258] used Rheo-PIV to characterize the velocity profile and shear bands locations of wormlike micellar solution of 100 mM CPyCl and 60 mM NaSal in their LAOS measurements. They observed that the shear bands existed over the full cycle of the oscillation. Shear bands in our study might form and vanish during the LAOS cycle. We are

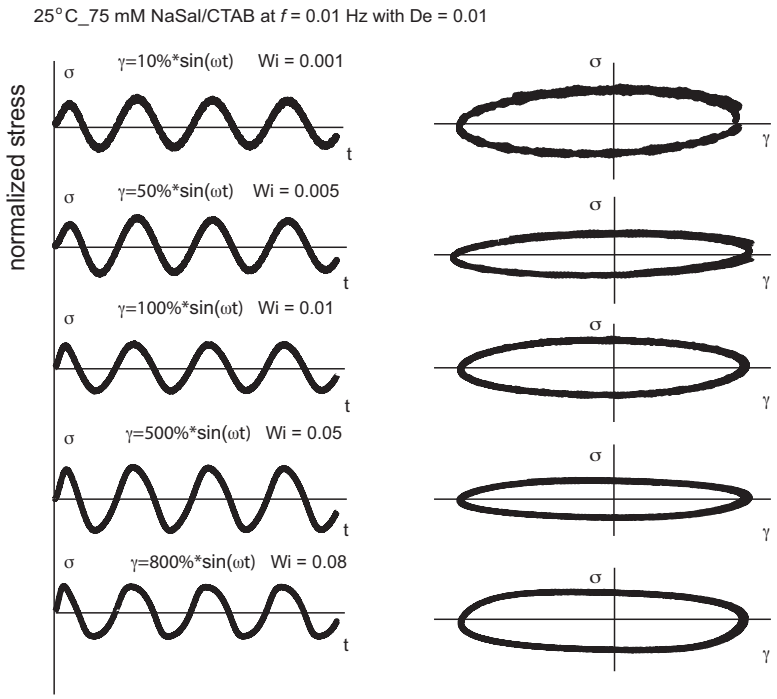

Figure 2.14: Stress response as a function of time (A) and Lissajous stress curves (B) for 75 mM CTAB/NaSal solution at 25 °C, $f = 0.01$ Hz, $\omega = 2\pi f$ with De= 0.01.

currently working towards developing a rheo-PIV system and we hope to be able to perform such experiments and report our results in the near future.

Comparing LAOS behavior of CTAB/SHNC at constant De

In order to decouple the effect of structure change and flow conditions, we performed more experiments by just holding *De* number constant while changing the oscillation frequency, (see Fig. 2.15). We have performed more experiments by holding $De = 20$ for 25 °C and 35 °C. Since it's taken incredibly long time for the fluid to get a low De at 20 °C, we decided to keep the $De = 20$ for 20 °C in the manuscript and added LAOS tests $f = 0.03$ Hz at 25 °C and $f = 1$ Hz at 35 °C, see Fig. 2.15, and the Fourier coefficients are extracted and plotted in the Fig. 2.15. As suggested by Morozov and vanSaarlos[259], for viscoelastic fluids, the combination of normal stress effects, intrinsic micelle properties (memory effects) and

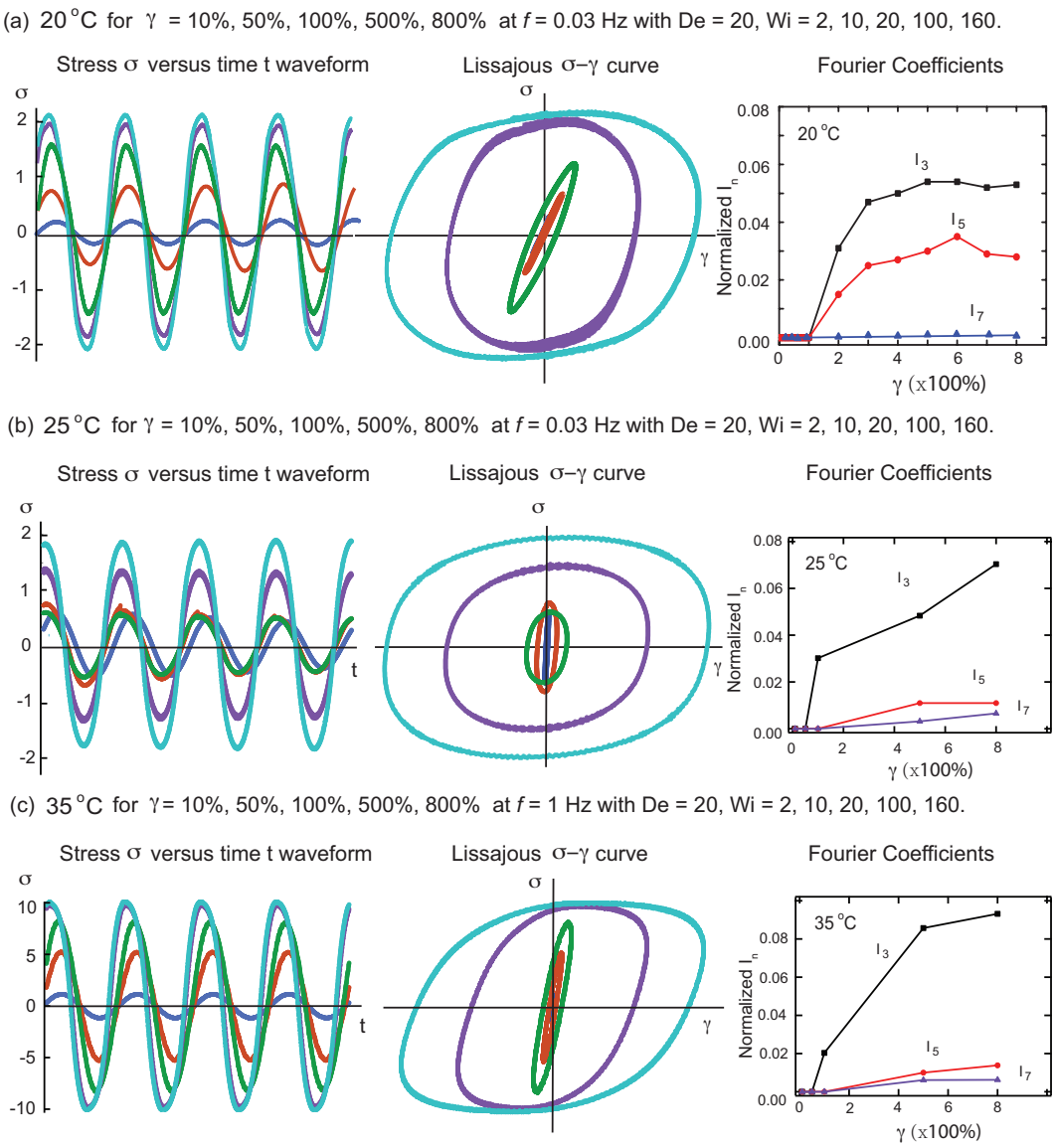

Figure 2.15: Plot of Lissajous curves (Torque versus angular displacement) under 20 °C (with a deformation time scale < micelle relaxation time λ_r), 25 °C (with a deformation time scale micelle relaxation time λ_r), 35 °C (with a deformation time scale > micelle relaxation time λ_r). Each Lissajous curve from the smallest circle to the largest circle corresponds to different strain at 10%, 50%, 100%, 500% and 800%.

the elastic effects, which are stored at high sheared region and released when the shear force decreases, are responsible for the onset of flow instabilities and nonlinearities. In our new tests, De is held constant, Wi is the same under same strain input, the flow conditions and elastic effects are decoupled. By compared the Lissajous curves and 3rd, 5th and 7th normalized Fourier Coefficients between 20 °C, 25 °C and 35 °C, we noticed the stress doesn't show significant nonlinearities and the three cases are very close to each other. The nonlinear stress response is more-likely elasticity-dominated and subcritical.

Comparing LAOS behavior of CTAB/SHNC and CTAB/NaSal solutions

To distinguish the extra benzene ring effect in the CTAB/SHNC solution, we compared LAOS measurements on both CTAB/SHNC and CTAB/NaSal solutions at the same surfactant and salt concentrations ([CTAB]=75 mM with $R = 0.32$), at 25 °C (see Fig. 2.14). The CTAB/NaSal solution exhibited less nonlinear viscoelastic response for all γ (see Fig. 2.14), while forward tilted stress was observed for the CTAB/SHNC solution at increasing γ (see Fig. 2.12). The zero shear viscosity and the stress relaxation time were significantly lower for CTAB/NaSal solution when compared with those of CTAB/SHNC system (see Table 2.1). At 25 °C, η_0 is 2.5 Pa s and λ_r is 0.21 s for CTAB/NaSal, while η_0 is 1000 Pa s and λ_r is 100 s for CTAB/SHNC system, suggesting faster breaking and reforming rates of micelles in CTAB/NaSal solutions. In the CTAB/NaSal system, the stress versus strain curve also exhibits more circular shaped Lissajous plots, with a phase angle close to 90°, corresponding to a more viscous response under the same large strain deformation. The quantitative comparison of the nonlinearity of the two solutions can be highlighted by plotting Fourier spectrums at $\gamma = 500\%$ and 25°C. Fig. 2.16 (a) illustrated the rich nonlinear behavior of CTAB/SHNC solution with relatively high I_3, I_5 and I_7 at the frequency range from 0 – 0.1 Hz. By contrast, the stress response in the CTAB/NaSal solution exhibited vanishing higher harmonic Fourier coefficients (see Fig. 2.16 (b)).

These comparisons demonstrated that the strong hydrotropic salt SHNC with dual benzene rings induced pronounced viscoelasticity when compared to that of CTAB/NaSal so-

lution. The strong hydrophobicity and high surface activity of SHNC molecules can yield stronger noncovalent interactions between adjacent micelles as hydrophobic HNC^- ions need to be shielded from water to stabilize these micelles. Consequently, domains of π–π ions are paired and cation–π groups are formed between HNC^- ions and adjacent hydrophobic CTAB headgroups, inducing stable and extensible micellar networks that exhibit versatile response under large deformations and temperatures. In particular, for 75 mM CTAB/SHNC solution, micellar network formed with π–π ions are paired and cation–π groups exhibit stability under different temperatures from 20 °C to 40 °C. Despite the increasing diffusion coefficient D at higher temperatures that led to more agitated interactions of micelles, the Arrhenius relationship remained valid.

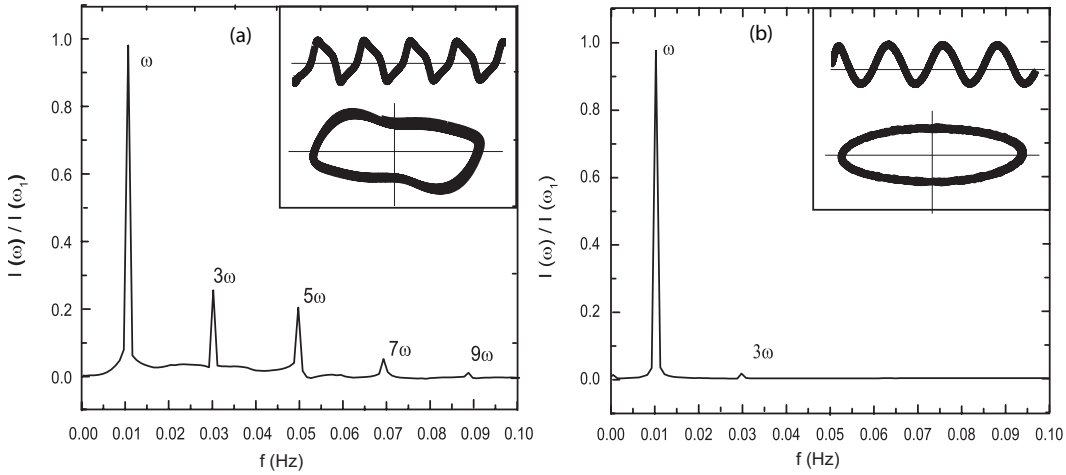

Figure 2.16: Fourier coefficient spectrum at $\gamma = 500\%$ under 25 °C (a) 75 mM CTAB/SHNC solution and (b) 75 mM CTAB/NaSal solution. The inserted images are plots of stress versus time curve and Lissajous curve at this particular strain and temperature.

2.4 Concluding remarks

We performed both linear and nonlinear rheological characterizations of an aqueous mixture of cationic surfactant CTAB and hydrotropic organic salt SHNC in the semi-dilute regime, coupled with dynamic light scattering measurements. With SHNC as counter ions, domains

of $\pi - \pi$ ions were paired and cation–π groups were formed between HNC^- ions and adjacent hydrophobic CTAB headgroups, inducing more viscoelastic and stable micellar networks compared with that of the CTAB/NaSal system. By focusing on 75 mM CTAB/SHNC solution, we observed a rich variety of nonlinear rheological behaviors under different deformation histories with temperatures ranging from 20 °C to 40 °C. Since the naphthalene ring can easily form stable noncovalent bonds that "arrest" micelles under simple shear flows and small deformations by Frounfelker et al.[182], when the deformation time is short compared with micelle relaxation time λ_r at 20 °C, the viscous dissipation is dominant at higher deformation. At 25 °C where the two time scales are comparable, yielding like behavior occurs and is accompanied by short range interactions between micelle head groups. At 35 °C, when the deformation time is much faster compared with λ_r, micelle network breaks and recombines at a fast rate and lead to more frequent interactions.

More specifically, for LAOS and shear hysteresis flow measurements of CTAB/SHNC solutions conducted at different temperatures, two important time scales emerged: deformation time scale from the flow procedure, and the longest micelle relaxation time as an intrinsic material time scale. we adopted the continuous Lissajous plot to illustrate the transient behavior in 75 mM SHNC/CTAB system under 20 °C, 25 °C, 35 °C (see Fig. 2.17).

At 20 °C, the micelle network was "soft" (with low harmonic Fourier coefficients) but the rearrangement of micelles were hindered due to the high viscosity of the solution. As a result, the "soft" gel continued "yielding" and the progressive alignment and stretching during the flow led to strong and heterogeneous localization of stresses in the entangled networks, with relatively high viscous dissipation during the cycle. At 25 °C and 35 °C, while the micelles were shorter and more mobile, a reorganization of entangled networks and short range interactions between adjacent micelles became more dominant. Meanwhile, reformation of new non-covalent bonds occurred during the deformation period since the micelle relaxation time was shorter. Moreover, additional stress relaxation mechanisms such as contour length fluctuations of reptation chains and constraint release from the motion and rearrangement of neighboring chains, might play an important role in the micelle relaxation

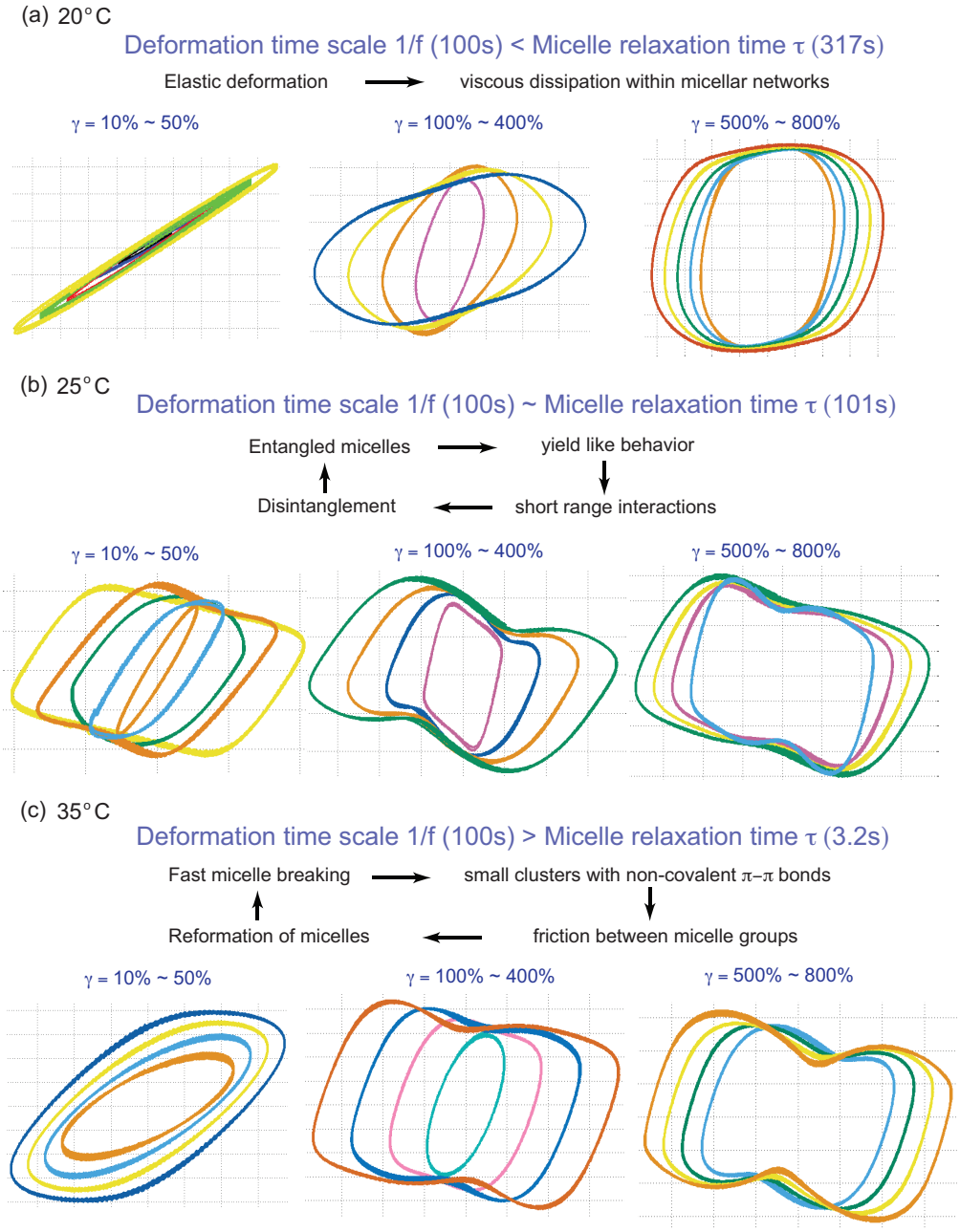

Figure 2.17: Plot of Lissajous curves (Torque versus angular displacement) under 20 °C (with a deformation time scale < micelle relaxation time λ_r), 25 °C (with a deformation time scale micelle relaxation time λ_r), 35 °C (with a deformation time scale > micelle relaxation time λ_r). Each Lissajous curve corresponds to different strain within in the range marked above.

mechanism[32,155,251,253]. In polydispersed wormlike micellar systems, a simple superposition of the Doi-Edwards model by Cates et al.[32] for different chain length was proved to be inadequate in describing the relaxation of micelle system. Therefore, other potential relaxation time scales from the length/concentration fluctuation of micelles might also be responsible for the stress response we observed earlier. Investigations of spatial resolution of heterogeneous bands, formation of shear induced structure phase[260,261] and localization of stresses at different deformations by rheo-optics[262–264] will be considered in future work to correlate shear stress and flow-birefringence, and flow instability in the CTAB/SHNC system. Concentration fluctuation and shear induced bond formation should be studied to further explore the transient behavior of highly viscoelastic hydrotropic micellar system.

Chapter 3

FLOW OF CTAB/SHNC MIXTURE AROUND CONFINED MICROFLUIDIC CYLINDERS

In this chapter, we utilized microfluidics as a tool to study how wormlike micelles behave at large deformations in the flow. Different from tradition rheometers, microfluidics was able to provide a large deformation of fluids without inertia effects present. Experiments with WLM solutions through model microfluidic porous media have revealed a variety of complex flow phenomena that can occur under such conditions, including the formation of stable gel-like structures known as a Flow-Induced Structured Phase (FISP). Such microstructural transitions undoubtedly play an important role in applications of WLM fluids, but are still poorly understood. An important first step in understanding flows of WLM fluids through porous media can be made by examining the flow around a single microscale cylinder aligned on the flow axis. This chapter describes the flow behavior of 60 mM CTAB/SHNC solutions around three confined microfluidic cylinder geometries. The strong hydrophobicity and naphthalene structure present in the SHNC induces significant growth of CTAB wormlike micelles, promotes stable micellar network formation and rich flow instabilities depending on the cylinder blockage ratios at different Weissenberg (Wi) numbers. Flow of WLM solutions around confined cylinders results in the onset of a sequence of low Re flow instabilities with increasing Wi. We mapped out the transition from symmetric Newtonian-like flow, unsteady asymmetric, vortex growth and unstable three dimensional flow behavior. The instability upstream of the cylinder is associated with high stresses in fluid that accelerates into the narrow gap between the cylinder and the channel wall, while the vortex growth is reminiscent of that seen in microfluidic contraction geometries. The instability downstream of the cylinder is associated with stresses generated at the trailing

stagnation point and the resulting flow modification in the wake.

3.1 Introduction

Viscoelastic flow around a cylinder has been considered as a benchmark problem in fluid mechanics and studied extensively by theoretical and numerical approaches[265–276]. Strong viscoelastic effects can be further enhanced as the characteristic length scale of the geometry is reduced to the microfluidic scale[63–65,277]. Small characteristic lengths l of fluidic devices result in short time scales T and high deformation rates $\dot{\gamma}$, which scale as $\sim U/l$, where U is a characteristic speed. Therefore in microfluidic devices elastic effects as characterized by the magnitudes of either the Weissenberg number $Wi = \lambda\dot{\gamma}$, or the Deborah number De can become high. In contrast, inertial effects in microfluidic devices, which can be characterized using a Reynolds number Re (which scales as $\sim l$) can become negligibly small. Several recent studies utilized microfluidic devices (with length scales of tens to hundreds of microns) to study elastic and inertio-elastic instabilities and three dimensional effects in viscoelastic fluids including polymer and wormlike micellar solutions[3,38–41,43–46,67–71,268,278–281].

Vasudevan et al.[70] studied a series of semi-dilute WLM solutions composed of mixtures of cetyltrimethyl ammonium bromide (CTAB) with NaSal flowing through a microfluidic tapered channel packed with glass beads ($20 \sim 100$ μm in diameter). The packed glass beads simulated porous media flow capable of achieving a total fluid strain of $\sim O(10^4)$ with a combination of shear and elongation deformation rates of $\sim O(10^4\ \mathrm{s}^{-1})$. They reported the formation of a long-lived gel-like structures emerging from the porous bed, which they named a flow-induced structured phase (FISP). Similar FISP formation has since been observed for the flow of WLM solutions through simpler two-dimensional (2D) microfluidic model porous arrays of cylinders[7,8,71] and with WLM solutions formed from non-ionic surfactant. It has been shown by high-resolution SEM imaging of captured gels that the FISP structure is stabilized by the formation of intermicellar branches and connections[8]. However, the exact cause of this microstructural transition and and the reason for it's irreversibility remains largely unknown. The formation of such gel-like FISP in porous media flows of WLM's

is likely to be of significant relevance to the application of WLM's in oilfield flooding and therefore demands to be better understood. Gel formation has also been reported for flow of aqueous poly(acrylamide) solutions through porous beds of sand or ballotini if extremely high deformation rates are applied and pore spaces are smaller than $\sim O(10\ \mu m)$[282].

A first step towards understanding flows through a packed bed of particles comes from looking at the flow around a single particle such as a sphere, or it's 2D equivalent, a cylinder. Flow around a cylinder has long been considered as a benchmark fluid mechanics problem[73–76,160–165]. The flow field around the cylinder can be separated into three distinct regions: the upstream region before flow reaches the cylinder, regions of high shear rates on either side of the cylinder and the extensional wake to the rear of the trailing stagnation point. Flow around cylinders and spheres have been studied as a good model for many industrial processes that are relevant to applications such as flow separation, flow though porous media, particle suspension or sedimentation, etc[114,159,283]. Previous experimental studies of wormlike micellar solutions flow around cylinders include flow past macroscopic cylinders[138–140]. In concentrated CTAB/NaSal solutions, Gladden and Belmonte[140] reported solid-like tearing and cracking of the fluid in the wake of the cylinder along with an unsteady leading crack ahead of the cylinder. Since wormlike micelles can break and recombine after scission, the fracture was observed to "self-heal" after a few hours. Moss *et al.*[138,139] studied the flow around a cylinder with two different wormlike micellar solutions (50 mM CTAB mixed with 50 mM NaSal and 100 mM cetylpyridinium chloride (CPyCl) mixed with 50 mM NaSal) and observed elastic instability of CTAB/NaSal solution for flow rates beyond which a critical De was exceeded. Here, the Deborah number is defined by $De = \lambda u/R$, where u is the average velocity of the fluid, and R is the radius of the cylinder. They illustrated that the flow remained symmetric for both fluids at low De. As the De was increased, shear thinning effects dominated and a pressure drop inside of the channel was observed. For further increases in De, extensional rheology began to play an important role resulting in the onset of elastic instability, in particular for the CTAB/NaSal solution, which showed strong strain hardening behavior under extensional flow.

In a microscale fluidic device, Kenney et al.[279] studied aqueous polyethylene oxide (PEO) solutions flowing around a cylinder. They used a single confined cylinder of diameter $D = 65$ μm in a channel of width $W = 100$ μm, providing a blockage ratio of $\beta = D/W = 0.65$. The Deborah number was varied between $0.01 < De < 1672$ and the Reynolds number between $0.1 < Re < 10$. Flow instability in the downstream wake was characterized by disordered and temporally varying streamlines, and was observed within the range $1 < De < 100$ and $0.1 < Re < 10$. This was a precursor to an instability upstream of the cylinder, which occurred for $Re > 10$ and $De > 10$, with unsteady vortices formed at the upstream surface of the cylinder. They concluded that the instability was fundamentally elastic in origin, though was affected by the moderate inertia in their experiment. Kenney et al.[279] discussed their results in terms of a well-known criterion that describes the onset of purely elastic flow instabilities in terms of a build up of elastic tensile stresses along curved streamlines[284]. However, in subsequent experiments using a wider variety of viscoelastic fluids and geometries with a range of characteristic dimensions, the same group of authors concluded that the onset of instability was due to the disruption of the base flow by the traveling elastic wave as the viscoelastic Mach number exceeded $Ma > 1$[285] With non-shear-thinning poly(acrylamide) in glycerol solutions, Galindo-Rosales et al.[286] found that besides the blockage ratio, the aspect ratio of the microchannel ($\alpha = H/W$, where H is the channel height) can also have a significant effect on the onset of instability. For given values of β and Wi, the instability was reported to become more intense for lower values of the aspect ratio, α[286].

Recently, Sun and Huang[287] used full-field time-resolved flow-induced birefringence (FIB) imaging to study the behavior of CTAB/NaSal and CPyCl/NaSal WLM solutions in straight microchannels containing cylinders on their central axes. Three flow cells were examined: two of the devices contained a single cylinder with relatively low blockage ratios $\beta = 0.25$ and $\beta = 0.5$, the third device consisted of a linear array of seven aligned cylinders with $\beta = 0.5$. Sun and Huang demonstrated that both extensional and shear strain rates contributed to the flow induced birefringence and the retardation measurement provides a quantitative

and non-invasive representation of the fluid deformation and stress in microfludics.

Motivated by this work, we examine the flow of a WLM solution through microchannels containing a single cylinder with varying cylinder to channel width ratio. We use a combination of quantitative full-field FIB imaging and micro particle image velocimetry (μPIV) to study the effect of the localized micelle deformation on the macroscopic flow field over a wide range of imposed Wi but for low fluid inertia. We also use fluorescent streak images to qualitatively compare the flow patterns observed between wormlike micellar solutions with those seen for the flow of Newtonian fluid. We observe a complex sequence of non-Newtonian flow effects and viscoelastic flow instabilities upstream and downstream of the cylinders as Wi is incremented.

3.2 Experiments and Methods

3.2.1 Material preparations

The wormlike micellar solution is an aqueous mixture of a cationic surfactant CTAB (Sigma-Adrich, Saint Louis, MO) and 3-hydroxy naphthalene-2-carboxylate (SHNC), a strong binding organic hydrotropic salt (TCI America, Portland, OR), used as received. The solution was prepared by adding [CTAB] = 60 mM and SHNC with the fixed molar ratio of R= [SHNC]/[CTAB] = 0.32 to deionized water and mixing for a minimum of 24 hours under room temperature 25 ^{o}C, and allowing the solution to equilibrate for one week. This salt/surfactant concentration ratio falls within the semi-dilute regime containing entangled wormlike micelles[288]. In particular, the strong hydrophobicity and naphthalene structure present in the SHNC enable strong non-covalent bonds (cation-π and π–π) between adjacent micelles, see schematics in Fig 2.1. As a result, micelles in this particular CTAB/SHNC system have shown persistent birefringence after the cessation of flow[10,182], with stronger viscoelasticity when compared to other cationic surfactant-salt systems[288].

To highlight the hydrodynamic and structural instability in wormlike micellar solutions, we also prepared a Newtonian fluid that consists of 92 wt% glycerol mixture with DI water,

with a constant viscosity of 0.15 Pa.s at 25 ^{o}C. We chose proper flow rates for the Newtonian solution in the microdevices to cover the same Re range as those for the wormlike micellar solutions. We then explored the flow instability originated from elasticity by comparing the flow patterns and velocity profiles between the Newtonian fluid and wormlike micellar solution.

3.2.2 Rheological characterizations

The viscoelastic properties of the wormlike micellar solution were measured by using a stress controlled rheometer (MCR 502, Anton-Paar), with a stainless steel cone and plate geometry (50 mm diameter and angle 1°, with a truncation gap of 59 μm). The measurable shear rate ranged from $\dot{\gamma} = 10$ s^{-1} up to $\dot{\gamma} = 300$ s^{-1} to avoid sample ejection from the rheometer, see solid symbols in Fig 3.1 (a) and its insert plot. All measurements were repeated 3 times and an environmental chamber was used to prevent sample evaporation.

Since the shear rate value reaches as high as $\sim O(10^3$ s$^{-1})$ in the microfluidic cylinder flow, the steady flow procedure was performed by using a high aspect ratio, rectangular microfluidic slit rheometer (m-VROC, RheoSense Inc.) to obtain the shear rheology information at high shear rate regime. The channel width, height and length are W = 50 μm, H = 3.308 mm and L = 8.8 mm respectively; four 800×800 μm^2 MEMS-based pressure transducers are fitted along the centerline[45]. A thermal jacket maintained the temperature of the sample and the microfluidic chip at 25 ^{o}C. The Weissenberg-Rabinowitsch-Mooney correction was applied in order to determine the true wall shear rate, enabling the computation of the shear-rate-dependent viscosity up to shear rates of $\dot{\gamma} = 3 \times 10^4$ s^{-1}. This allowed us to characterize the high shear rate branch for the shear banding solution of CTAB/SHNC, see hollow symbols in Fig 3.1(a) and its insert plot.

The wormlike micellar solution (60 mM CTAB/SHNC) exhibited strong shear-thinning behavior with a zero shear viscosity around 136 Pa.s, see Fig 3.1(a). The micellar solution reached a constant stress (around 4 Pa) at $\dot{\gamma} = 0.2$ s^{-1} and expanded in two decades in shear rates, which has been generally characterized as shear banding, see Fig 3.1(b). In the shear

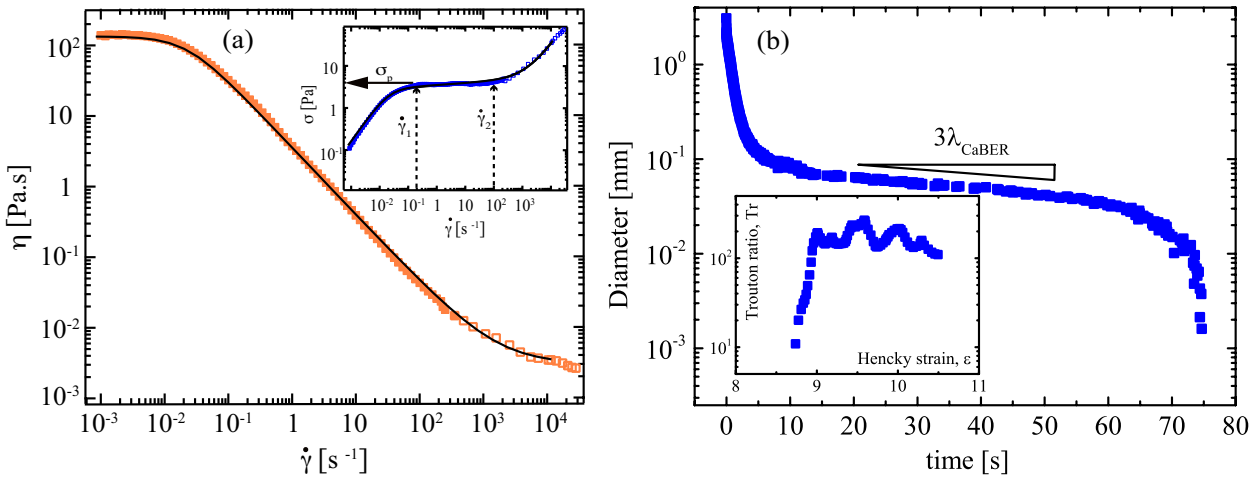

Figure 3.1: (a) Shear viscosity as a function of shear rates for 60 mM CTAB/SHNC solution under steady shear. At high shear rates, the solution exhibited shear thinning behavior. The inserted plot displays shear stress as a function of the shear rate. The shear banding region occurs at $\dot{\gamma} \in (0.2\ \mathrm{s}^{-1}, 100\ \mathrm{s}^{-1})$, with a nearly constant shear stress $\sigma_p = 4$ Pa. The data are well fitted by the Carreau-Yasuda model. (b) Dimensionless mid-filament diameter as a function of time for 60 mM CTAB/SHNC solution measured by CaBER, the insert plot showing the extensional viscosity as a function of total strain.

banding regime, homogeneous flow of wormlike micellar solutions can become unstable and separate into coexisting shear bands with different local viscosities and internal structures above a critical shear rate[30,77,78]. The $\eta(\dot{\gamma})$ and $\sigma(\dot{\gamma})$ were fitted by a Carreau-Yasuda model $\eta_{\dot{\gamma}} = \eta_\infty + (\eta_0 - \eta_\infty)/[1 + (\dot{\gamma}/\dot{\gamma}^*)^a]^{(1-n)/a}$, which yields the zero shear viscosity $\eta_0 = 130$ Pa.s, the infinite viscosity $\eta_\infty = 3$ mPa.s, characteristic shear rate for onset of shear thinning $\dot{\gamma}^* = 0.022\ \mathrm{s}^{-1}$, transient control factor $a = 1.5$ and power law index in the shear thinning region $n = 0.05$, see Table 3.1. The solution followed the single-mode Maxwell model at lower frequencies with the longest relaxation time at $\lambda_M = 45.5$ s, which was reasonably consistent with the cross over value obtained from the small amplitude oscillatory sweep, see Fig 2.2 in chapter 2.

The extensional properties of the wormlike micellar solution were characterized at 25 ^{o}C using a Capillary Breakup Extensional Rheometer (Haake CaBER1, Thermo Scientific),

Table 3.1: Rheological properties of solutions at 25 °C from Carreau-Yasuda model

Solution	η_0 (Pa.s)	η_∞ (Pa.s)	λ_{CaBER} (s)	$\dot{\gamma}^*$ (s^{-1})	n	a	Tr_{max}
60 mM	130 ± 1.3	0.003 ± 0.0001	45.4 ± 0.1	0.022	0.05	1.5	≈ 200

equipped with circular end-plates (d_0 = 6 mm in diameter) and a gap l_0 = 2 mm between the top and bottom plates for initial loading of the WLM fluid sample. The plates were separated by a linear displacement over a 50 ms time period to reach a final separation of l_f = 8 mm, and the time evolution of the diameter of the resulting fluid filament (d(t)) was measured until the eventual breakup of the fluid thread using a laser micrometer positioned at the midpoint between the two end-plates. The measurement was repeated six times in order to ensure reproducibility and a representative set of transient extensional rheology data is shown in Fig 3.1(b). As Fig 3.1(b) shows, the filament diameter decayed with time to an eventual breakup at time $t_c \approx 75$ s. The diameter versus time curve displays an extended elasto-capillary regime between times 15 s $\leq t \leq$ 60 s, where the diameter of the fluid thread decays exponentially with time[289,290]. This region can be fitted with an equation of the form $d/d_0 = \exp(-t/3\lambda)$ in order to extract a characteristic relaxation time for the fluid of λ_{CaBER} = 45.4 ± 0.5 s, which is in fair agreement with the relaxation times obtained from both the Carreau-Yasuda model fit to the steady flow curve and from the crossover observed in small amplitude oscillatory shear measurements[288].

The transient extension rate $\dot{\epsilon}(t)$ can be computed from the filament diameter using the expression $\dot{\epsilon} = -2\dot{d(t)}/d(t)$, which can be integrated over time to give the total accumulated Hencky strain $\epsilon = 2\ln[d_0/d(t)]$[289,290]. Within the elasto-capillary thinning regime, assuming a balance between surface tension and elastic forces, the transient elongational viscosity of the fluid can be computed according to $\eta_E = -\sigma/\dot{d(t)}$, where σ is the surface tension. The surface tension of the 60 mM CTAB/SHNC wormlike micellar solution was measured to be σ = 17.75 mN m^{-1} using a pendant drop tensiometer (Attension Theta, Biolin Scientific).

The transient dimensionless Trouton ratio of the fluid is given by $T_r = \eta_E/\eta_0$ and is plotted as a function of accumulated Hencky strain shown in the inset of Fig 3.1(b). The extensional viscosity η_E and Trouton ratio Tr increase monotonically with increasing Hencky strain ϵ_H, demonstrating a significant strain hardening: the WLM solution achieved a maximum extensional viscosity at a strain of $\epsilon = 9$ where the Trouton ratio reached a maximum value of $Tr_{max} \approx 200$.

3.2.3 Microchannel flow geometry design and fabrication

To investigate the elastic instabilities in the WLM solution under large shear and extension rates, we fabricate three microdevices with a single cylinder in the middle of a straight microchannel, with varying blockage ratios $\beta = \frac{D}{W}$, defined as the ratio of the cylinder diameter D over the channel width W. The channel width W and channel height H are the same for all devices. The blockage ratio in Device 1 was chosen as the bench mark value $\beta = 0.50$ based on literature[266], and increased to $\beta = 0.67$ in Device 2, and $\beta = 0.83$ in Device 3 to probe the spatial confinement effects on wormlike micelles at low fluid inertia, see Table 3.2 and Fig 3.2.

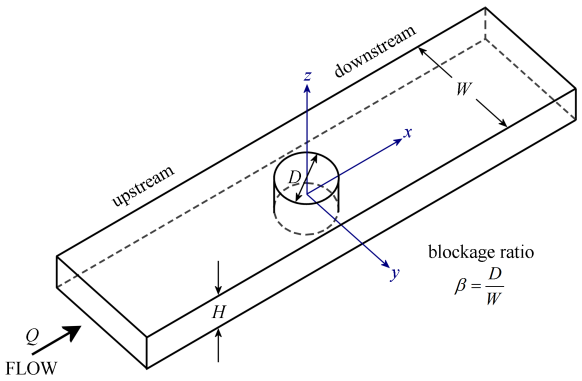

Figure 3.2: Microfluidic geometries contain a single cylinder in a straight microchannel with a blockage ratio (a) $\beta = 0.50$, (b) $\beta = 0.67$, and (c) $\beta = 0.83$, by fixing the width of the microchannel $W = 600$ μm and varying the diameter of the cylinder D accordingly (see details in Table 3.2).

The microfluidic devices were fabricated using Sylgard 184-PDMS elastomer via standard soft lithography techniques (SU-8 2050, MicroChem Corp. Newton, MA)[291]. After a layer of photoresist was spun onto a silicon wafer and cured, a Heidelberg μPG-101 machine (Heidelberg Instruments GmbH, Heidelberg, Germany) at 4X speed and 75% of 18 mW was applied to write the mold of microchannel onto the photoresist. The wafer was subsequently cured, developed, and surface treated to render it hydrophobic. A mixture 10:1 of polydimethylsiloxane (PDMS) (SYGARD 184, Dow Corning) was poured over the molds, and allowing curing overnight after degassing. The resulting PDMS cast was peeled from the wafer and plasma bonded onto a glass slide using a Femto plasma cleaner (Diener Electronic). A syringe pump neMESYS (Cetoni GmbH) equipped with a 10 mL Hamilton syringes was used to pump the wormlike micellar solution into the device through the inserted polyethylene tubing (Intragenic).

Table 3.2: Channel dimensions

Geometry	W (μm)	D (μm)	$\beta = \frac{D}{W}$	H (μm)
Device 1	600	300	0.50	100
Device 2	600	400	0.67	100
Device 3	600	500	0.83	100

3.2.4 Dimensionless groups

To study the effect of the localized micelle deformation on the macroscopic flow field in the microscale flow, we define the key dimensionless numbers the Re, the Wi and the elasticity number El based on conditions encountered within the narrow gap region between the cylinder and the channel walls:

$$\mathrm{Re} = \frac{\rho \bar{u} D_h}{\eta(\dot{\gamma})}, \tag{3.1}$$

and

$$\mathrm{Wi} = \lambda_{CaBER}\dot{\gamma} = \lambda_{CaBER}\frac{\bar{u}}{(1-\beta)W}. \tag{3.2}$$

Finally, the elasticity number El is:

$$El = \frac{Wi}{Re}. \tag{3.3}$$

Here the average flow velocity in the contraction region $\bar{u} = \bar{U}/(1-\beta)$, where $\bar{U} = Q/WH$ is the average flow rate in the main channel and Q is the imposed volume flow rate. The hydraulic diameter is $D_h = \frac{2(1-\beta)WH}{(1-\beta)W+2H}$ for a rectangular cross section channel. The shear viscosity $\eta(\dot{\gamma})$ is found by evaluating the Carreau-Yasuda fit to the steady flow curve at an average shear rate of $\dot{\gamma} = \frac{\bar{u}}{(1-\beta)W}$ in the narrow gap.

3.2.5 Flow visualizations

Flow induced birefringence (FIB)

Quantitative full-field flow-induced birefringence (FIB) imaging was performed using an Exicor Microimager (Hinds Instruments, Inc.). The Microimager is able to fully quantify both retardance and orientation angle during flow with a retardance resolution of 0.01 nm and a detection limit (noise floor) of 0.1 nm. The instrument performs Mueller matrix calculations on images acquired using two photoelastic modulators and a synchronized stroboscopic light source[292,293]. The calculation of retardance and orientation angle requires a total of 7 images, which are accumulated over a period of 1 s each, so while the system is fully quantitative in the case of steady flows, it does not have sufficient temporal resolution for capturing time-varying flows in detail. Nevertheless, even for unsteady flows we are able to obtain images that provide a good overall indication of the time-averaged spatial distribution of the micellar orientation and the optical retardance (hence stress distribution[151]) in the flowing

WLM solution. A 5X objective lens and a green light source with a wavelength of 532 nm were used in this work.

Streak imaging

Flow pattern visualizations were performed by capturing streak images with an inverted epi-fluorescence spinning-disc confocal microscope (DSD2, Andor Technology Ltd.), equipped with an Andor iXon camera and a Nikon 4X (NA = 0.13) objective lens. Both fluids (Newtonian fluid and WLM solution) were seeded at a concentration of 0.01 wt% with fluorescent polystyrene particles of diameter $d_p = 5$ μm (Microparticles, GmbH) with excitation and emission wavelengths of 530 nm and 607 nm, respectively. The illumination and visualization of the fluorescent particles was enabled by a mercury lamp and using the appropriate excitation and emission filters.

Streak images were recorded with frame rates ranging from 0.3 to 10 frames per second (fps) for the steady two dimensional flow, depending on the flow rate. For unsteady flows, single streak images were not sufficient to describe the flow behavior. Thus we recorded streak imaging videos over time periods of several seconds in order to characterize the time dependent nature of flow field in such cases.

Micro-particle image velocimetry (μ-PIV)

The kinematics associated with the flow was visualized by micro-particle image velocimetry, μ-PIV (TSI Instruments). Monodispersed fluorescent polystyrene microspheres of diameter $d_p = 1$ μm (Life Technology) were added to the solution at a concentration of 0.025 wt%, with excitation and emission wavelengths of 535 nm and 575 nm, respectively.

The laser light was emitted from a double pulsed 532 nm Nd: YAG laser. A temporal sequence of particle images was created by illuminating the same plane using multiple laser pulses with a variable delay; the timing control was implemented using a LaserPulser Synchronizer. The delay between laser pulses was chosen within the range of 80 μs $< \delta t <$ 800 μs according to the flow rates and region of interest (ROI).

The particle images were acquired through a 4X (NA = 0.1) objective lens, for which the correlation depth is around 55 μm. The majority of the images were captured at the center plane of the channel, which was identified by focusing on the top and bottom stationary particles first and then averaging the distance. The sequence of images was recorded with a high frame rate CMOS camera and processed by a conventional cross-correlation PIV algorithm[294,295]. For steady state flow, 100 image pairs were ensemble-averaged to obtain a single velocity field. For unstable flows, a pair of images were analyzed within 100 total images to study the time-dependent behavior. Post-processing techniques to remove spurious vectors and interpolate for missing vectors were only used for unsteady flows.

3.3 Results

In this section we investigate the effects of localized micelle deformation and increasing spatial confinement in the microchannel upon the macroscopic flow field of the wormlike micellar solution over a wide range of Wi but for low Re. By using a combination of quantitative full-field FIB imaging, μ-PIV, and fluorescent streak imaging, we are able to qualitatively and quantitatively compare the flow patterns from the WLM solution with those from the Newtonian fluid over a similar Re range.

3.3.1 Newtonian flow around confined microfluidic cylinders

We first examined the Newtonian flow around confined microfluidic cylinders, in order to validate our measurement techniques and to provide standard flow patterns for later comparison with flows of the wormlike micellar solution. Streak images of Newtonian fluid flow around three confined geometries are shown in Fig.3.3, for a range of Reynolds numbers spanning $1.4 \times 10^{-3} < Re < 23$. Fore-aft symmetry with smooth streamlines around the cylinder were observed in all three devices over the entire range of Re (see Fig.3.3).

We also conducted μ-PIV experiments in order to quantitatively map the flow field of the Newtonian fluid in all three channels as a function of increasing flow rates, or Re, see Fig 3.4 (a_2). Here, the two-dimensional (2D) maps of the velocity magnitude shown with

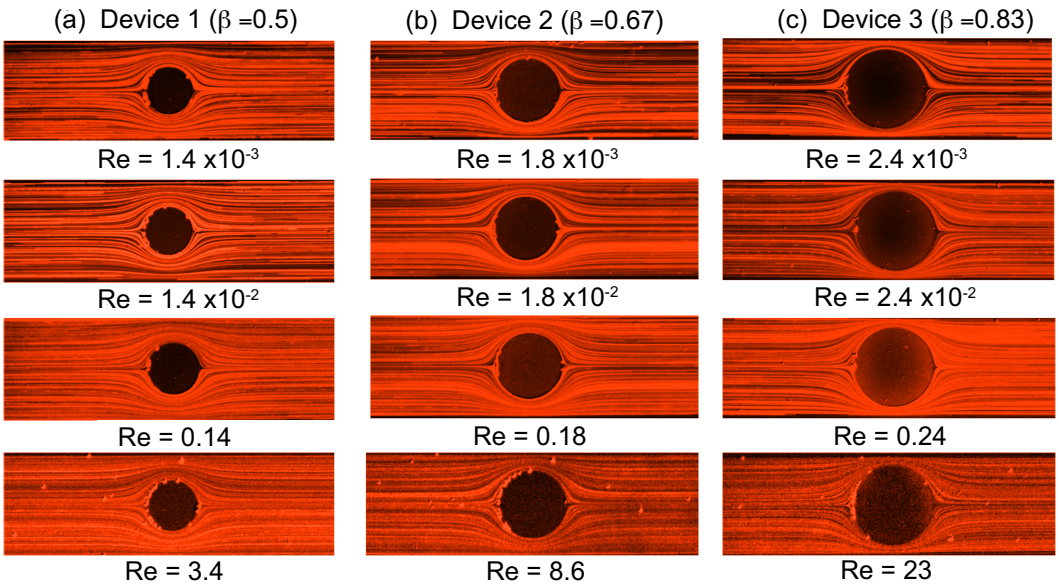

Figure 3.3: The development of streakline patterns in the flow of glycerol solution in (a) Device 1 with $\beta = 0.50$; (b) Device 2 with $\beta = 0.67$; and (c) Device 3 with $\beta = 0.83$. Flow stayed fore-aft symmetric over the range of $1.4 \times 10^{-3} < Re < 23$ in all three devices.

superimposed streamlines (top panel, Fig 3.4 (a_1), (b_1) and (c_1)) have been normalized using the average velocity in the constriction regions, $\bar{u} = \bar{U}/(1-\beta)$. The streamwise velocity profiles of v_x along the centerline (y = 0, middle panel, Fig 3.4 (a_2), (b_2) and (c_2)) and across the channels at $x = 0.7$ mm (bottom panel, Fig 3.4 (a_3), (b_3) and (c_3)) for all three devices have been normalized by the average flow velocity in the main channel, $\bar{U} = Q/WD$. Curves with different colors in the middle and bottom panels correspond to different flow rates (hence Re numbers). These normalized velocity profiles nearly collapse into a single master curve, as expected for low Re flow of a Newtonian fluid. The black curves shown in Fig 3.4 (a_2), (b_2) and (c_2) are based on the theoretical prediction of the velocity profile for potential flow around a cylinder, with $v(x) = 1.68\bar{U}(1 - D/2x)$. Downstream of the cylinder at a distance of $x = 0.7$ mm, profiles of the streamwise flow velocity taken across the channel compare well with a numerical prediction of the fully-developed velocity profile for creeping Newtonian flow in a 600×100 μm^2 rectangular channel, see black lines in Fig 3.4

(a_3), (b_3) and (c_3). This prediction gives the maximum streamwise velocity along the channel axis of $v_{x.max} = 1.68\bar{U}$. The close agreement between our experimental velocimetry data and theoretical expectations validates our PIV setup and image processing algorithms and allays any concerns regarding excessive averaging due to the large measurement depth of our imaging system[134,272,274].

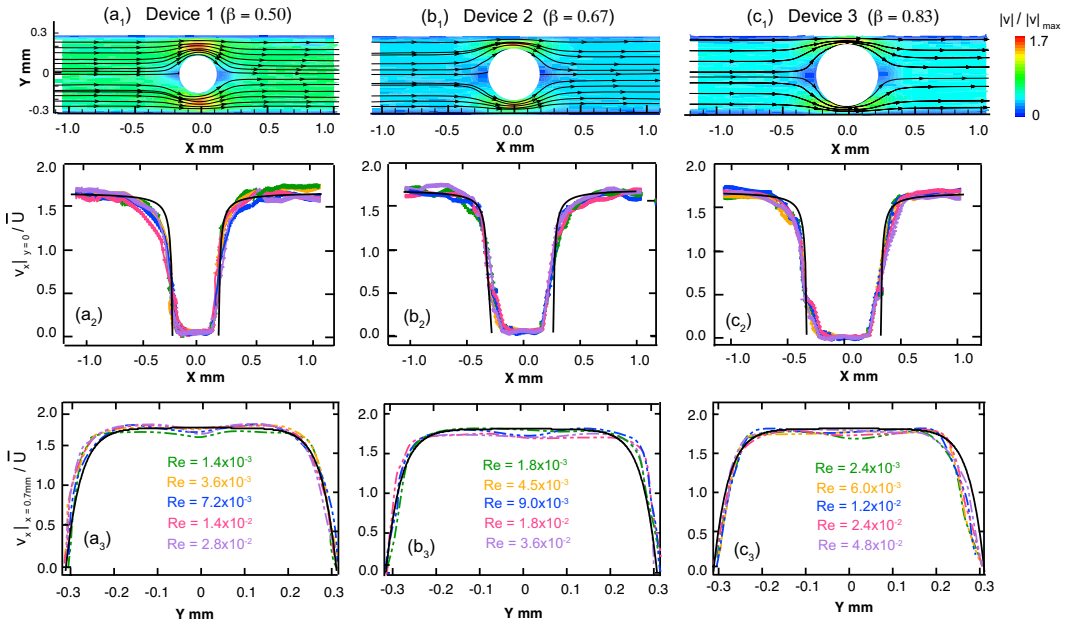

Figure 3.4: Velocity vector map constructed from μ-PIV for the Newtonian fluid around (a_1) Device 1 ($\beta = 0.50$), (b_1) Device 2, and (c_1) Device 3 ($\beta = 0.83$) over the range of 0.1 mL/h $< Q <$2 mL/h, corresponding to 1.4 $\times 10^{-3} < Re <$ 4.8 $\times 10^{-2}$. In the middle panel, (a_2), (b_2) and (c_2) plotted horizontal velocity at the center line $y = 0$. The black curves are based on the theoretical prediction of the velocity profile for an inviscid flow around a cylinder, with $v(x) = 1.68\bar{U}(1 - D/2x)$. ($a_3$), ($b_3$) and ($c_3$) plotted the normalized horizontal velocity along y axis at $x = 0.7$ mm. The black curves correspond to numerically-computed fully developed velocity profiles at the mid-height of a rectangular microchannel of dimension 600$\times$100 μm^2, which gives a maximum flow velocity on the channel centerline of $v_{x.max} = 1.68\bar{U}$.

3.3.2 Wormlike micellar flow around confined microfluidic cylinders

Here we present the results of streak imaging experiments and FIB measurements for the flow of the wormlike micellar CTAB/SHNC solution through the three confined microfluidic cylinder geometries in order to illustrate the transition from steady through to time-dependent flows at volumetric flow rates spanning $0.1 < Q < 10$ mL/h, which correspond to a wide range of Wi at $1 < Wi < 10^5$, but extremely low to moderate Re ($Re \in (10^{-7}, 10)$).

In Fig. 3.5 we present the results obtained from Device 1 (b = 0:5). We observed that the flow remained steady, symmetric and Newtonian-like for $Wi < 50$ (Q < 0.05 mL/h, data not shown). However, as the flow rate is increased, the flow patterns observed with CTAB/SHNC solution diverge in comparison to those of the Newtonian flow. For $Q = 0.1$ mL/h ($Wi = 1.4 \times 10^2$), bending streamlines are observed upstream of the cylinder, see Fig. 6a. As the Wi is increased to $Wi = 3.5 \times 10^2$ ($Q = 0.25$ mL/h) a recirculating vortex region develops at the upstream surface of the cylinder, which extends progressively further upstream with increasing flow rates. Interestingly, with this WLM solution we do not observe the "pinching" of streamlines immediately upstream of the recirculation region, which seems to be a typical feature of flows of viscoelastic polymer solutions around cylinders[134,135]. Here we observe more smooth and continuous divergence of the streamlines towards the sides of the cylinder. For $Q \geq 1$ mL/h ($Wi \geq 1.4 \times 10^3$), bending streamlines and lateral asymmetries about the $y = 0$ axis become apparent towards the downstream wake of the cylinder. Crossing streamlines also indicate the onset of three-dimensional (3D) flow effects. When the flow rate reaches Q =10 mL/h ($Wi = 1.4 \times 10^4$), the flow upstream of the cylinder undergoes a large scale loss of stability, the recirculating vortex region collapses and reforms in an apparently quasi-periodic fashion, leading to an unsteady 3D flow field.

The streak images in Fig. 3.5 (a)(left column) are consistent with the birefringent patterns shown in the middle and right columns in Fig. 3.5 (b)(c). As in the streak images, we observe distinctly different growth of the birefringence patterns upstream and downstream of the cylinder. In the upstream region, the birefringence intensity increases the most where

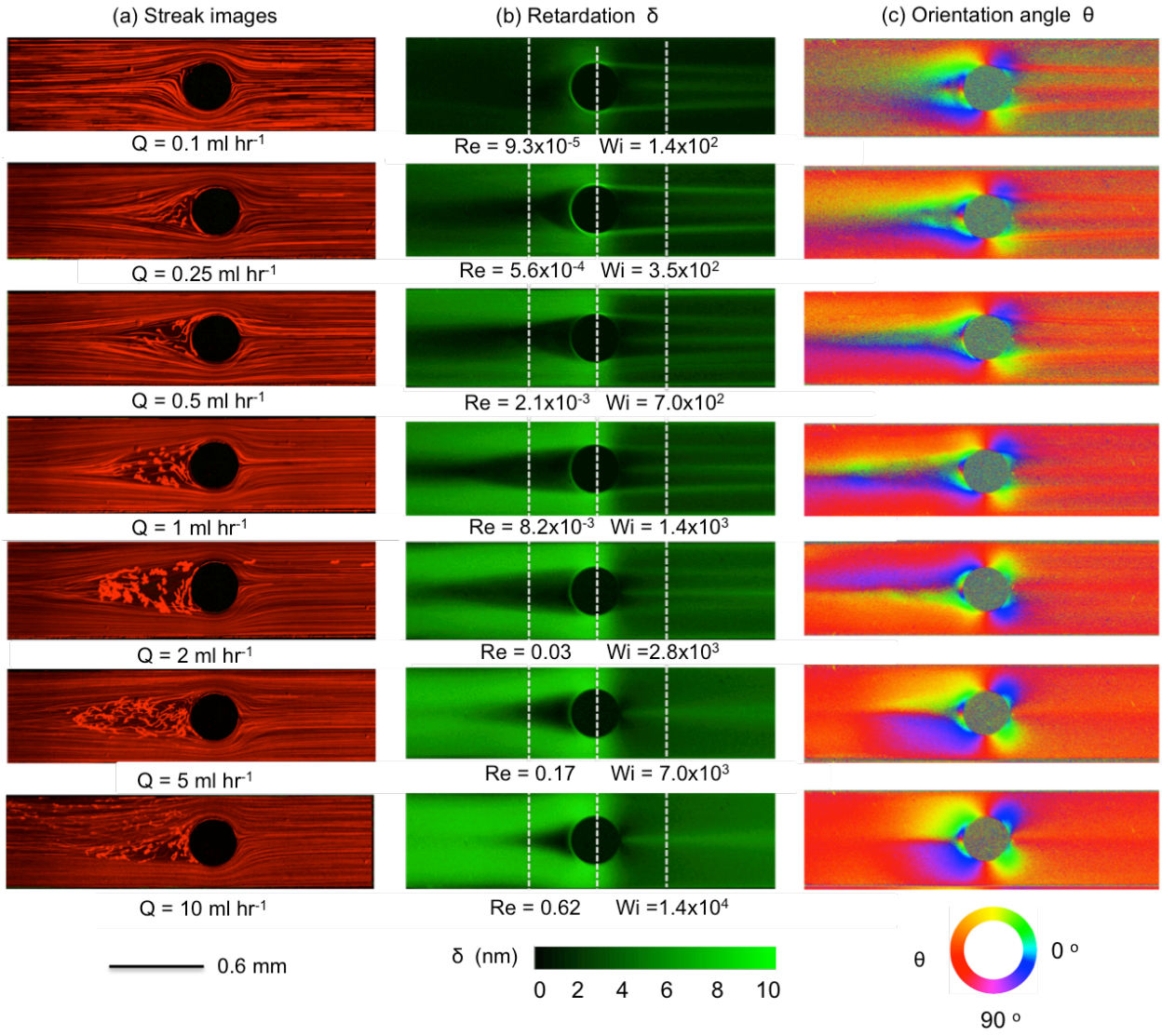

Figure 3.5: The development of flow patterns in the flow of 60 mM CTAB/SHNC solution in Device 1 ($\beta = 0.50$) (flow from left to right) with (a) streak images; (b) birefringence retardation; and (c) extinction angles at flow rates 0.1 mL/h $< Q <$ 10 mL/h, corresponding to 9.3 $\times 10^{-5} < Re <$ 0.62, and 1.4 $\times 10^{2} < Wi <$ 1.4 $\times 10^{4}$.

fluid is squeezed into the narrow gaps between the sides of the cylinder and the channel walls. The result is reminiscent of the flow into a contraction, in which the stress increases progressively as polymers or WLMs approach the contraction and recirculating regions develop and grow at the corners, effectively displacing the contraction plane towards the upstream as the Wi is increased[134,135]. Here, the upstream surface of the cylinder behaves as the salient corner located between two "half-contractions". As Wi increases, the growth of the upstream recirculation causes the streamlines to divide, and stress to grow, from a location progressively further back upstream. The patterns of retardation upstream of the cylinder shown in Fig. 3.5 (b) bear similarity to those reported by Sun and Huang[287] for flows of wormlike micellar CTAB/NaSal solutions around confined microfluidic cylinders with $\beta = 0.5$. However, they are quite distinct from the images of birefringence captured by Moss and Rothstein[138,139] for the flow of CTAB/NaSal solutions upstream of macroscopic cylinders with relatively less blockage ratios $\beta = 0.1$ and 0.2. They reported that micelles deformed strongly upstream of the cylinder and that the retardation intensity increased approaching the edge of the cylinder; in contrast, our birefringent patterns show a dark area with lower birefringence intensity in the area upstream of the cylinder corresponding to the location of the recirculation seen in Fig. 3.5 (a). This discrepancy between our observations and those of Moss and Rothstein[138,139] is probably due to increased confinement effects between the microchannel wall and the sides of the cylinder, which gives rise to extra viscoelastic stresses, resulting in pressure buildup and secondary flows upstream.

Downstream of the cylinder, the buildup of stress birefringence due to the contraction in flow cross section at the sides of the cylinder is suddenly relieved as the flow expands into the downstream wake, Fig. 3.5 (b). Here, we observe the formation and intensification of narrow birefringent strands that originate from the trailing edge of the cylinder. Initially, at $Wi = 1.4 \times 10^2$, three such strands are clearly evident: two strands are located symmetrically on either side of the $y = 0$ axis and appear to originate from shear-induced birefringence that becomes detached from the surface of the cylinder. The third birefringent strand is centrally located and originates from the axial trailing stagnation point. At such

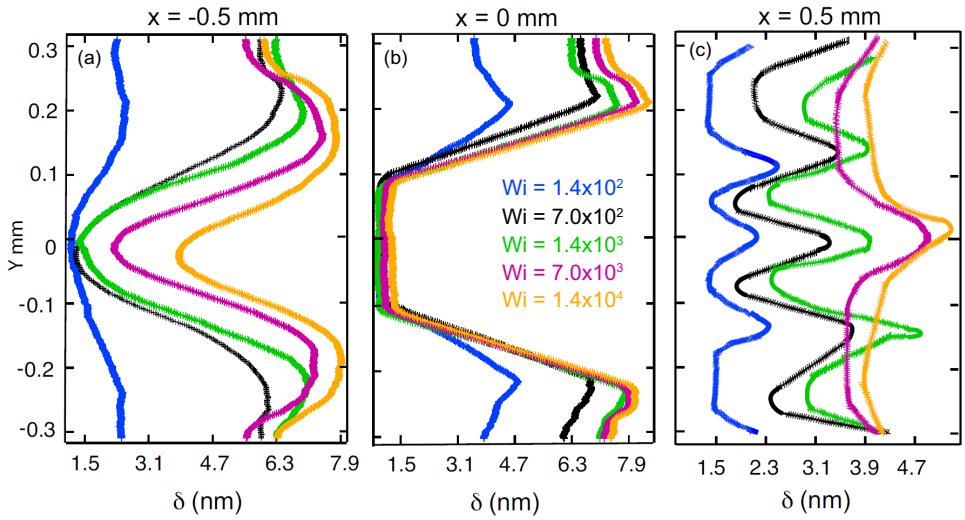

Figure 3.6: Retardation δ in Device 1 ($\beta = 0.50$), plotted along the transverse direction y at position of (a) $x = -0.5$ mm (i.e. upstream of the cylinder); (b) $x = 0$ mm (across the cylinder axis); and (c) $x = 0.5$ mm (downstream of the cylinder), respectively. In each sub-figure, curves with different colors correspond to flow rates varied from 0.1 mL/h $< Q <$ 10 mL/h, equivalent to 1.4 $\times 10^2 < Wi <$ 1.4 $\times 10^4$.

locations residence times are long and elongational rates can be high, while shear and vorticity is minimal. These conditions provide the possibility of achieving high elongation of WLMs. As the Wi increases beyond $Wi = 7.0 \times 10^2$, the relative intensity of the central birefringent strand grows as the two off-axis strands diminish. Eventually, for $Wi = 7.0 \times 10^3$, only the single centrally located strand originating from the stagnation point remains. The formation of birefringent strands in the strong extensional flow of WLM solutions in the vicinity of stagnation points has been reported in a number of publications. Similar patterns of birefringent strands were observed previously by Moss and Rothstein[138,139] for the flow of CTAB/NaSal solutions downstream of macroscopic cylinders with low blockage ratios. The pattern of three birefringent strands seen here is also similar to that reported by Cressely and Hocquart[265] for the flow of a poly(ethylene oxide) solution in the wake of a cylinder and is reminiscent of the birefringence patterns reported by Haward and Odell[296] for the flow of dilute poly(styrene) solutions in the wake of a sphere.

We quantitatively characterize the birefringence growth with Wi in Device 1 by plotting the retardation d measured across the microchannel at three specific locations: at the upstream position x = - 0.5 mm (Fig. 3.6 (a)); at the centerline of the cylinder $x = 0$ (Fig. 3.6 (b)); and at the downstream position $x = 0.5$ mm (Fig. 3.6 (c)), as indicated by the locations of the three vertical dashed white lines shown in Fig. 3.5 (b). For each x position, the birefringence intensity measured transverse to the flow direction changes significantly as the flow rate is increased in the range 0.1 mL/h $< Q <$ 10 mL/h , equivalent to 1.4 $\times 10^2 < Wi <$ 1.4 $\times 10^4$.

When the Wi increases from $Wi = 1.4 \times 10^2$ (blue curves) to $Wi = 7.0 \times 10^2$ (black curves), the retardance near the channel walls upstream of and to the sides of the cylinder increases significantly, before tending towards a saturation value of around 8 nm as Wi is increased towards $Wi = 1.4 \times 10^4$, see Fig. 3.6 (a), (b). For downstream flows at $Wi \leq 1.4 \times 10^3$, three birefringent strands are evident at $x = 0.5$ mm, which exhibit intensity peaks at y = -0.15 mm, $y = 0$ mm and $y = 0.15$, see Fig. 3.6 (c). For higher $Wi \geq 7.0 \times 10^3$, the pair of strands located at $y = \pm$ 0.15 mm are lost, while the central strand continues to intensify with increasing Wi.

As the blockage ratio of the cylinder is increased in Device 2 (with $\beta = 0.67$), the onset of disordered streak images emerges at lower flow rates ($Q = 0.1$ mL/h and $Wi = 3.2 \times 10^2$) than in Device 1, with a larger unstable triangle-like vortex growth region formed upstream as the Wi is increased, see Fig. 3.7. As Wi is increased further, the divergent streamlines become progressively more pronounced and a transition to elastic instability occurs upstream when the flow rate reaches $Q = 5$ mL/h ($Wi = 1.6 \times 10^4$). Both the streak images and the birefringence patterns are very similar to those produced by Device 1, although the transitions between flow states are shifted to lower flow rates (but broadly similar Wi). For $Q = 2$ mL/h ($Wi = 6.3 \times 10^3$), we observe time-dependent quasi-periodic oscillations in the upstream flow patterns. This upstream instability intensifies with increasing flow rates ultimately resulting in a chaotic-appearing 3D flow field for $Q = 10$ mL/h ($Wi = 3.2 \times 10^4$.

With the largest blockage ratio of $\beta = 0.83$ (Device 3, Fig. 3.8), the flow streamline and

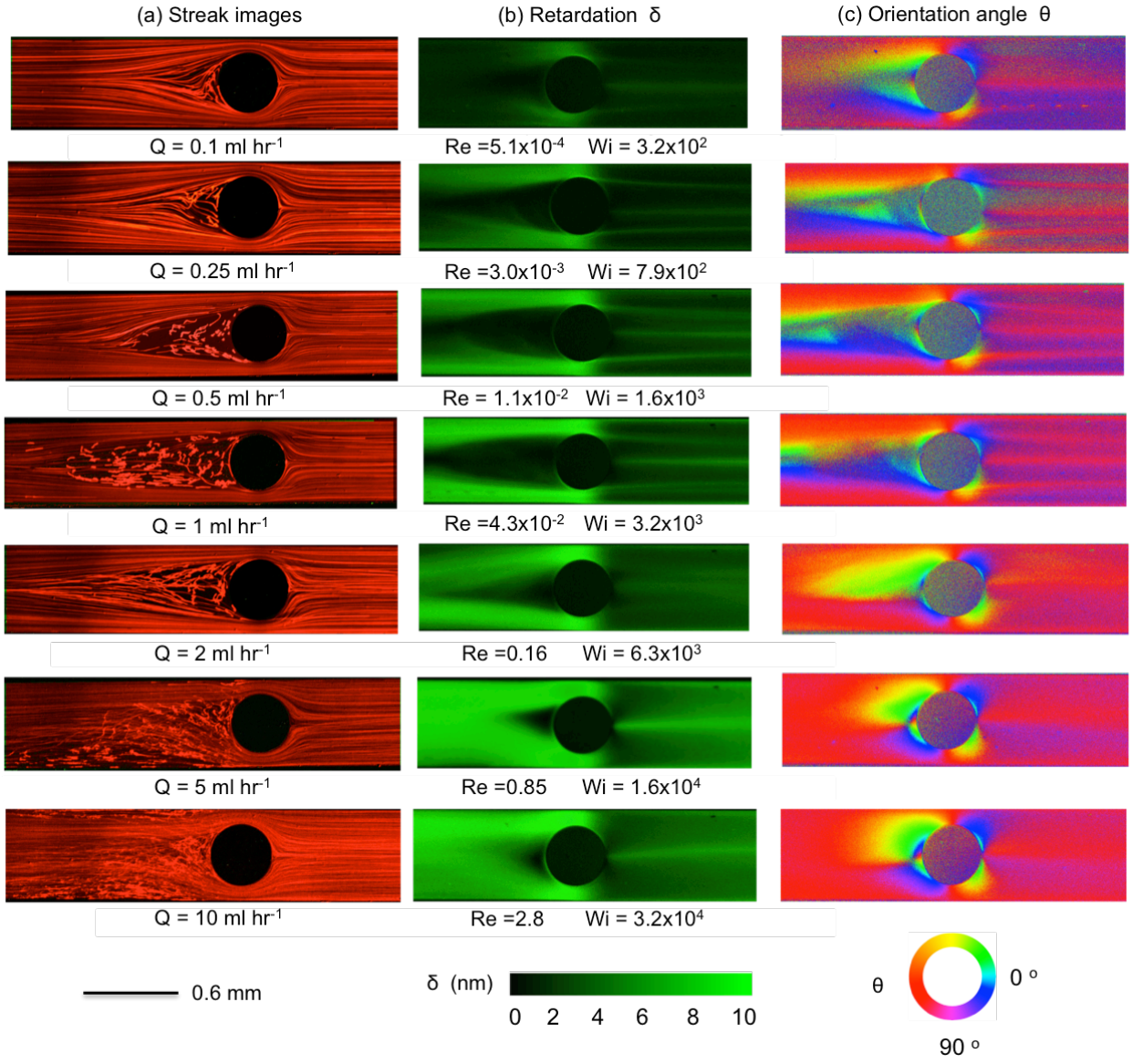

Figure 3.7: The development of flow patterns in the flow of 60 mM CTAB/SHNC solution in Device 2 ($\beta = 0.67$) (flow from left to right) with (a) streak images; (b) birefringence retardation; and (c) extinction angles at flow rates 0.1 mL/h $< Q <$ 10 mL/h, corresponding to 5.1 $\times 10^{-4} < Re <$ 2.8, and 3.2 $\times 10^{2} < Wi <$ 3.2 $\times 10^{4}$.

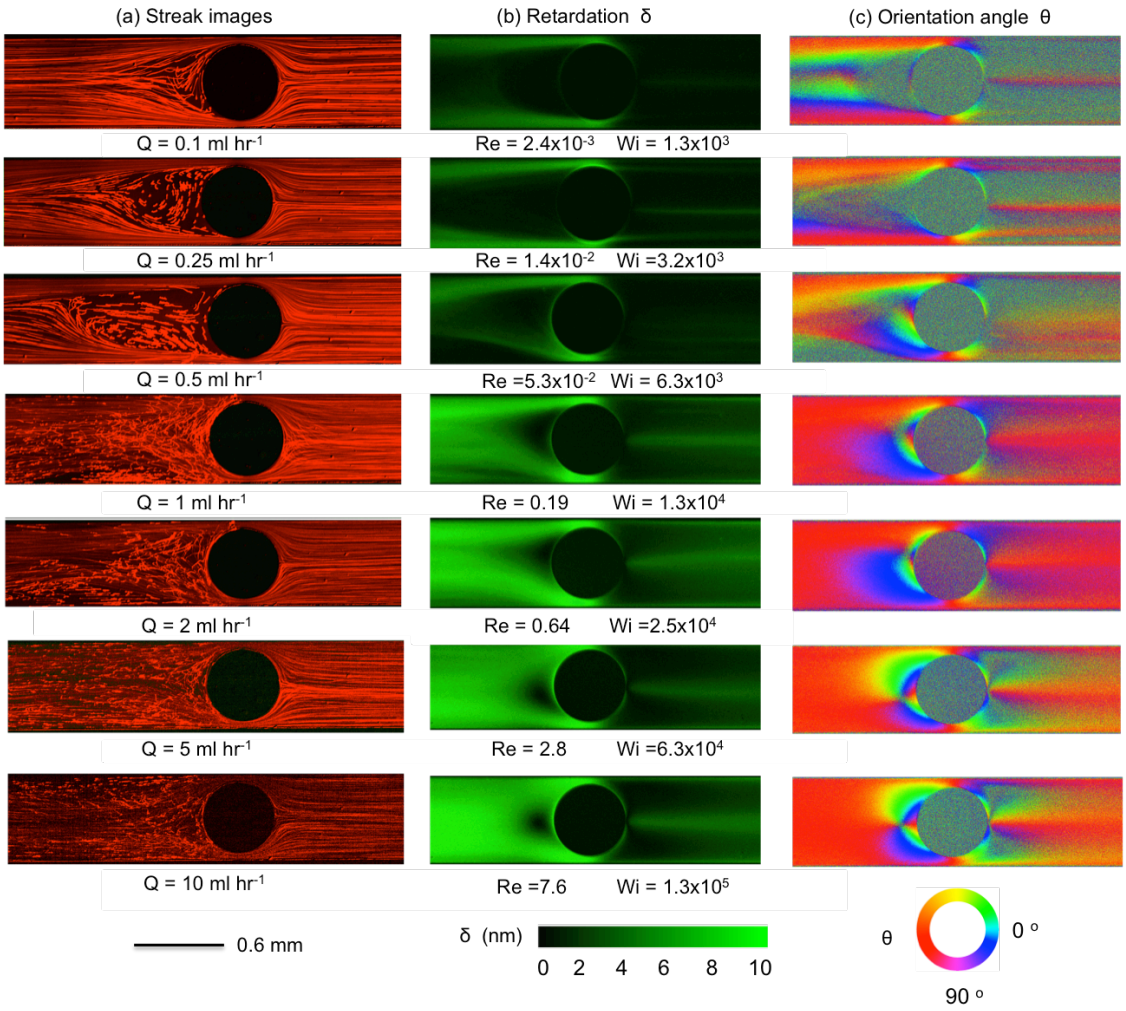

Figure 3.8: The development of flow patterns in the flow of 60 mM CTAB/SHNC solution in Device 3 ($\beta = 0.83$) (flow from left to right) with (a) streak images; (b) birefringence retardation; and (c) extinction angles at flow rates 0.1 mL/h $< Q <$ 10 mL/h, corresponding to 2.4 $\times 10^{-3} < Re <$ 7.6, and 1.3 $\times 10^{3} < Wi <$ 1.3 $\times 10^{5}$.

birefringence patterns are again broadly similar to those observed at lower blockage ratios (Fig. 3.5 and Fig. 3.7), although transitions between flow regimes are again shifted to lower flow rates. Significant spatiotemporal fluctuations and 3D flow is now clearly evident at a flow rate of only $Q = 1$ mL/h and $Wi = 1.3 \times 10^4$. For $Q \geq 2$ mL/h ($Wi \geq 2.5 \times 10^4$) flow upstream of the cylinder in Device 3 appears chaotic, while disordered and temporally varying streamlines become evident downstream of the cylinder. We note that the sequence of instabilities we observe here contrasts with reports involving viscoelastic polymer solutions, in which instability first arose downstream of the cylinder and was considered to drive the onset of instability in the upstream region. In the case of our WLM solution, instability in the form of bending and distorted streamlines is first apparent upstream of the cylinder.

We make use of quantitative μ-PIV measurements for the Newtonian fluid and the WLM test solution, in order to analyze and compare the flow velocity profiles downstream of the cylinder. Here we focus on Device 1 and Device 2 only because Device 3 exhibits unsteadiness in the downstream section of channel at rather low flow rates, so very limited data is available for analysis in this case.

In Fig. 3.9 (a) we present velocity magnitude maps with superimposed streamlines for the flow of the wormlike micellar CTAB/SHNC solution over a range of flow rates and Wi. At $Wi = 1.4 \times 10^2$ the flow is approximately fore-aft and laterally symmetric. However, at $Wi = 7.0 \times 10^2$ there appears a large almost stagnant region upstream of the cylinder in the area corresponding to the recirculation zone apparent in Fig. 3.5 (a). In the trailing wake of the cylinder a region of low flow velocity becomes apparent along the $y = 0$ axis, extending downstream from the trailing stagnation point and corresponding to the location of the central downstream birefringent strand observed in Fig. 3.5 (b). As the Wi is increased further, the stagnant region upstream of the cylinder grows upstream (as does the recirculating region shown in Fig. 3.5 (a)), while the low flow velocity region on the $y = 0$ axis downstream of the cylinder is maintained. Downstream of the cylinder, we make measurements of the streamwise velocity along the $y = 0$ axis (Fig 3.9 (b)) as well as across the channel at a location $x = 0.7$ mm (Fig 3.9 (c)). These velocity profiles have been nor-

malized by the average flow velocity in the channel, $\bar{U} = Q/WH$ and are compared with equivalent profiles obtained with the Newtonian fluid. In Fig 3.9 (b), it is clear that as the Wi is increased from 1.4×10^2 to 7.0×10^2 in Device 1 the flow velocity along the centerline of the channel downstream of the cylinder becomes very significantly reduced compared to the velocity measured in the Newtonian fluid. As Wi is increased further to 1.4×10^3 and subsequently to 2.8×10^3 , the centerline velocity increases again slightly. In Fig 3.9 (c), the profiles of the streamwise velocity taken across the channel in the downstream reveal the development of a significant dip in the velocity on the centerline, that appears as the Wi is incremented, resulting in a non-monotonic velocity profile. The location of the dip in the streamwise flow velocity corresponds to the location of the central birefringent strand observed in Fig. 3.5 (b) and (c). Such non-monotonic flow profiles have been observed in the vicinity of birefringent strands in polymer solution flows near stagnation points and are generally considered to be a consequence of a localized increase in the extensional viscosity of the fluid due to the high strains and elongation rates experienced at the stagnation point. We are not aware of any explicit report of such non-monotonic flow profiles obtained from flow velocimetry performed on wormlike micellar solutions flowing near stagnation points. It is interesting to point out that the two additional birefringent strands visible in Fig. 3.5 (b) and (c), located at $y \approx \pm 0.15$ mm, do not cause a dip in the velocity profiles shown in Fig 3.9 (c). This is despite the fact that the intensity of the retardance (hence presumably the stress) in those strands is at least equal to, or even greater than, the retardance measured in the central strand originating from the stagnation point. This is very like due to the stress gradient, which is largest for the strand in the center, governed the flow and led to the "negative wake" effect,

Similar trends are observed for the 60 mM CTAB/SHNC WLM solution flowing in Device 2 ($\beta = 0.67$), see Fig. 3.10. Here, very significant and sharp dips are apparent in the velocity profiles taken across the channel downstream of the cylinder, Fig. 3.10 (b,c), where the minimum normalized flow velocity can be as little as 30 % of the value measured in the Newtonian fluid. In the case of Device 2, the location of the local minimum in streamwise

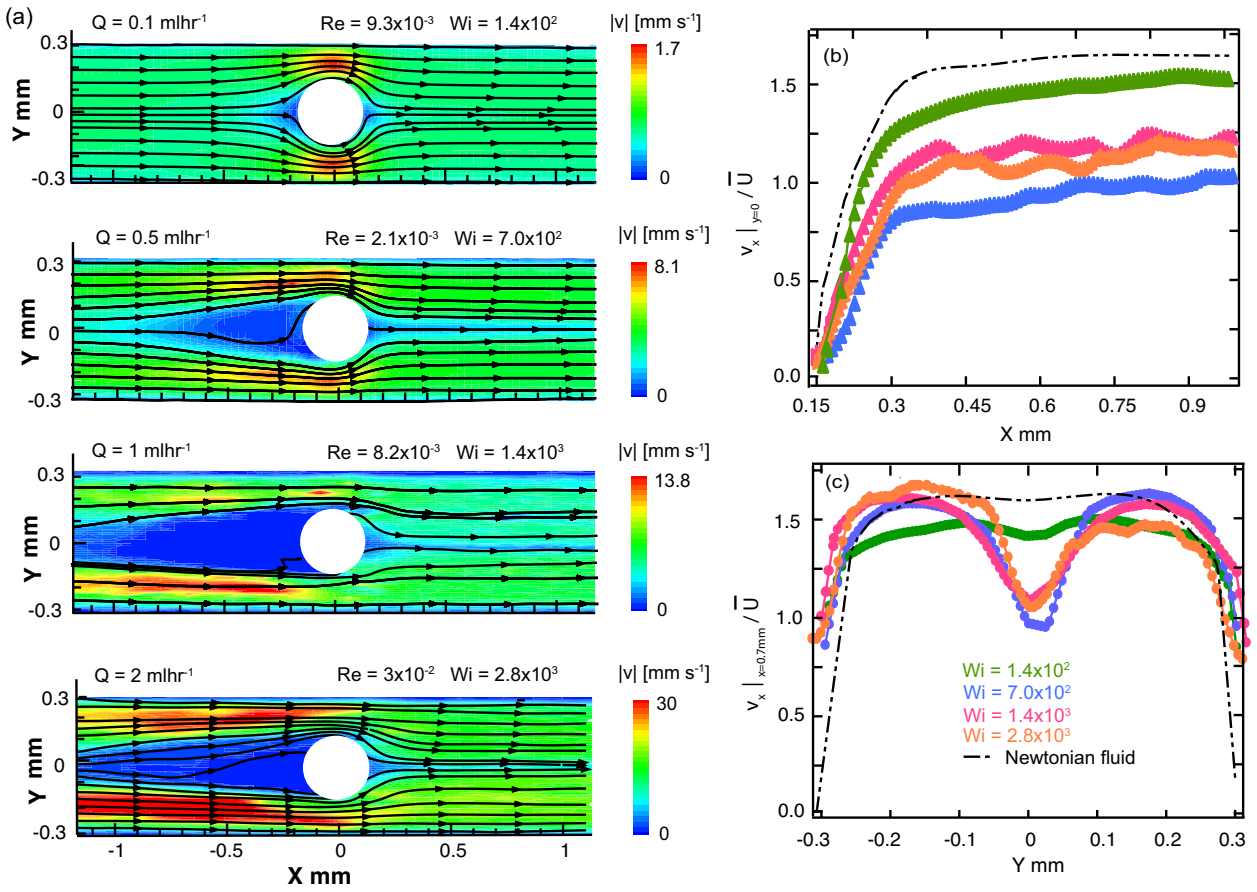

Figure 3.9: (a) Velocity magnitude maps with superimposed streamlines constructed by using μPIV at flow rates 0.1 mL/h $< Q <$ 2 mL/h for the flow of the WLM solution in Device 1 ($\beta = 0.50$). Different colors correspond to different velocity magnitudes, with color bars shown on the right. (b) Normalized streamwise velocity profiles along the channel center line $y = 0$ mm, downstream of the cylinder. (c) Normalized streamwise velocity profiles across the channel at $x = 0.7$ mm. The velocities are normalized by the average velocity $\bar{U} = \frac{Q}{WH}$ in the channel. Black dashed lines correspond to the normalized Newtonian fluid velocity profiles that are approximately independent of the flow rate.

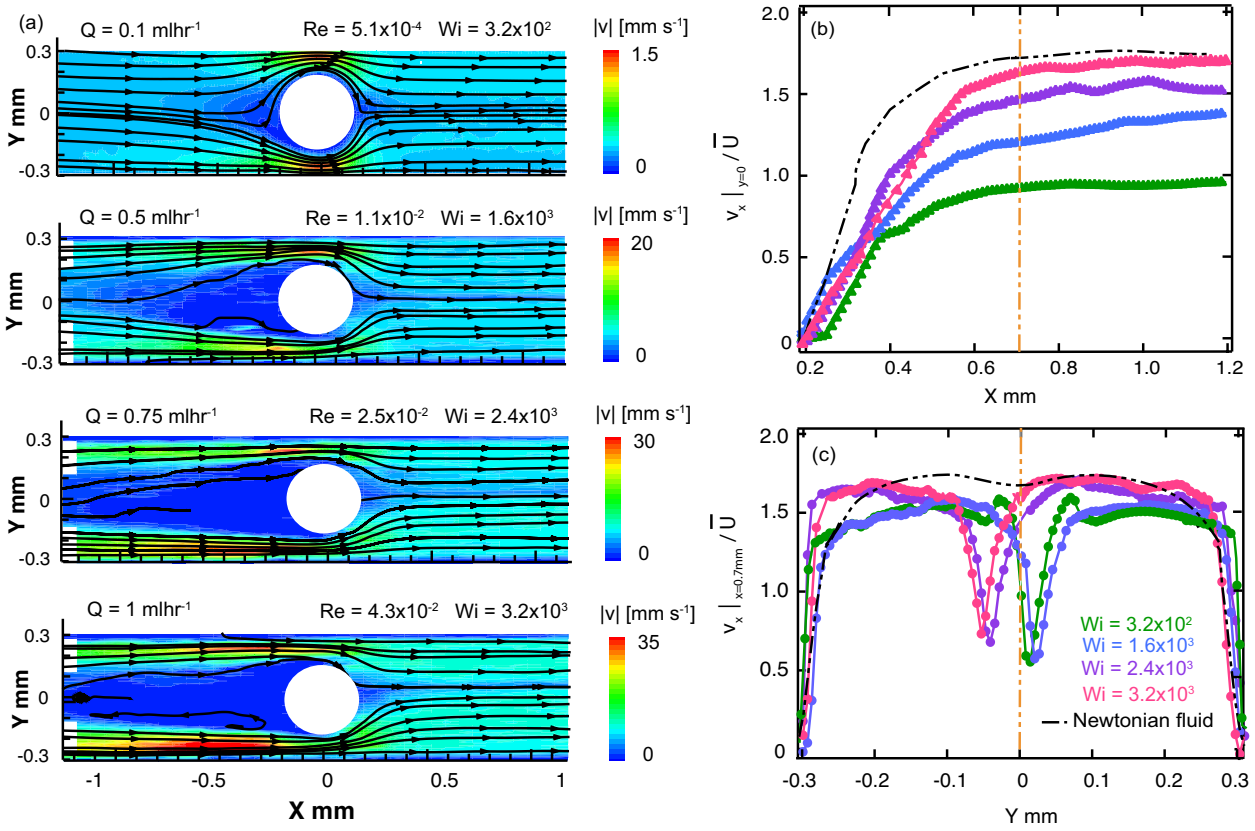

Figure 3.10: (a) Velocity magnitude maps with superimposed streamlines constructed by using μPIV at flow rates 0.1 mL/h $< Q <$ 1 mL/h for the flow of the WLM solution in Device 2 ($\beta = 0.67$). Different colors correspond to different velocity magnitudes, with color bars shown on the right. (b) Normalized streamwise velocity profiles along the channel center line $y = 0$ mm, downstream of the cylinder. (c) Normalized streamwise velocity profiles across the channel at $x = 0.7$ mm. The velocities are normalized by the average velocity $\bar{U} = \frac{Q}{WH}$ in the channel. Black dashed lines correspond to the normalized Newtonian fluid velocity profiles that are approximately independent of the flow rate.

velocity has an increased tendency to deviate from the flow axis ($y = 0$) as compared with Device 1 (see Fig. 3.9 (b,c)). This deviation from the flow axis appears to be connected with the asymmetric division of the flow either side of the cylinder, so is most likely a result of coupling with the time-dependent flow instability upstream of the cylinder.

3.3.3 Upstream vortex growth of wormlike micellar flow

Here we examine the growth of the recirculating vortices observed upstream of the cylinders in all 3 Devices as the Wi is increased. We quantify the vortex length L by measuring the distance along x between the leading edge of the cylinder and the location upstream of the cylinder where streamlines diverge. The length of the vortex L at each flow rate is averaged from a sequence of 5 streak images and is normalized by the cylinder diameter D to obtain the dimensionless vortex length $\chi = L/D$, which is plotted as a function of Wi in Fig. 3.11. Error bars on the data points in Fig. 3.11 represent the standard deviation of each sample of 5 measurements. The dimensionless vortex length χ increases gradually with increasing Wi, following a similar trend for all three devices and tending to a plateau value of $\chi \approx 3$ ($L \approx 3D$) for $Wi \geq 3 \times 10^3$, before the flow upstream of the cylinder becomes unsteady and time-dependent. The behavior is similar to that reported by Kenney et al.[279] for the growth of vortices upstream of a confined cylinder with a highly elastic semidilute poly(ethylene oxide) solution. However, unlike Kenney et al.[279] in no cases do we observe a periodic growth and collapse cycle of the vortices.

3.3.4 Flow pattern and phase diagram

We summarize the transitions between the various flow patterns observed with our WLM solution in all three microfluidic cylinder devices using $Wi - \beta$ state space, see Fig. 3.12. The flow of WLM solution displayed at least five distinct regimes in all experiments. Note that experiments with othere values of W/H are likely to have similar transitions but not the same values of Wi. We categorize the various flow states in our setup as described below:

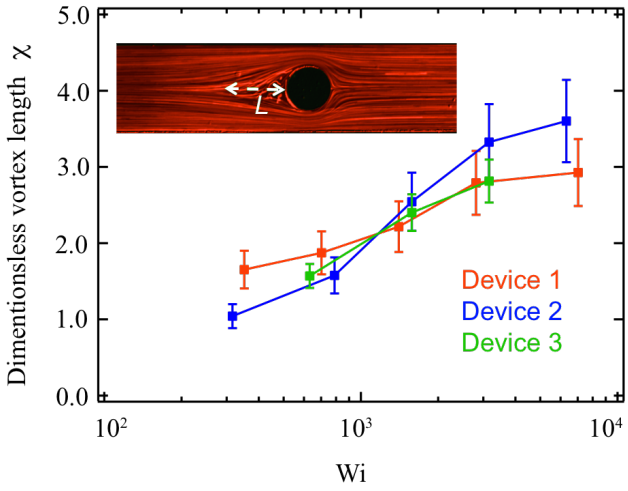

Figure 3.11: Dimensionless vortex length ($\chi = \frac{L}{D}$) as a function of Wi for 3 different blockage ratio devices. The insert illustrates the definition of vortex length L.

- Newtonian-like flow: flow is steady and both fore-aft and laterally symmetric around the cylinder

- Bending streamlines: streamlines become distorted in the compressional flow at the forward cylinder stagnation point due to the onset of elastic effects.

- Vortex growth upstream: streamlines begin to diverge upstream of the cylinder leading edge; a recirculating region develops and a vortex grows with increasing Wi

- Unsteady downstream: time-dependent motion of streamlines is observed downstream

- 3D and time-dependent: flow becomes unsteady both upstream and downstream with quasi-periodic or chaotic appearance upstream, which the streak lines are different from frames

These flow regimes occur over a very wide variation in the Wi between O(1) up to O(10^5), but while inertial effects in the flow remain low with the Re in the range $10^{-7} \leq Re \leq 10$.

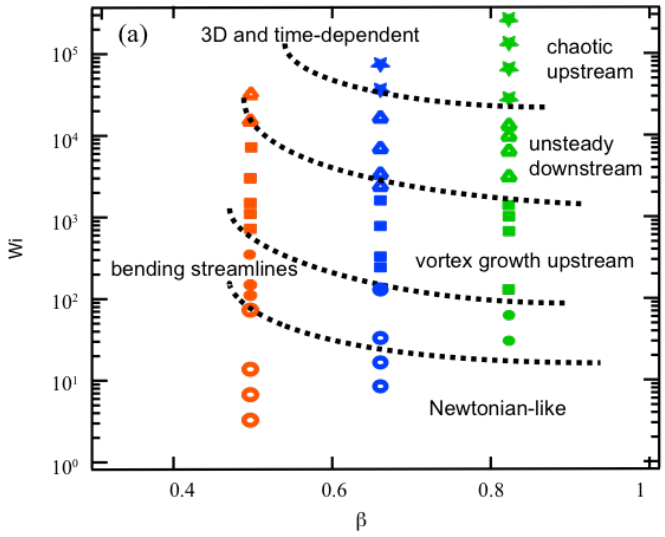

Figure 3.12: Summary $Wi-\beta$ state space of flow patterns identified for 60 mM CTAB/SHNC solution flowing past confined microfluidic cylinders with 3 different blockage ratios: orange symbols - Device 1 ($\beta = 0.5$); blue symbols - Device 2 ($\beta = 0.67$); green symbols - Device 3 ($\beta = 0.83$)

Rodd et al.[134] reported the onset of transition from Newtonian like flow patterns to bending streamlines at a critical $Wi_c \simeq 50$ for semi-dilute polyethylene oxide (PEO) solutions through a micro-fabricated contraction expansion channel (with a contraction ratio of 16:1) and with the Wi defined within the narrow contraction[134,135]. In our confined cylinder devices, we also define our Wi in the narrow constriction regions and we observe the initial onset of flow transitions due to elastic effects occurs at comparable Wi_c. However, in our system there is some dependence of the critical Wi on the blockage ratio β (see Fig. 3.12), with $Wi_c \simeq 100$ in Device 1, $Wi_c \simeq 50$ in Device 2, and $Wi_c \simeq 20$ in Device 3. The onset of instabilities in the WLM solution showed a clear dependence on the spatial confinement resulting from the increasing blockage ratio. Kenney et al.[279] reported flow instabilities with semi-dilute PEO solutions flowing around a microfluidic cylinder device with a cylinder blockage ratio of $\beta = 0.65$. They proposed that the instabilities they observed were purely elastic in origin but were affected by inertia. Also working with semi-dilute PEO solutions,

Shi et al.[285] proposed that instability arose due to the speed of the base flow exceeding that of the elastic traveling wave at a viscoelastic Mach number $Ma = \sqrt{Re \times De} > 1$. However, in our experiments the elasticity numbers are significantly higher than those in the experiments of Kenney et al. and Shi et al.[279,285] Here, the elasticity varies in the range $10^4 \leq El \leq 10^7$, depending on the flow rate (due to shear thinning) whereas the elasticity of the most elastic fluid studied by Kenney et al was $El = 88$[279]. The instabilities observed by Shi et al.[285] arose for relatively moderate values of the Re ($0.1 \leq Re \leq 1$,). In our work, instabilities in the form of bending and asymmetric streamlines become apparent for Reynolds numbers as low as $Re \approx 10^{-5}$, indicating that inertia is negligible in our case. We have evaluated the viscoelastic Mach numbers at the onset of instability in our experiment (using the same definitions of Re and De employed by Shi et al.[285]) and we find in all three cases that $Ma << 1$. Therefore we consider instabilities for the flow of our WLM solution in our single cylinder devices to be purely elastic in origin. We associate the onset of instability upstream of the cylinder with the compression at the leading edge of the cylinder and the growth of viscoelastic stresses generated by the squeezing flow into the the narrow gaps between the cylinder and the channel walls. Downstream of the cylinder, there is significant growth of viscoelastic stress originating from the trailing stagnation point, which results in strong flow modification in the wake of the cylinder This may be the cause of the onset of flow instability in the downstream wake, although coupling with instability and time dependent flow upstream also appears to be a strong factor influencing the onset of the time dependent motion of streamlines observed in the downstream.

3.4 Discussions and Conclusions

In this chapter, we investigated the flow of a Newtonian fluid and a viscoelastic wormlike micellar solution prepared from CTAB with a strong hydrotropic salt past three microfluidic cylinder devices with different blockage ratios. For Newtonian fluid flow, we have used flow diagnostic techniques including streak imaging and flow velocimetry to show both fore-aft and lateral symmetry of the flow with smooth streamlines around the cylinder over a range of Re

comparable to those encountered in experiments with the WLM solution. In our experiments with the WLM solution, we have used streak imaging, quantitative flow velocimetry and FIB imaging to document a sequence of elastic flow instabilities that occur for low Re but as the Wi is increased to very high values. We observe some contrasting effects compared with previous experiments carried out with viscoelastic polymer solutions. In particular with our WLM solution, instability is first apparent in the form of bending and distorted streamlines upstream of the cylinder, not downstream of the cylinder as reported by Kenney et al. and Shi et al.[279,285]. Also, as the instability develops we observe smoothly diverging streamlines upstream of the cylinder, as opposed to the "pinching" streamlines typically observed with polymer solutions[279,285]. In addition, in our experiments the viscoelastic Mach number are apparently too low to account for the observed instabilities[285]. Our results suggest that the instabilities observed upstream of the cylinder are associated with the growth of high stresses generated in the viscoelastic WLM fluid as it accelerates into the narrow gaps between the cylinder and the channel walls. The instabilities downstream of the cylinder are most likely associated with stresses generated by strong extensional deformations at the trailing stagnation point and the resulting flow modification in the wake, and are influenced by the onset of time-dependent flow in the upstream region. Furthermore, the onset of flow instabilities and flow patterns of the WLM solution are sensitive to the degree of confinement resulting from the variation of the blockage ratio of the channels.

The characteristic shear rates imposed within the microchannels lie in the range $0.1 \leq \dot{\gamma} \leq 1000$ s^{-1}, which coincides with the shear-banding stress-plateau regime in the steady flow curve see Fig 3.1. Therefore, the instabilities we report are also likely to be affected by strong shear thinning and non-uniform distributions of stresses and structural interactions between micelles.

In this work we did not observe evidence of the formation of the Flow-Induced Structured Phase (FISP) that has been reported previously for flows of WLM solutions through arrays of cylinders and through microscale models of porous media. This may be because the degree of spatial confinement in our devices was insufficient, or because shear and elongation

rates were too low, or because the total fluid strains imposed were not great enough to induce the formation of FISP[71]. In future work we intend to increase the complexity of our microfluidic devices through combinations of multiple aligned cylinders, staggered cylinders, etc, systematically varying the spatial confinement, strain rate and total available fluid strain. Our eventual aim is to approach a closer model of a real porous medium while building an understanding of the geometrical and rheological factors that affect flow stability (or onset of instability) and the potential formation of FISP in fluidic systems relevant to enhanced oil and gas extraction from underground reservoirs.

Chapter 4

SUMMARY

In this thesis, we have studied the rheology and flow instabilities of CTAB/SHNC mixture under various flow conditions. With SHNC as counter ions, domains of $\pi-\pi$ ions were paired and cation–π groups were formed between HNC^- ions and adjacent hydrophobic CTAB headgroups, inducing more viscoelastic and stable micellar networks compared to that of the CTAB/NaSal system. These micelles have exhibited rich flow behaviors in confined microfluidic geometries, with a combination of shear and extension around the cylinder. The flow instabilities are likely a result of elasticity and non-uniform distributions of stresses that originates from shear banding fluid. Investigations of spatial resolution of heterogeneous bands, formation of shear induced structure phase and localization of stresses at different deformations by rheo-optics, rheo-PIV will be considered in the future work to correlate shear stress and flow-birefringence, and flow instability in the CTAB/SHNC system. A fully flow instability transition of PEO solution with the same confined microfluidic cylinders should be studied to further compare with the transient behavior originated from microstructural transitions in highly viscoelastic hydrotropic micellar system.

BIBLIOGRAPHY

[1] M. A. Fardin, B. Lasne, O. Cardoso, G. Gregoire, M. Argentina, J. P. Decruppe, S. Lerouge, Taylor-like vortices in shear-banding flow of giant micelles, Phys. Rev. Lett. 103 (2009) 028302–4.

[2] P. Nghe, S. M. Fielding, P. Tabeling, A. Ajdari, Interfacially driven instability in the microchannel flow of a shear-banding fluid, Phys. Rev. Lett. 104 (2010) 248303–4.

[3] S. J. Haward, G. H. McKinley, Stagnation point flow of wormlike micellar solutions in a microfluidic cross-slot device: Effects of surfactant concentration and ionic environment, Phys. Rev. E 85 (2012) 031502–14.

[4] N. Dubash, P. Cheung, A. Q. Shen, Elastic instabilities in a microfluidic cross-slot flow of wormlike micellar solutions, Soft Matter 8 (2012) 5847–56.

[5] T. Ober, S. Haward, C. Pipe, J. Soulages, G. McKinley, Microfluidic extensional rheometry using a hyperbolic contraction geometry, Rheol. Acta 52 (2013) 529–46.

[6] C. H. Liu, D. J. Pine, Shear-induced gelation and fracture in micellar solutions, Phys Rev. Lett. 77 (1996) 2121–4.

[7] P. Cheung, N. Dubash, A. Q. Shen, Local micelle concentration fluctuations in microfluidic flows and its relation to a flow-induced structured phase (FISP), Soft Matter 8 (2012) 2304–9.

[8] J. J. Cardiel, A. C. Dohnalkova, N. Dubash, Y. Zhao, P. Cheung, A. Q. Shen, Microstructure and rheology of a flow-induced structured phase in wormlike micellar solutions, Proc. Natl. Acad. Sci. U. S. A. 110 (2013) E1653–60.

[9] C. Manohar, U. R. K. Rao, B. S. Valaulikar, R. M. Iyer, On the origin of viscoelasticity in micellar solutions of cetyltrimethylammonium bromide and sodium salicylate, J. Chem. Soc. Chem. Commun. 5 (1986) 379–381.

[10] B. K. Mishra, S. D. Samant, P. Pradhan, S. B. Mishra, C. Manohar, A new strongly flow birefringent surfactant system, Langmuir 9 (1993) 894–898.

[11] J. N. Israelachvili, Intermolecular and Surface Forces: With Applications to Colloidal and Biological Systems, Academic Press, London, 1985.

[12] H. Hoffmann, H. Löbl, H. Rehage, I. Wunderlich, Rheology of surfactant solutions, Tenside, Deterg. 22 (1985) 290–8.

[13] H. Rehage, H. Hoffmann, Rheological properties of viscoelastic surfactant systems, J. Phys. Chem. 92 (1988) 4712–9.

[14] H. Hoffmann, Viscoelastic surfactant solutions, Structure and Flow in Surfactant Solutions Chapter 1 (1994) 2–31.

[15] R. Abdel-Rahem, The influence of hydrophobic counterions on micellar growth of ionic surfactants, Adv. Colloid Interface Sci. 141 (2008) 24–36.

[16] J. Brackman, J. Engberts, Influence of polymers on the micellization of cetyltrimethylammonium salts, Langmuir 7 (1991) 2097–102.

[17] V. Hartmann, R. Cressely, Influence of sodium salicylate on the rheological behaviour of an aqueous CTAB solution, Colloids Surf., A 121 (1997) 151–62.

[18] W. J. Kim, S. M. Yang, Effects of sodium salicylate on the microstructure of an aqueous micellar solution and its rheological responses, J. Colloid Interface Sci. 232 (2000) 225–34.

[19] C. Oelschlaeger, G. Waton, S. J. Candau, Rheological behavior of locally cylindrical micelles in relation to their overall morphology, Langmuir 19 (2003) 10495–500.

[20] C. A. Dreiss, Wormlike micelles : Where do we stand? Recent developments, linear rheology and scattering techniques, Soft Matter 3 (2007) 956–70.

[21] S. Ezrahi, E. Tuval, A. Aserin, Properties, main applications and perspectives of worm micelles, Adv. Colloid Interface Sci. 128 (2006) 77–102.

[22] G. C. Maitland, Oil and gas production, Curr. Opin. Colloid Interface Sci. 5 (2000) 301–11.

[23] D. Ohlendorf, W. Interthal, H. Hoffmann, Surfactant systems for drag reduction: Physico-chemical properties and rheological behaviour, Rheol. Acta 25 (1986) 468–86.

[24] S. J. Candau, R. Oda, Linear viscoelasticity of salt-free wormlike micellar solutions, Colloids Surf., A 183 (2001) 5–14.

[25] T. M. Clausen, P. K. Vinson, J. R. Minter, H. T. Davis, Y. Talmon, W. G. Miller, Viscoelastic micellar solutions-microscopy and rheology, J. Phys. Chem. 96 (1992) 474–84.

[26] T. S. Davies, A. M. Ketner, S. R. Raghavan, Self-assembly of surfactant vesicles that transform into viscoelastic wormlike micelles upon heating, J. Am. Chem. Soc. 128 (2006) 6669–75.

[27] S. R. Raghavan, Distinct character of surfactant gels:a smooth progression from micelles to fibrillar networks, Langmuir 25 (2009) 8382–5.

[28] K. Trickett, J. Eastoe, Surfactant-based gels, Adv. Colloid Interface Sci. 144 (2008) 66–74.

[29] F. Nettesheim, N. J. Wagner, Fast dynamics of wormlike micellar solutions, Langmuir 23 (2007) 5267–9.

[30] H. Rehage, H. Hoffmann, Viscoelastic surfactant solutions-model system for rheological research, Mol. Phys. 74 (1991) 933–73.

[31] T. Shikata, S. J. Dahman, D. S. Pearson, Rheo-optical behavior of wormlike micelles, Langmuir 10 (1994) 3470–6.

[32] M. E. Cates, Reptation of living polymers-dynamics of entangled polymers in the presence of reversible chain-scission reactions, Macromolecules 20 (1987) 2289–96.

[33] T. Shikata, H. Hirata, T. Kotaka, Micelle formation of detergent molecules in aqueous media: viscoelastic properties of aqueous cetyltrimethylammonium bromide solutions, Langmuir 3 (1987) 1081–6.

[34] T. Shikata, H. Hirata, T. Kotaka, Micelle formation of detergent molecules in aqueous media. 2. role of free salicylate ions on viscoelastic properties of aqueous cetyltrimethylammonium bromide-sodium salicylate solutions, Langmuir 4 (1988) 354–359.

[35] T. Shikata, T. Kotaka, Entanglement network of thread-like micelles of a cationic detergent, J. Non-Cryst. Solids 131-133 (1991) 831–5.

[36] M. Carvalho, M. Padmanabhan, C. Macosko, Single-point correction for parallel disks rheometry, J. Rheol. 38 (1994) 1925–36.

[37] C. Clasen, G. McKinley, Gap-dependent microrheometry of complex liquids, J. Non-Newtonian Fluid Mech. 124 (2004) 1–10.

[38] S. J. Haward, T. J. Obe, M. S. N. Oliveira, M. A. Alves, G. H. McKinley, Extensional rheology and elastic instabilities of a wormlike micellar solution in a microfluidic cross-slot device, Soft Matter 8 (2012) 536–55.

[39] C. Masselon, A. Colin, P. D. Olmsted, Influence of boundary conditions and confinement on nonlocal effects in flows of wormlike micellar systems, Phys. Rev. E 81 (2010) 021502–15.

[40] C. Masselon, J. B. Salmon, A. Colin, Nonlocal effects in flows of wormlike micellar solutions, Phys. Rev. Lett. 10 (2008) 038301–4.

[41] P. Nghe, G. Degre, P. Tabeling, A. Ajdari, High shear rheology of shear banding fluids in microchannels, Appl. Phys. Lett. 93 (2008) 204102–3.

[42] P. Nghe, E. Terriac, M. Schneider, Z. Z. Li, M. Cloitre, B. Abecassis, P. Tabeling, Microfluidics and complex fluids, Lab Chip 11 (2011) 788–94.

[43] T. J. Ober, J. Soulages, G. H. McKinley, Spatially resolved quantitative rheo-optics of complex fluids in a microfluidic device, J. Rheol. 55 (2011) 1127–59.

[44] J. A. Pathak, S. D. Hudson, Rheo-optics of equilibrium polymer solutions : Wormlike micelles in elongational flow in a microfluidic cross-slot, Macromolecules 39 (2006) 8782–92.

[45] C. J. Pipe, T. S. Majmudar, G. H. McKinley, High shear rate viscometry, Rheol. Acta 47 (2008) 621–42.

[46] C. J. Pipe, G. H. McKinley, Microfluidic rheometry, Mech. Res. Commun. 36 (2009) 110–20.

[47] P. T. Callaghan, Rheo-NMR: nuclear magnetic resonance and the rheology of complex fluids, Rep. Prog. Phys. 62 (1999) 599–670.

[48] S. M. Fielding, Complex dynamics of shear banded flows, Soft Matter 3 (2007) 1262–79.

[49] S. Manneville, Recent experimental probes of shear banding, Rheol. Acta 47 (2008) 301–18.

[50] P. D. Olmsted, Perspectives on shear banding in complex fluids, Rheol. Acta 47 (2008) 283–300.

[51] L. M. Walker, Scattering from polymer-like micelles, Curr. Opin. Colloid Interface Sci. 14 (2009) 451–4.

[52] G. Ovarlez, S. Rodts, X. Chateau, P. Coussot, Phenomenology and physical origin of shear localization and shear banding in complex fluids, Rheol. Acta 48 (2009) 831–44.

[53] A. Q. Shen, P. Cheung, The freedom of confinement in complex fluids, Phys. Today 63 (2010) 30–5.

[54] S. Lerouge, J. F. Berret, Shear-induced transitions and instabilities in surfactant wormlike micelles, Adv. Polym. Sci. 230 (2010) 1–71.

[55] G. M. Whitesides, The origins and the future of microfluidics, Nature 442 (2006) 368–73.

[56] D. N. Breslauer, S. J. Muller, L. P. Lee, Generation of monodisperse silk microspheres prepared with microfluidics, Biomacromolecules 11 (2010) 643–7.

[57] J. S. Wexler, P. H. Trinh, H. Berthet, N. Quennouz, O. du Roure, H. E. Huppert, A. Linder, H. A. Stone, Bending of elastic fibres in viscous flows: the influence of confinement, J. Fluid Mech. 733 (2013) 684–84.

[58] S. Gulati, D. Liepmann, S. J. Muller, Elastic secondary flows of semidilute DNA solutions in abrupt 90 degrees microbends, Phys. Rev. E 78 (2008) 036314.

[59] W. Xu, S. J. Muller, Polymer-monovalent salt-induced DNA compaction studied via single-molecule microfluidic trapping, Lab Chip 12 (2012) 647–51.

[60] W. R. DiLuzio, L. Turner, M. Mayer, P. Garstecki, D. B. Weibel, H. C. Berg, G. M. Whitesides, Escherichia coli swim on the right-hand side, Nature 435 (2005) 1271–4.

[61] A. Costanzo, R. Di Leonardo, G. Ruocco, L. Angelani, Transport of self-propelling bacteria in micro-channel flow, J. Phys. Condens. Matter 24 (2012) 065101–9.

[62] E. Altshuler, G. Mino, C. Perez-Penichet, L. d. Rio, A. Lindner, A. Rousselet, E. Clement, Flow-controlled densification and anomalous dispersion of e. coli through a constriction, Soft Matter 9 (2013) 1864–70.

[63] H. A. Stone, A. D. Stroock, A. Ajdari, Engineering flows in small devices: Microfluidics toward a lab-on-a-chip, Ann. Rev. Fluid Mech. 36 (2004) 381–411.

[64] T. M. Squires, S. R. Quake, Microfluidics: Fluid physics at the nanoliter scale, Rev. Mod. Phys. 77 (2005) 977–1026.

[65] R. Attia, D. C. Pregibon, P. S. Doyle, J. L. Viovy, D. Bartolo, Soft microflow sensors, Lab Chip 9 (2009) 1213–8.

[66] F. J. Galindo-Rosales, M. A. Alves, M. S. N. Oliveira, Microdevices for extensional rheometry of low viscosity elastic liquids: a review, Microfluid Nanofluidics 14 (2013) 1–19.

[67] S. J. Haward, F. J. Galindo-Rosales, P. Ballesta, M. A. Alves, Spatiotemporal flow instabilities of wormlike micellar solutions in rectangular microchannels, Appl. Phys. Lett. 104 (2014) 124101.

[68] G. Arya, A. Panagiotopoulos, Log-rolling micelles in sheared amphiphilic thin films, Phys. Rev. Lett. 95 (2005) 188301–4.

[69] G. Davies, J. Stokes, Thin film and high shear rheology of multiphase complex fluids, J. Non-Newtonian Fluid Mech. 148 (2008) 73–87.

[70] M. Vasudevan, E. Buse, D. L. Lu, H. Krishna, R. Kalyanaraman, A. Q. Shen, B. Khomami, R. Sureshkumar, Irreversible nanogel formation in surfactant solutions by microporous flow, Nat. Mater. 9 (2010) 436–41.

[71] N. Dubash, J. J. Cardiel, P. Cheung, A. Q. Shen, A stable flow-induced structured phase in wormlike micellar solutions, Soft Matter 7 (2011) 876–9.

[72] F. J. Galindo-Rosales, L. Campo-Deano, F. T. Pinho, E. van Bokhorst, P. J. Hamersma, M. S. N. Oliveira, M. A. Alves, Microfluidic systems for the analysis of

viscoelastic fluid flow phenoemna in porous media, Microfluid Nanofluidics 12 (2012) 485–98.

[73] J. Holweg, P. Brunn, F. Durst, Proceedings, 4th Europ. Symp. on Enhanced Oil Recoverydgmk, Hamburg (1987) 1007–18.

[74] J. Holweg, P. Brunn, F. Durst, Progress and Trends in Rheology II, Steinkopff, 1988.

[75] P. Brunn, J. Holweg, The effect of shear in porous medium flow of surfactant solutions, J. Non-Newtonian Fluid Mech. 30 (1988) 317–24.

[76] P. Brunn, J. Holweg, The Flow of Surfactant Solutions Through Porous Media: Universal Laws, Springer Netherlands, 1990.

[77] E. Cappelaere, R. Cressely, J. P. Decruppe, Linear and non-linear rheological behaviour of salt-free aqueous CTAB solutions, Colloids Surf., A 104 (1995) 353–74.

[78] E. Cappelaere, J. F. Berret, J. P. Decruppe, R. Cressely, P. Lindner, Rheology, birefringence, and small-angle neutron scattering in a charged micellar system: Evidence of a shear-induced phase transition, Phys. Rev. E 56 (1997) 1869–78.

[79] M. M. Britton, P. T. Callaghan, Two-phase shear band structures at uniform stress, Phys. Rev. Lett. 78 (1997) 4930–3.

[80] W. M. Holmes, M. R. Lopez-Gonzalez, P. T. Callaghan, Shear-induced constraint to amphiphile chain dynamics in wormlike micelles (vol 66, pg 132, 2004), Europhys. Lett. 66 (2004) 132–8.

[81] J. B. Salmon, A. Colin, S. Manneville, F. Molino, Velocity profiles in shear-banding wormlike micelles, Phys. Rev. Lett. 90 (2003) 228303–4.

[82] Y. T. Hu, A. Lips, Kinetics and mechanism of shear banding in an entangled micellar solution, J. Rheol. 49 (2005) 1001–27.

[83] S. Manneville, L. Becu, A. Colin, High-frequency ultrasonic speckle velocimetry in sheared complex fluids, The European Physical Journal Applied Physics 28 (2004) 361–73.

[84] L. Bécu, S. Manneville, A. Colin, Spatiotemporal dynamics of wormlike micelles under shear, Phys. Rev. Lett. 93 (2004) 018301–4.

[85] J. F. Berret, D. C. Roux, G. Porte, Isotropic to nematic transition in wormlike micelles under shear, J. Phys. II 4 (1994) 1261–79.

[86] J. F. Berret, Transient rheology of wormlike micelles, Langmuir 13 (1997) 2227–34.

[87] J. F. Berret, G. Porte, J. P. Decruppe, Inhomogeneous shear rows of wormlike micelles: A master dynamic phase diagram, Phys. Rev. E 55 (1997) 1668–76.

[88] S. Lerouge, J. P. Decruppe, C. Humbert, Shear banding in a micellar solution under transient flow, Phys. Rev. Lett. 81 (1998) 5457–60.

[89] P. Fischer, E. K. Wheeler, G. G. Fuller, Shear-banding structure orientated in the vorticity direction observed for equimolar micellar solution, Rheol. Acta 41 (2002) 35–44.

[90] J. Y. Lee, G. G. Fuller, N. E. Hudson, X. F. Yuan, Investigation of shear-banding structure in wormlike micellar solution by point-wise flow-induced birefringence measurements, J. Rheol. 49 (2005) 537–50.

[91] J. P. Decruppe, O. Greffier, S. Manneville, S. Lerouge, Local velocity measurements in heterogeneous and time-dependent flows of a micellar solution, Phys. Rev. E 73 (2006) 061509–8.

[92] J. Drappier, D. Bonn, J. Meunier, S. Lerouge, J. P. Decruppe, F. Bertrand, Correlation between birefringent bands and shear bands in surfactant solutions, J. Stat. Mech. 06 (2006) 04003–12.

[93] M. W. Liberatore, F. Nettesheim, N. J. Wagner, L. Porcar, Spatially resolved small-angle neutron scattering in the 1-2 plane: A study of shear-induced phase-separating wormlike micelles, Phys. Rev. E 73 (2006) 020504.

[94] E. Miller, J. P. Rothstein, Transient evolution of shear-banding wormlike micellar solutions, J. Non-Newtonian Fluid Mech 143 (2007) 22–37.

[95] M. A. Fardin, D. Lopez, J. Croso, G. Gregoire, O. Cardoso, G. H. McKinley, S. Lerouge, Elastic turbulence in shear banding wormlike micelles, Phys. Rev. Lett. 104 (2010) 178303–4.

[96] S. M. Fielding, H. J. Wilson, Shear banding and interfacial instability in planar poiseuille flow, J. Non-Newtonian Fluid Mech 165 (2010) 196–202.

[97] M. A. Fardin, T. J. Ober, C. Gay, G. Gregoire, G. H. McKinley, S. Lerouge, Criterion for purely elastic Taylor-Couette instability in the flows of shear-banding fluids, Europhys. Lett. 96 (2011) 44004–6.

[98] M. A. Fardin, T. Divoux, M. A. Guedeau-Boudeville, I. Buchet-Maulien, J. Browaeys, G. H. McKinley, S. Manneville, S. Lerouge, Shear-banding in surfactant wormlike micelles: elastic instabilities and wall slip, Soft Matter 8 (2012) 2535–53.

[99] M. W. Liberatore, F. Nettesheim, P. A. Vasquez, M. E. Helgeson, N. J. Wagner, E. W. Kaler, L. P. Cook, L. Porcar, Y. T. Hu, Microstructure and shear rheology of entangled wormlike micelles in solution, J. Rheol. 53 (2009) 441–58.

[100] M. E. Helgeson, P. A. Vasquez, E. W. Kaler, N. J. Wagner, Rheology and spatially resolved structure of cetyltrimethylammonium bromide wormlike micelles through the shear banding transition, J. Rheol. 53 (2009) 727–56.

[101] M. E. Helgeson, M. D. Reichert, Y. T. Hu, N. J. Wagner, Relating shear banding, structure, and phase behavior in wormlike micellar solutions, Soft Matter 5 (2009) 3858–69.

[102] N. A. Spenley, M. E. Cates, T. C. B. McLeish, Nonlinear rheology of wormlike micelles, Phys. Rev. Lett. 71 (1993) 939–42.

[103] M. A. Fardin, T. J. Ober, C. Gay, G. Gregoire, G. H. McKinley, S. Lerouge, Potential "ways of thinking" about the shear-banding phenomenon, Soft Matter 8 (2012) 910–22.

[104] J. Beaumont, N. Louvet, T. Divoux, M. A. Fardin, H. Bodiguel, S. Lerouge, S. Manneville, A. Colin, Turbulent flows in highly elastic wormlike micelles, Soft Matter 9 (2013) 735–49.

[105] N. Alexandre, M. Alexander, Nonaxisymmetric instability of shear-banded Taylor-Couette flow, Phys. Rev. Lett. 108 (2012) 0883021–4.

[106] S. Lerouge, M. Argentina, J. P. Decruppe, Interface instability in shear-banding flow, Phys. Rev. Lett. 96 (2006) 0883011–4.

[107] S. M. Fielding, Linear instability of planar shear banded flow, Phys. Rev. Lett. 95 (2005) 134501–4.

[108] J. Dhont, A constitutive relation describing the shear-banding transition, Phys. Rev. E 60 (1999) 4534–44.

[109] S. Lerouge, M. A. Fardin, M. Argentina, G. Gregoire, O. Cardoso, Interface dynamics in shear-banding flow of giant micelles, Soft Matter 4 (2008) 1808–19.

[110] P. Ballesta, M. P. Lettinga, S. Manneville, Superposition rheology of shear-banding wormlike micelles, J. Rheol. 51 (2007) 1047–72.

[111] O. Radulescu, P. D. Olmsted, J. P. Decruppe, S. Lerouge, J. F. Berret, G. Porte, Time scales in shear banding of wormlike micelles, Europhys. Lett. 62 (2003) 230–36.

[112] C. M. Chen, G. G. Warr, Light scattering from wormlike micelles in an elongational field, Langmuir 13 (1997) 1374–6.

[113] J. P. Rothstein, Transient extensional rheology of wormlike micelle solutions, J. Rheol. 47 (2003) 1227–47.

[114] V. J. Anderson, J. R. A. Pearson, E. S. Boek, The rheology of worm-like micellar fluids, Rheology Reviews (2006) 217–53.

[115] P. E. Arratia, C. C. Thomas, J. Diorio, J. P. Gollub, Elastic instabilities of polymer solutions in cross-channel flow, Phys. Rev. Lett. 96 (2006) 144502–4.

[116] A. Bhardwaj, E. Miller, J. P. Rothstein, Filament stretching and capillary breakup extensional rheometry measurements of viscoelastic wormlike micelle solutions, J. Rheol. 51 (2007) 693–719.

[117] J. S. Lee, R. Dylla-Spears, N. P. Teclemariam, S. J. Muller, Microfluidic four-roll mill for all flow types, Appl. Phys. Lett. 90 (2007) 074103–3.

[118] M. S. N. Oliveira, P. J. Oliveira, F. T. Pinho, M. A. Alves, Effect of contraction ratio upon viscoelastic flow in contractions: The axisymmetric case, J. Non-Newtonian Fluid Mech 147 (2007) 92–108.

[119] M. S. N. Oliveira, M. A. Alves, F. T. Pinho, G. H. McKinley, Viscous flow through microfabricated hyperbolic contractions, Exp. Fluids 43 (2007) 437–51.

[120] G. I. Taylor, The formation of emulsions in definable fields of flow, Proc. R. Soc. London, Ser. A 146 (1934) 0501–23.

[121] G. G. Fuller, L. G. Leal, Flow birefringence of dilute polymer solutions in two-dimensional flows, Rheol. Acta 19 (1980) 580–600.

[122] E. C. Lee, S. J. Muller, Flow light scattering studies of polymer coil conformation in solutions in extensional flow, Macromolecules 32 (1999) 3295–305.

[123] D. E. Smith, H. P. Babcock, S. Chu, Single-polymer dynamics in steady shear flow, Science 283 (1999) 1724–7.

[124] C. M. Schroeder, H. P. Babcock, E. S. G. Shaqfeh, S. Chu, Observation of polymer conformation hysteresis in extensional flow, Science 301 (2003) 1515–9.

[125] C. M. Schroeder, R. E. Teixeira, E. S. G. Shaqfeh, S. Chu, Characteristic periodic motion of polymers in shear flow, Phys. Rev. Lett. 95 (2005) 018301–5.

[126] S. D. Hudson, F. R. Phelan, M. D. Handler, J. T. Cabral, K. B. Migler, E. J. Amis, Microfluidic analog of the four-roll mill, Appl. Phys. Lett. 85 (2004) 335–7.

[127] F. R. Phelan, S. D. Hudson, M. D. Handler, Fluid dynamics analysis of channel flow geometries for materials characterization in microfluidic devices, Rheol. Acta 45 (2005) 59–71.

[128] O. Scrivener, C. Berner, R. Cressely, R. Hocquart, R. Sellin, N. S. Vlachos, Dynamical behavior of drag-reducing polymer-solutions, J. Non-Newtonian Fluid Mech. 5 (1979) 475–95.

[129] K. Gardner, E. R. Pike, M. J. Miles, A. Keller, K. Tanaka, Photon-correlation velocimetry of polystyrene solutions in extensional flow-fields, Polymer 23 (1982) 1435–42.

[130] A. Keller, A. J. Müller, J. A. Odell, Entanglements in semi-dilute solutions as revealed by elongational flow studies, Prog. Colloid Polym. Sci. 75 (1987) 179–200.

[131] J. A. Odell, S. P. Carrington, Extensional flow oscillatory rheometry, J. Non-Newtonian Fluid Mech. 137 (2006) 110–20.

[132] A. M. Afonso, M. A. Alves, F. T. Pinho, Purely elastic instabilities in three-dimensional cross-slot geometries, J. Non-Newtonian Fluid Mech 165 (2010) 743–51.

[133] R. J. Poole, M. A. Alves, P. J. Oliveira, Purely elastic flow asymmetries, Phys. Rev. Lett. 99 (2007) 164503–4.

[134] L. E. Rodd, J. J. Cooper-White, D. V. Boger, G. H. McKinley, Role of the elasticity number in the entry flow of dilute polymer solutions in micro-fabricated contraction geometries, J. Non-Newtonian Fluid Mech 143 (2007) 170–91.

[135] L. E. Rodd, T. P. Scott, D. V. Boger, J. J. Cooper-White, G. H. McKinley, The inertio-elastic planar entry flow of low-viscosity elastic fluids in micro-fabricated geometries, J. Non-Newtonian Fluid Mech. 129 (2005) 1–22.

[136] J. Soulages, M. S. N. Oliveira, P. C. Sousa, M. A. Alves, G. H. McKinley, Investigating the stability of viscoelastic stagnation flows in T-shaped microchannels, J. Non-Newtonian Fluid Mech 163 (2009) 9–24.

[137] A. M. Afonso, P. J. Oliveira, F. T. Pinho, M. A. Alves, Dynamics of high-deborah-number entry flows: a numerical study, J. Fluid Mech. 677 (2011) 272–304.

[138] G. R. Moss, J. P. Rothstein, Flow of wormlike micelle solutions through a periodic array of cylinders, J. Non-Newtonian Fluid Mech 165 (2010) 1–13.

[139] G. R. Moss, J. P. Rothstein, Flow of wormlike micelle solutions past a confined circular cylinder, J. Non-Newtonian Fluid Mech 165 (2010) 1505–15.

[140] J. Gladden, A. Belmonte, Motion of a viscoelastic micellar fluid around a cylinder: Flow and fracture, Phys. Rev. Lett.

[141] C. C. Hsieh, S. J. Park, R. G. Larson, Brownian dynamics modeling of flow-induced birefringence and chain scission in dilute polymer solutions in a planar cross-slot flow, Macromolecules 38 (2005) 1456–68.

[142] M. S. N. Oliveira, M. A. Alves, F. T. Pinho, G. H. McKinley, Viscous flow through microfabricated hyperbolic contractions, Exp. Fluids 43 (2007) 437–51.

[143] J. P. Rothstein, G. H. McKinley, Extensional flow of a polystyrene boger fluid through

a 4:1:4 axisymmetric contraction/expansion, J. Non-Newtonian Fluid Mech 86 (1999) 61–88.

[144] J. P. Rothstein, G. H. McKinley, The axisymmetric contraction-expansion: the role of extensional rheology on vortex growth dynamics and the enhanced pressure drop, J. Non-Newtonian Fluid Mech 98 (2001) 33–63.

[145] H. Jahromi, M. F. Webster, J. P. Aguayo, O. Manero, Numerical investigation of transient contraction flows for worm-like micellar systems using bautista-manero models, J. Non-Newtonian Fluid Mech 166 (2011) 102–17.

[146] M. Nystrom, H. R. T. Jahromi, M. Stading, M. F. Webster, Numerical simulations of boger fluids through different contraction configurations for the development of a measuring system for extensional viscosity, Rheol. Acta 51 (2012) 713–27.

[147] D. Rajagopalan, Computational analysis of techniques to determine extensional viscosity from entrance flows, Rheol. Acta 39 (2000) 138–51.

[148] J. T. Padding, W. J. Briels, M. R. Stukan, E. S. Boek, Review of multi-scale particulate simulation of the rheology of wormlike micellar fluids, Soft Matter 5 (2009) 4367–75.

[149] M. R. Stukan, E. S. Boek, J. T. Padding, J. P. Crawshaw, Influence of system size and solvent flow on the distribution of wormlike micelles in a contraction-expansion geometry, Eur. Phys. J. E 26 (2008) 63–71.

[150] M. R. Stukan, E. S. Boek, J. T. Padding, W. J. Briels, J. P. Crawshaw, Flow of wormlike micelles in an expansion-contraction geometry, Soft Matter 4 (2008) 870–9.

[151] G. G. Fuller, Optical Rheometry of Complex Fluids, Oxford University Press, 1995.

[152] X. Ye, R. G. Larson, C. Pattamaprom, T. Sridhar, Extensional properties of monodisperse and bidisperse polystyrene solutions, J. Rheol. 47 (2003) 443–68.

[153] P. Sunthar, D. Nguyen, R. Dubbelboer, J. R. Prakash, T. Sridhar, Measurement and prediction of the elongational stress growth in a dilute solution of DNA molecules, Macromolecules 38 (2005) 10200–9.

[154] X. N. Ye, T. Sridhar, Shear and extensional properties of three-arm polystyrene solutions, Macromolecules 34 (2001) 8270–7.

[155] P. K. Bhattacharjee, D. A. Nguyen, G. H. McKinley, T. Sridhar, Extensional stress growth and stress relaxation in entangled polymer solutions, J. Rheol. 47 (2003) 269–90.

[156] A. Tripathi, K. C. Tam, G. H. McKinley, Rheology and dynamics of associative polymers in shear and extension: theory and experiments, Macromolecules 39 (2006) 1981–99.

[157] S. L. Anna, G. H. McKinley, Effect of a controlled pre-deformation history on extensional viscosity of dilute polymer solutions, Rheol. Acta 47 (2008) 841–59.

[158] A. Bhardwaj, D. Richter, M. Chellamuthu, J. P. Rothstein, The effect of pre-shear on the extensional rheology of wormlike micelle solutions, Rheol. Acta 46 (2007) 861–75.

[159] S. Chen, J. P. Rothstein, Flow of a wormlike micelle solution past a falling sphere, J. Non-Newtonian Fluid Mech 116 (2004) 205–34.

[160] B. Kalpakci, E. E. Klaus, J. L. Duda, R. Nagrajan, Flow characteristics of surfactant solutions in porous media and their role in permeability modification, Soc. ol. Eng. J. 21 (1981) 709–20.

[161] E. Ruckenstein, P. O. Brunn, J. Holweg, Flow-induced creation and destruction of supermicelles in surfactant solutions, Langmuir 4 (1988) 350–4.

[162] J. Vorwerk, P. Brunn, Shearing effects for the flow of surfactant and polymer solutions through a packed bed of spheres, J. Non-Newtonian Fluid Mech. 51 (1994) 79–95.

[163] J. P. Rothstein, Strong flows of viscoelastic wormlike micelle solutions, Rheology Reviews 6 (2008) 1–46.

[164] M. Torres, J. Gonzéz, M. Rojas, A. J. Müller, A. Sáez, D. Löf, K. Schillń, Effect of ionic strength on the rheological behavior of aqueous cetyltrimethylammonium p-toluene sulfonate solutions, J. Colloid Interface Sci. 307 (2007) 221–8.

[165] M. R. Rojas, A. J. Müller, A. E. Sáez, Shear rheology and porous media flow of wormlike micelle solutions formed by mixtures of surfactants of opposite charge, J. Colloid Interface Sci. 326 (2008) 221–6.

[166] J. M. González, A. J. Müller, M. F. Torres, A. E. Sáez, The role of shear and elongation in the flow of solutions of semi-flexible polymers through porous media, Rheol. Acta 44 (2005) 396–405.

[167] A. J. Müller, M. F. Torres, A. E. Sáez, Effect of the flow field on the rheological behavior of aqueous cetyltrimethylammonium p-toluenesulfonate solutions, Langmuir 20 (2004) 3838–41.

[168] T. M. Squires, T. G. Mason, Fluid mechanics of microrheology, Annu. Rev. Fluid Mech. 42 (2010) 413–38.

[169] G. Porte, R. Gomati, O. El Haitamy, J. Appell, J. Marignan, Morphological transformations of the primary surfactant structures in brine-rich mixtures of ternary systems (surfactant/alcohol/brine), J. Phys. Chem. 90 (1986) 5746–51.

[170] T. J. Drye, M. E. Cates, Living networks: The role of crosslinks in entangled surfactant solutions, J. Chem. Phys. 96 (1992) 1367–75.

[171] D. L. Lu, J. J. Cardiel, G. Z. Cao, A. Q. Shen, Nanoporous scaffold with immobilized enzymes during flow-induced gelation for sensitive H_2O_2 biosensing, Adv. Mater. 22 (2010) 2809–13.

[172] E. Mendes, J. Narayanan, R. Oda, F. Kern, S. J. Candau, C. Manohar, Shear-induced vesicle to wormlike micelle transition, J. Phys. Chem. B 101 (1997) 2256–2258.

[173] E. Mendes, R. Oda, C. Manohar, J. Narayanan, A small-angle neutron scattering study of a shear-induced vesicle to micelle transition in surfactant mixtures, J. Phys. Chem. B 102 (1998) 338–343.

[174] J. F. A. Soltero, J. E. Puig, O. Manero, Rheology of the cetyltrimethylammonium tosilatewater system. 2. linear viscoelastic regime, Langmuir 12 (11) (1996) 2654–2662.

[175] M. Carver, T. L. Smith, J. C. Gee, A. Delichere, E. Caponetti, L. J. Magid, Tuning of micellar structure and dynamics in aqueous salt-free solutions of cetyltrimethylammonium mono- and dichlorobenzoates, Langmuir 12 (3) (1996) 691–698.

[176] W. Brown, K. Johansson, M. Almgren, Threadlike micelles from cetyltrimethylammonium bromide in aqueous sodium naphthalenesulfonate solutions studied by static and dynamic light-scattering, J. Phys. Chem. 93 (1989) 5888–5894.

[177] Y. Y. Lin, Y. Qiao, X. H. Cheng, Y. Yan, Z. B. Li, J. B. Huang, Hydrotropic salt promotes anionic surfactant self-assembly into vesicles and ultralong fibers, J. Colloid Interface Sci. 369 (2012) 238–244.

[178] T. K. Hodgdon, E. W. Kaler, Hydrotropic solutions, Curr. Opin. Colloid Interface Sci. 12 (2006) 121–128.

[179] M. H. Hatzopoulos, J. Eastoe, P. J. Dowding, S. E. Rogers, R. Heenan, R. Dyer, Are hydrotropes distinct from surfactants?, Langmuir 27 (2011) 12346–12353.

[180] D. Subramanian, C. T. Boughter, J. B. Klauda, B. Hammouda, M. A. Anisimov, Mesoscale inhomogeneities in aqueous solutions of small amphiphilic molecules, Faraday Discuss. 167 (2013) 217–238.

[181] B. A. Schubert, E. W. Kaler, N. J. Wagner, The microstructure and rheology of mixed cationic/anionic wormlike micelles, Langmuir 19 (2003) 4079–4089.

[182] B. D. Frounfelker, G. C. Kalur, B. H. Cipriano, D. Danino, S. R. Raghavan, Persistence of birefringence in sheared solutions of wormlike micelles, Langmuir 25 (2008) 167–172.

[183] S. Mishra, B. K. Mishra, S. D. Samant, J. Narayanan, C. Manohar, Charge-induced nematic-isotropic transition in mixed surfactant solutions, Langmuir 9 (1993) 2804–2807.

[184] R. Abdel-Rahem, The influence of hydrophobic counterion on the phase behavior of ionic surfactants, Tenside Surfactants Detergents 42 (2005) 95–101.

[185] R. Krishnaswamy, S. K. Ghosh, S. Lakshmanan, V. A. Raghunathan, A. K. Sood, Phase behavior of concentrated aqueous solutions of cetyltrimethylammonium bromide (CTAB) and sodium hydroxy naphthoate (SHN), Langmuir 21 (2005) 10439–10443.

[186] E. W. Kaler, A. K. Murthy, B. E. Rodriguez, J. A. N. Zasadzinski, Spontaneous vesicle formation in aqueous mixtures of single-tailed surfactants, Science 245 (1989) 1371–1374.

[187] P. A. Hassan, B. S. Valaulikar, C. Manohar, F. Kern, L. Bourdieu, S. J. Candau, Vesicle to micelle transition: rheological investigations, Langmuir 12 (1996) 4350–4357.

[188] K. Horbaschek, H. Hoffmann, C. Thunig, Formation and properties of lamellar phases in systems of cationic surfactants and hydroxy-naphthoate, J. Colloid Interface Sci. 206 (1998) 439–456.

[189] R. Abdel-Rahem, M. Gradzielski, H. Hoffmann, A novel viscoelastic system from a cationic surfactant and a hydrophobic counterion, J. Colloid Interface Sci. 288 (2005) 570–582.

[190] S. Gravsholt, Viscoelasticity in highly dilute aqueous solutions of pure cationic detergents, J. Colloid Interface Sci. 57 (1976) 575–577.

[191] G. C. Kalur, B. D. Frounfelker, B. H. Cipriano, A. I. Norman, S. R. Raghavan, Viscosity increase with temperature in cationic surfactant solutions due to the growth of wormlike micelles, Langmuir 21 (2005) 10998–11004.

[192] G. Verma, V. K. Aswal, G. Fritz-Popovski, C. P. Shah, M. Kumar, P. A. Hassan, Dilution induced thickening in hydrotrope-rich rod-like micelles, J. Colloid Interface Sci. 359 (2011) 163–170.

[193] U. R. K. Rao, C. Manohar, B. S. Valaulikar, R. M. Iyer, Micellar chain model for the origin of the visoelasticity in dilute surfactant solutions, J. Phys. Chem. 91 (1987) 3286–3291.

[194] M. Ouchi, T. Takahashi, M. Shirakashi, Rheological properties of shear-induced structure in ctab/nasal aqueous solution - viscosity and elasticity change under start-up flows, Nihon Reoroji Gakkaishi. 35 (2007) 107–114.

[195] M. Vasudevan, A. Shen, B. Khomami, R. Sureshkumar, Self-similar shear thickening behavior in CTAB/NaSal surfactant solutions, J. Rheol. 52 (2) (2008) 527–550.

[196] J. J. Cardiel, Y. Zhao, P. De La Iglesia, L. D. Pozzo, A. Q. Shen, Turning up the heat on wormlike micelles with a hydrotopic salt in microfluidics, Soft Matter 10 (2014) 9300–9312.

[197] J. J. Cardiel, Y. Zhao, L. Tonggu, L. G. Wang, J. H. Chung, A. Q. Shen, Flow-induced immobilization of glucose oxidase in nonionic micellar nanogels for glucose sensing, Lab Chip 14 (2014) 3912–3916.

[198] M. E. Cates, S. J. Candau, Statics and dynamics of worm-like surfactant micelles, J. Phys.: Condens. Matter 33 (1990) 6869–6892.

[199] M. Doi, S. F. Edwards, The Theory of Polymer Dynamics, Clarendon Press, Oxford, 1986.

[200] R. Granek, M. E. Cates, Stress relaxation in living polymers: Results from a poisson renewal model, J. Chem. Phys. 96 (1992) 4758–4767.

[201] R. H. Ewoldt, A. E. Hosoi, G. H. McKinley, New measures for characterizing nonlinear viscoelasticity in large amplitude oscillatory shear, J. Rheol. 52 (2008) 1427–1458.

[202] R. H. Ewoldt, Defining nonlinear rheological material functions for oscillatory shear, J. Rheol. 57 (2013) 177–195.

[203] A. J. Giacomin, J. M. Dealy, Using large-amplitude oscillatory shear, Springer Netherlands, 1998.

[204] K. Hyun, S. H. Kim, K. H. Ahn, S. J. Lee, Large amplitude oscillatory shear as a way to classify the complex fluids, J. Non-Newtonian Fluid Mech. 107 (2002) 51–65.

[205] A. J. Giacomin, R. B. Bird, L. M. Johnson, A. W. Mix, Large-amplitude oscillatory shear flow from the corotational maxwell model, J. Non-Newtonian Fluid Mech. 166 (2011) 1081–1099.

[206] A. S. K. Gurnon, N. J. Wagner, Large amplitude oscillatory shear (laos) measurements to obtain constitutive equation model parameters: Giesekus model of banding and nonbanding wormlike micelles, J. Rheol. 56 (2012) 333–351.

[207] S. A. Rogers, M. P. Lettinga, A sequence of physical processes determined and quantified in large-amplitude oscillatory shear (laos): Application to theoretical nonlinear models, J. Rheol. 56 (2012) 1–25.

[208] B. C. Blackwell, R. H. Ewoldt, A simple thixotropicviscoelastic constitutive model produces unique signatures in large-amplitude oscillatory shear (LAOS), J. Non-Newtonian Fluid Mech 208 (2014) 27–41.

[209] S. A. Rogers, B. M. Erwin, D. Vlassopoulos, M. Cloitre, A sequence of physical processes determined and quantified in laos: Application to a yield stress fluid, J. Rheol. 55 (2011) 435–458.

[210] S. A. Rogers, A sequence of physical processes determined and quantified in laos: An instantaneous local 2d/3d approach, J. Rheol. 56 (2012) 1129–1151.

[211] J. S. Dodge, I. M. Krieger, Oscillatory shear of nonlinear fluids i. preliminary investigation, Trans. Soc. Rheol. 15 (1971) 589–601.

[212] M. Wilhelm, Fourier-transform rheology, Macromol. Mater. Eng. 287 (2002) 83–105.

[213] B. Debbaut, H. Burhin, Large amplitude oscillatory shear and fourier-transform rheology for a high-density polyethylene: Experiments and numerical simulation, J. Rheol. 46 (2002) 1155–1176.

[214] K. Hyun, J. G. Nam, M. Wilhellm, K. H. Ahn, S. J. Lee, Large amplitude oscillatory shear behavior of peo-ppo-peo triblock copolymer solutions, Rheol. Acta 45 (2006) 239–249.

[215] L. Martinetti, A. M. Mannion, W. E. Voje, R. X. Xie, R. H. Ewoldt, L. D. Morgret, F. S. Bates, C. W. Macosko, A critical gel fluid with high extensibility: The rheology of chewing gum, J. Rheol. 58 (2014) 821–838.

[216] K. Hyun, M. Wilhelm, C. O. Klein, K. S. Cho, J. G. Nam, K. H. Ahn, S. J. Lee, R. H. Ewoldt, G. H. McKinley, A review of nonlinear oscillatory shear tests: Analysis and application of large amplitude oscillatory shear (LAOS), Prog. Polym. Sci. 36 (2011) 1697–1753.

[217] R. H. Ewoldt, N. A. Bharadwaj, Low-dimensional intrinsic material functions for nonlinear viscoelasticity, Rheol. Acta 52 (2013) 201–219.

[218] A. Giacomin, J. Dealy, Large Amplitude Oscillatory Shear, Springer Netherlands, 1993.

[219] T. Neidhöfer, M. Wilhelm, B. Debbaut, Fourier-transform rheology experiments and finite-element simulations on linear polystyrene solutions, J. Rheol. 47 (2003) 1351–1371.

[220] C. Daniel, I. W. Hamley, M. Wilhelm, W. Mingvanish, Non-linear rheology of a face-centred cubic phase in a diblock copolymer gel, Rheol. Acta 40 (2001) 39–48.

[221] A. J. Giacomin, R. B. Bird, Normal stress differences in large-amplitude oscillatory shear flow for the corotational ansr model, Rheol. Acta 50 (2011) 741–752.

[222] P. Stepanek, J. Jakes, C. Konak, R. Johnsen, W. Brown, Dynamic light scattering measurements on the polystyrene/ethyl acetate system at semi-dilute concentrations as a function of temperature, Polym. Bull. 18 (1987) 175–182.

[223] N. Nemoto, M. Kuwahara, Dynamic light scattering of CTAB/sodium salicylate long threadlike micelles in the semidilute regime: applicability of the dynamic scaling law, Langmuir 9 (1993) 419–423.

[224] N. Nemoto, M. Kuwahara, Self diffusion and viscoelasticity of elongated micelles from cetyltrimethyl-ammonium bromide in aqueous sodium salicylate solution. ii. temperature effect, Colloid. Polym. Sci. 272 (1994) 846–854.

[225] N. Nemoto, M. Kuwahara, M. L. Yao, K. Osaki, Dynamic light scattering of CTAB/NaSal threadlike micelles in a semidilute regime. 3. dynamic coupling between concentration fluctuation and stress, Langmuir 11 (1995) 30–36.

[226] E. Buhler, C. Oelschlaeger, G. Waton, S. J. Candau, Viscoelastic properties of hydrocarbon/fluorocarbon mixed wormlike micelles at high ionic strength, J. Phys. Chem. B 108 (2004) 11236–11243.

[227] G. Garg, P. A. Hassan, S. K. Kulshreshtha, Dynamic light scattering studies of rod-like micelles in dilute and semi-dilute regime, Colloids Surf., A 275 (2006) 161–167.

[228] H. Q. Yin, Y. Y. Lin, J. B. Huang, Microstructures and rheological dynamics of viscoelastic solutions in a catanionic surfactant system, J. Colloid Interface Sci. 338 (2009) 177–183.

[229] D. E. Koppel, Analysis of macromolecular polydispersity in intensity correlation spectroscopy: The method of cumulants, J. Chem. Phys. 57 (1972) 4814–4820.

[230] S. W. Provencher, A fourier method for the analysis of exponential decay curves, Biophys. J. 16 (1976) 27–29.

[231] S. W. Provencher, An eigenfunction expansion method for the analysis of exponential decay curves, J. Chem. Phys. 64 (1976) 2772–2777.

[232] A. Khatory, F. Lequeux, F. Kern, S. J. Candau, Linear and nonlinear viscoelasticity of semidilute solutions of wormlike micelles at high salt content, Langmuir 9 (1993) 1456–1464.

[233] M. M. Britton, R. W. Mair, R. K. Lambert, P. T. Callaghan, Transition to shear banding in pipe and couette flow of wormlike micellar solutions, J. Rheol. 43 (1999) 897–909.

[234] R. L. Moorcroft, S. M. Fielding, Shear banding in time-dependent flows of polymers and wormlike micelles, J. Rheol. 58 (2014) 103–47.

[235] C. Grand, J. Arrault, M. Cates, Slow transients and metastability in wormlike micelle rheology, J. Phys. II France 7 (1997) 1071–1086.

[236] M. E. Cates, Nonlinear viscoelasticity of wormlike micelles (and other reversibly breakable polymers), J. Phys. Chem. 94 (1990) 371–375.

[237] T. Shikata, H. Hirata, E. Takatori, K. Osaki, Nonlinear viscoelastic behavior of aqueous detergent solutions, J. Non-Newtonian Fluid Mech. 28 (1988) 171–82.

[238] Y. X. Han, Y. J. Feng, H. Q. Sun, Z. Q. Li, Y. G. Han, H. Y. Wang, Wormlike micelles formed by sodium erucate in the presence of a tetraalkylammonium hydrotrope, J. Phys. Chem. 115 (2011) 6893–6902.

[239] M. E. Helgeson, P. A. Vasquez, E. W. Kaler, N. J. Wagner, Rheology and spatially resolved structure of cetyltrimethylammonium bromide wormlike micelles through the shear banding transition, J. Rheol. 53 (2009) 727–56.

[240] M. E. Helgeson, M. D. Reichert, Y. T. Hu, N. J. Wagner, Relating shear banding, structure, and phase behavior in wormlike micellar solutions, Soft Matter 5 (2009) 3858–69.

[241] M. A. Fardin, T. Divoux, M. A. Guedeau-Boudeville, I. Buchet-Maulien, J. Browaeys, G. H. McKinley, S. Manneville, S. Lerouge, Shear-banding in surfactant wormlike micelles: elastic instabilities and wall slip, Soft Matter 8 (2012) 2535–53.

[242] Y. Y. Lu, L. J. An, S. Q. Wang, Z. G. Wang, Origin of stress overshoot during startup shear of entangled polymer melts, ACS Macro Lett. 3 (2014) 569–573.

[243] Y. Hu, C. Palla, A. Lips, Comparison between shear banding and shear thinning in entangled micellar solutions, J. Rheol. 52 (2008) 379–400.

[244] A. K. Gurnon, C. R. López-Barrón, A. P. R. Eberle, L. Porcar, N. J. Wagner, Spatiotemporal stress and structure evolution in dynamically sheared polymer-like micellar solutions, Phys. Rev. Lett. 110 (2013) 086001.

[245] C. R. López-Barrón, A. K. Gurnon, A. P. R. Eberle, L. Porcar, N. J. Wagner, Microstructural evolution of a model, shear-banding micellar solution during shear startup and cessation, Phys. Rev. E 89 (2014) 042301.

[246] J. Mewis, N. J. Wagner, Thixotropy, Adv. Colloid Interface Sci. 147 (2009) 214–227.

[247] R. B. Bird, B. D. Marsh, Viscoelastic hysteresis. part i. model predictions, Trans. Soc. Rheol. 12 (1968) 479–488.

[248] T. Divoux, V. Grenard, S. Manneville, Rheological hysteresis in soft glassy materials, Phys. Rev. Lett. 110 (2013) 018304. doi:10.1103/PhysRevLett.110.018304.

[249] J. Yoon, C, S. D. Heister, O. H. Campanella, Modeling gelled fluid flow with thixotropy and rheological hysteresis effects, Fuel 128 (2014) 467–475.

[250] S. T. Milner, T. C. B. McLeish, Reptation and contour length fluctuations in melts of linear polymers, Phys. Rev. Lett. 85 (1998) 725–728.

[251] S. T. Milner, T. C. B. McLeish, A. E. Likhtman, Microscopic theory of convective constraint release, J. Rheol. 45 (2001) 539–563.

[252] G. Ianniruberto, G. Marrucci, A multimode ccr model for entangled polymers with chain stretch, J. Non-Newtonian Fluid Mech 102 (2002) 383–395.

[253] R. S. Graham, A. E. Likhtman, T. C. B. McLeish, S. T. Milner, Microscopic theory of linear, entangled polymer chains under rapid deformation including chain stretch and convective constraint release, J. Rheol. 47 (2003) 1171–1200.

[254] F. Da Cruz, F. Chevoir, D. Bonn, P. Coussot, Viscosity bifurcation in granular materials, foams, and emulsions, Phys. Rev. E 66 (2002) 051305.

[255] P. Tapadia, S. Q. Wang, Nonlinear flow behavior of entangled polymer solutions: yield like entanglement-disentanglement transition, Macromolecules 37 (2004) 9083–9095.

[256] P. Tapadia, S. Q. Wang, Direct visualization of continuous simple shear in non-newtonian polymeric fluids, Phys. Rev. Lett. 96 (2006) 016001.

[257] S. Q. Wang, Y. Y. Wang, S. W. Cheng, X. Li, X. Y. Zhu, H. Sun, New experiments for improved theoretical description of nonlinear rheology of entangled polymers, Macromolecules 46 (2013) 3147–3159. doi:10.1021/ma300398x.

[258] C. J. Dimitriou, L. Casanellas, O. T. J., G. H. McKinley, Rheo-piv of a shear-banding wormlike micellar solution under large amplitude oscillatory shear, Rheo. Acta 51 (2012) 395–411.

[259] A. N. Morozov, W. van Saarloos, An introductory essay on subcritical instabilities and the transition to turbulence in visco-elastic parallel shear flows, Phys. Rep. 447 (2007) 112–143.

[260] M. Ouchi, T. Takahashi, M. Shirakashi, Shear-induced structure change and flow-instability in start-up couette flow of aqueous, wormlike micelle solution, J. Rheol. 50 (2006) 341–352.

[261] T. Takahashi, D. Sakata, Flow-induced structure change of CTAB/NaSal aqueous solutions in step planar elongation flow, J. Rheol. 55 (2011) 225–40.

[262] T. Takahashi, N. Yako, M. Shirakashi, Relationship between shear-induced structure and optical anisotropy on cpycl/nasal aqueous solution, Nihon Reoroji Gakkaishi. 29 (2001) 27–32.

[263] T. Takahashi, H. Sugata, M. Shirakashi, Rheo-optic behavior of wormlike micelles under a shear-induced structure formational condition: Verification of stress-optic rule component measurement of refractive index tensor, Nihon Reoroji Gakkaishi. 30 (2002) 109–113.

[264] M. Ouchi, T. Takahashi, M. Shirakashi, Flow-induced structure change and flow-instability of ctab/nasal aqueous solution in a two-dimensional abrupt contract channel,, Nihon Reoroji Gakkaishi. 34 (2006) 229–234.

[265] R. Cressely, R. Hocquart, Biréfringence d'écoulement localisée induite á l'arriere d'obstacles, Optica Acta: International Journal of Optics 27 (1980) 699–711.

[266] G. H. McKinley, R. C. Armstrong, R. A. Brown, The wake instability in viscoelastic flow past confined circular cylinders, Philosophical Transactions: Physical Sciences and Engineering 344 (1993) 265–304.

[267] A. H. Shiang, J. C. Lin, A˙otekin, D. Rockwell, Viscoelastic flow around a confined circular cylinder: measurements using high-image-density particle image velocimetry, J. Non-Newtonian Fluid Mech. 73 (1997) 29 – 49.

[268] A. H. Shiang, A. zkekin, J. C. Lin, D. Rockwell, Hydroelastic instabilities in viscoelastic flow past a cylinder confined in a channel, Exp. Fluids 28 (2000) 128–142.

[269] A. Afonso, M. A. Alves, F. T. Pinho, P. J. Oliveira, Uniform flow of viscoelastic fluids past a confined falling cylinder, Rheol. Acta 47 (2008) 325–348.

[270] A. K. Sankaran, D. A. Dros, H. J. Meerman, S. J. Pickend, M. T. Kreutzer, Increasing the stability of high contraction ratio flow of boger fluids by pre-deformation, J. Non-Newtonian Fluid Mech. 196 (2013) 27–35.

[271] F. Baaijens, S. Selen, H. Baaijens, G. Peters, H. Meijer, Viscoelastic flow past a confined cylinder of a low density polyethylene melt, J. Non-Newtonian Fluid Mech. 68 (1997) 173–203.

[272] A. W. Liu, D. E. Bornside, R. Armstrong, R. Brown, Viscoelastic flow of polymer solutions around a periodic, linear array of cylinders: comparisons of predictions for microstructure and flow fields, J. Non-Newtonian Fluid Mech. 77 (1998) 153190.

[273] Y. Fan, R. Tanner, N. Phan-Thien, Galerkin/least-square finite-element methods for steady viscoelastic flows, J. Non-Newtonian Fluid Mech. 84 (1999) 233–256.

[274] M. Alves, F. Pinho, P. Oliveira, The flow of viscoelastic fluid past a cylinder: finite-volume high-resolution methods, J. Non-Newtonian Fluid Mech. 97 (2001) 207–232.

[275] M. A. Hulsen, R. Fattal, R. Kupferman, Flow of viscoelastic fluids past a cylinder at high weissenberg number: stabilized simulations using matrix logarithms, J. Non-Newtonian Fluid Mech. 127 (2005) 2739.

[276] P. J. Oliveira, A. I. P. Miranda, A numerical study of steady and unsteady viscoelastic flow past bounded cylinders, J. Non-Newtonian Fluid Mech. 127 (2005) 5166.

[277] Y. Zhao, P. Cheung, A. Q. Shen, Microfluidic flows of wormlike micellar solutions, Adv. Colloid Interface Sci.

[278] P. Y. Huang, J. Feng, Wall effects on the flow of viscoelastic fluids around a circular cylinder, J. Non-Newtonian Fluid Mech. 60 (1995) 179–198.

[279] S. Kenney, K. Poper, G. Chapagain, G. Christopher, Large deborah number flows around confined microfluidic cylinders, Rheol. Acta 52 (2013) 485–497.

[280] H. S. Dou, N. Phan-Thien, Viscoelastic flow past a confined cylinder: Instability and velocity inflection, Chem. Eng. Sci. 62 (2007) 3909–3929.

[281] V. M. Ribeiro, P. M. Coelho, F. T. Pinho, M. A. Alves, Viscoelastic fluid flow past a confined cylinder: Three-dimensional effects and stability, Chem. Eng. Sci. 111 (2014) 364 – 380.

[282] L. Campo-Deano, F. J. Galindo-Rosales, F. T. Pinho, M. A. Alves, M. S. N. Oliveira, Nanogel formation of polymer solutions flowing through porous media, Soft Matter 8 (2012) 6445–6453.

[283] J. L. Zakin, B. Lu, H. W. Bewersdorff, Surfactant drag reduction, Rev. Chem. Eng. 14 (1998) 253–320.

[284] P. Pakdel, G. H. McKinley, Elastic instability and curved streamlines, Phys. Rev. Lett. 77 (1996) 2459–2462.

[285] X. Shi, S. Kenney, G. Chapagain, G. F. Christopher, Mechanisms of onset for moderate mach number instabilities of viscoelastic flows around confined cylinders, Rheol. Acta 54 (2015) 805–815.

[286] F. J. Galindo-Rosales, L. Campo-Deano, P. C. Sousa, V. M. Ribeiro, M. Oliveira, M. A. Alves, F. T. Pinho, Viscoelastic instabilities in micro-scale flows, Exp. Therm. Fluid. Sci. 59 (2014) 128–139.

[287] C. L. Sun, H. Y. Huang, Measurements of flow-induced birefringence in microfluidics, Biomicrofluidics 10 (2016) 011903.

[288] Y. Zhao, S. J. Haward, A. Q. Shen, Rheological characterizations of wormlike micellar solutions containing cationic surfactant and anionic hydrotropic salt, J. Rheol. 59 (2015) 1229–1259.

[289] M. I. Kolte, P. Szabo, Capillary thinning of polymeric filaments, J. Rheol. 43 (1999) 609–625.

[290] S. L. Anna, G. H. McKinley, Elasto-capillary thinning and breakup of model elastic liquids, J. Rheol. 45 (2001) 115–138.

[291] Y. Xia, G. M. Whitesides, Soft lithography, Angew. Chem., Int. Ed. 37 (1998) 550575.

[292] C.-Y. Han, Y.-F. Chao, Photoelastic modulated imaging ellipsometry by stroboscopic illumination technique, Rev. Sci. Instrum 77.

[293] S. Nichols, J. Freudenthal, O. Arteaga, B. Kahr, Imaging with photoelastic modulators, Proc. SPIE 9099.

[294] R. D. Keane, R. J. Adrian, Theory of cross-correlation analysis of piv images, Appl. Sci. Res. 49 (1992) 191–215.

[295] S. Wereley, L. Gui, A correlation-based central difference image correction (cdic) method and application in a four-roll mill flow piv measurement, Exp. Fluids 34 (2003) 42–51.

[296] S. J. Haward, J. A. Odell, Molecular orientation in non-newtonian flow of dilute polymer solutions around spheres, Rheol. Acta 43 (2004) 350–363.

[297] M. Cromer, L. P. Cook, G. H. McKinley, Extensional flow of wormlike micellar solutions, Chem. Eng. Sci. 64 (2009) 4588–96.

[298] L. Zhou, L. P. Cook, G. H. McKinley, Probing shear-banding transitions of the VCM model for entangled wormlike micellar solutions using large amplitude oscillatory shear (LAOS) deformations, J. Non-Newtonian Fluid Mech. 165 (2010) 1462–72.

[299] C. J. Pipe, N. J. Kim, P. A. Vasquez, L. P. Cook, G. H. McKinley, Wormlike micellar solutions: II. comparison between experimental data and scission model predictions, J. Rheol. 54 (2010) 881–913.

[300] B. Yesilata, C. Clasen, G. McKinley, Nonlinear shear and extensional flow dynamics of wormlike surfactant solutions, J. Non-Newtonian Fluid Mech. 133 (2006) 73–90.

[301] F. Bautista, J. F. A. Soltero, J. H. Perez-Lopez, J. E. Puig, O. Manero, On the shear banding flow of elongated micellar solutions, J. Non-Newtonian Fluid Mech. 94 (2000) 57–66.

[302] O. Manero, F. Bautista, J. F. A. Soltero, J. Puig, Dynamics of worm-like micelles: the Cox-Merz rule, J. Non-Newtonian Fluid Mech. 106 (2002) 1–15.

[303] O. Manero, J. H. Perez-Lopez, J. I. Escalante, J. E. Puig, F. Bautista, A thermodynamic approach to rheology of complex fluids: The generalized BMP model, J. Non-Newtonian Fluid Mech. 146 (2007) 22–9.

[304] M. Cromer, L. P. Cook, G. H. McKinley, Pressure-driven flow of wormlike micellar solutions in rectilinear microchannels, J. Non-Newtonian Fluid Mech. 166 (2011) 180–93.

[305] M. Kroger, Simple models for complex nonequilibrium fluids, Phys. Rep. 390 (2004) 453–551.

[306] M. Kroger, R. Makhloufi, Wormlike micelles under shear flow: A microscopic model studied by nonequilibrium-molecular-dynamics computer simulations, Phys. Rev. E 53 (1996) 2531–6.

[307] P. D. Olmsted, O. Radulescu, C. Y. D. Lu, Johnson-segalman model with a diffusion term in cylindrical couette flow, J. Rheol. 44 (2000) 257–75.

[308] J. T. Padding, E. S. Boek, Influence of shear flow on the formation of rings in wormlike micelles: A nonequilibrium molecular dynamics study, Phys. Rev. E 70 (2004) 031502–10.

[309] J. T. Padding, E. S. Boek, W. J. Briels, Rheology of wormlike micellar fluids from brownian and molecular dynamics simulations, J. Phys.: Condens. Matter 17 (2005) S3347–53.

[310] L. P. Cook, L. R. Rossi, Slippage and migration in models of dilute wormlike micellar solutions and polymeric fluids, J. Non-Newtonian Fluid Mech. 116 (2004) 347–69.

[311] L. F. Rossi, G. H. McKinley, L. P. Cook, Slippage and migration in Taylor-Couette flow of a model for dilute wormlike micellar solutions, J. Non-Newtonian Fluid Mech. 136 (2006) 79–92.

[312] M. Cromer, P. L. Cook, G. H. McKinley, Interfacial instability of pressure-driven channel flow for a two-species model of entangled wormlike micellar solutions, J. Non-Newtonian Fluid Mech 166 (2011) 566–77.

[313] M. E. Cates, S. M. Fielding, Rheology of giant micelles, Adv. Phys. 55 (2006) 799–879.

[314] S. J. Haward, J. A. Odell, Z. Li, X. F. Yuan, Extensional rheology of dilute polymer solutions in oscillatory cross-slot flow: the transient behavior of birefringent strands, Rheol. Acta 49 (2010) 633–45.

[315] L. Xi, M. D. Graham, A mechanism for oscillatory instability in viscoelastic cross-slot flow, J. Fluid Mech. 622 (2009) 145–65.

[316] G. N. Rocha, R. J. Poole, M. A. Alves, P. J. Oliveira, On extensibility effects in the cross-slot flow bifurcation, J. Non-Newtonian Fluid Mech. 156 (2009) 58–69.

[317] M. S. N. Oliveira, F. T. Pinho, R. J. Poole, P. J. Oliveira, M. A. Alves, Purely elastic flow asymmetries in flow-focusing devices, J. Non-Newtonian Fluid Mech 160 (2009) 31–9.

[318] M. S. N. Oliveira, L. E. Rodd, G. H. McKinley, M. A. Alves, Simulations of extensional flow in microrheometric devices, Microfluid and Nanofluidics 5 (2008) 809–26.

[319] G. H. McKinley, L. E. Rodd, M. S. N. Oliverira, J. Cooper-White, Extensional flows of polymer solutions in microfluidic converging/diverging geometries, J. Cent. South Univ. Technol. 14 (2007) 6–9.

[320] E. S. Boek, J. T. Padding, V. J. Anderson, P. M. J. Tardy, J. P. Crawshaw, J. R. A. Pearson, Constitutive equations for extensional flow of wormlike micelles: stability analysis of the bautistamanero model, J. Non-Newtonian Fluid Mech 126 (2005) 39–46.

[321] A. Milchev, J. P. Wittmer, D. P. Landau, A Monte-Carlo study of equilibrium polymers in a shear flow, Eur. Phys. J. B, 12 (1999) 241–51.

[322] P. A. Stone, S. D. Hudson, P. Dalhaimer, D. E. Discher, E. J. Amis, K. B. Migler, Dynamics of wormlike micelles in elongational flows, Macromolecules 39 (2006) 7144–8.

[323] R. Barrett, M. Faucon, J. Lopez, G. Cristobal, F. Destremaut, A. Dodge, P. Guillot, P. Laval, C. Masselon, J. B. Salmon, X-ray microfocussing combined with microfluidics for on-chip x-ray scattering measurements, Lab Chip 6 (2006) 494–9.

[324] L. C. Pan, P. E. Arratia, A high-shear, low reynolds number microfluidic rheometer, Microfluid and Nanofluidics 14 (2013) 885–94.

[325] Z. L. Chu, C. A. Dreiss, Y. Feng, Smart wormlike micelles, Chem. Soc. Rev. 42 (2013) 7174–203.

[326] A. Matsumura, K. Sakai, H. Sakai, M. Abe, Photoinduced increase in surfactant solution viscosity using azobenzene dicarboxylate for molecular switching, J. Oleo Sci. 60 (2011) 203–7.

[327] H. Sakai, Y. Orihara, H. Kodashima, A. Matsumura, T. Ohkubo, K. Tsuchiya, M. Abe, Photoinduced reversible change of fluid viscosity, J. Am. Chem. Soc. 127 (2005) 13454–5.

[328] H. Sakai, S. Taki, K. Tsuchiya, A. Matsumura, K. Sakai, M. Abe, Photochemical control of viscosity using sodium cinnamate as a photoswitchable molecule, Chem. Lett. 41 (2012) 247–8.

[329] H. Azzouzi, J. P. Decruppe, S. Lerouge, O. Greffier, Temporal oscillations of the shear stress and scattered light in a shear-banding-shear-thickening micellar solution, Eur. Phys. J. E, 17 (2005) 507–14.

[330] Y. T. Hu, P. Boltenhagen, D. J. Pine, Shear thickening in low-concentration solutions of wormlike micelles. i. direct visualization of transient behavior and phase transitions, J. Rheol. 42 (1998) 1185–208.

[331] I. A. Kadoma, J. W. van Egmond, Flow-induced nematic string phase in semidilute wormlike micelle solutions, Phys. Rev. Lett. 80 (1997) 5679–82.

[332] I. A. Kadoma, C. Ylitalo, J. W. vanEgmond, Structural transitions in wormlike micelles, Rheol. Acta 36 (1997) 1–12.

[333] I. A. Kadoma, J. W. vanEgmond, Shear-enhanced orientation and concentration fluctuations in wormlike micelles: Effect of salt, Langmuir 13 (1997) 4551–61.

[334] L. M. Walker, P. Moldenaers, J. F. Berret, Macroscopic response of wormlike micelles to elongational flow, Langmuir 12 (1996) 6309–14.

[335] I. A. Kadoma, J. W. vanEgmond, "tuliplike" scattering patterns in wormlike micelles under shear flow, Phys. Rev. Lett. 76 (1996) 4432–5.

[336] V. Schmitt, F. Lequeux, A. Pousse, D. Roux, Flow behavior and shear-induced transition near an isotropic-nematic transition in equilibrium polymers, Langmuir 10 (1994) 955–61.

[337] R. F. Day, H. A. Stone, Lubrication analysis and boundary integral simulations of a viscous micropump, J. Fluid Mech. 416 (2000) 197–216.

[338] H. A. Barnes, J. F. Hutton, K. Walters, An introduction to Rheology, Elsevier, Amsterdam, 1989.

[339] H. Rehage, I. Wunderlich, H. Hoffmann, Shear induced phase transitions in dilute aqueous surfactant solutions, Prog. Colloid Polym. Sci. 72 (1985) 51–59.

[340] A. E. Likhtman, R. S. Graham, Simple constitutive equation for linear polymer melts derived from molecular theory: Rolie-poly equation, J. Non-Newtonian Fluid Mech. 114 (2003) 1–12.

[341] R. Moorcroft, S. M. Fielding, Criteria for shear banding in time-dependent flows of complex fluids, Phys. Rev. Lett. 110 (2013) 086001.

[342] J. M. Adams, P. D. Olmsted, Nonmonotonic models are not necessary to obtain shear banding phenomena in entangled polymer solutions, Phys. Rev. Lett. 102 (2009) 067801.

[343] J. M. Adams, S. M. Fielding, P. D. Olmsted, Transient shear banding in entangled polymers: a study using the rolie-poly model, J. Rheol. 5 (2011) 1007–32.

[344] P. Boltenhagen, Y. T. Hu, E. F. Matthys, D. J. Pine, Inhomogeneous structure formation and shear-thickening in worm-like micellar solutions, Europhys. Lett. 38 (1997) 389–94.

[345] J.-F. Berret, R. Gamez-Corrales, J. Oberdisse, L. M. Walker, P. Lindner, Flow-structure relationship of shear-thickening surfactant solutions, Europhys. Lett. 41 (1998) 677–82.

[346] C. Barentin, A. J. Liu, Shear thickening in dilute solutions of wormlike micelles, Europhys. Lett. 55 (2001) 432–8.

[347] Y. T. Hu, S. Q. Wang, A. M. Jamieson, Rheological and flow birefringence studies of a shear thickening complex fluid: A surfactant model system, J. Rheol. 37 (1993) 531–46.

[348] I. Wunderlich, H. Hoffmann, H. Rehage, Flow birefringence and rheological measurements on shear induced micellar structures, Rheol. Acta 26 (1987) 532–42.

[349] R. Oda, P. Panizza, M. Schmutz, F. Lequeux, Direct evidence of the shear-induced structure of wormlike micelles: Gemini surfactant 12-2-12, Langmuir 13 (1997) 6407–12.

[350] B. Lu, X. Li, L. E. Scriven, H. T. Davis, Y. Talmon, J. L. Zakin, Effect of chemical structure on viscoelasticity and extensional viscosity of drag-reducing cationic surfactant solutions, Langmuir 14 (1998) 8–16.

[351] M. T. Truong, L. M. Walker, Quantifying the importance of micellar microstructure and electrostatic interactions on the shear-induced structural transition of cylindrical micelles, Langmuir 18 (2002) 2024–31.

[352] R. Oda, V. Weber, P. Lindner, D. J. Pine, E. Mendes, F. Schosseler, Time-resolved small-angle neutron scattering study of shear-thickening surfactant solutions after the cessation of flow, Langmuir 16 (2000) 4859–63.

[353] V. Schmitt, F. Schosseler, F. Lequeux, Structure of salt-free wormlike micelles: Signature by sans at rest and under shear, Europhys. Lett. 30 (1995) 31–6.

[354] R. Bandyopadhyay, A. K. Sood, Chaotic dynamics in shear-thickening surfactant solutions, Europhys. Lett. 56 (2001) 447–53.

[355] B. M. Marín-Santibánez, J. Pérez-González, L. de Vargas, F. Rodríguez-González, G. Huelsz, Rheometry-PIV of shear-thickening wormlike micelles, Langmuir 22 (2006) 4015–26.

[356] D. P. Acharya, H. Kunieda, Wormlike micelles in mixed surfactant solutions, Adv. Colloid Interface Sci. 123 (2006) 401–413.

[357] T. Lu, J. B. Huang, Z. H. Li, S. K. Jia, H. L. Fu, Effect of hydrotropic salt on the assembly transitions and rheological responses of cationic gemini surfactant solutions., J. Phys. Chem. B 112 (2008) 2909–2914.

[358] K. V. Padalkar, O. R. Pal, V. G. Gaikar, Rheological characterization of mixtures of cetyl trimethylammonium bromide and sodium butyl benzene sulfonate in aqueous solutions, J. Mol. Liq. 173 (2012) 18–28.

[359] P. A. Hassan, S. R. Raghavan, E. W. Kaler, Microstructural changes in SDS micelles induced by hydrotropic salt., Langmuir 18 (2002) 2543–2548.

[360] S. R. Raghavan, E. W. Kaler, Highly viscoelastic wormlike micellar solutions formed by cationic surfactants with long unsaturated tails, Langmuir 17 (2001) 300–306.

[361] V. Croce, T. Cosgrove, G. Maitland, T. Hughes, G. Karlsso, Rheology, cryogenic transmission electron spectroscopy, and small-angle neutron scattering of highly viscoelastic wormlike micellar solutions, Langmuir 20 (2003) 8536–8541.

[362] T. Nash, The interaction of some naphthalene derivatives with a cationic soap below the critical micelle concentration, J. Colloid Interface Sci. 13 (1958) 134–139.

[363] C. Oelschlaeger, P. Suwita, N. Willenbacher, Effect of counterion binding efficiency on structure and dynamics of wormlike micelles, Langmuir 26 (2010) 7045–7053.

[364] T. Shikata, H. Hirata, E. Takatori, K. Osaki, Nonlinear viscoelastic behavior of aqueous detergent solutions, J. Non-Newtonian Fluid Mech. 28 (1988) 171–182.

[365] H. Z. Cummins, E. R. Pike, Photon Correlation and Light Beating Spectroscopy, Plenum Press, New York, 1985.

[366] M. Grosso, P. L. Maffettone, Fourier Transforms - New Analytical Approaches and FTIR Strategies"-Chapter 14 : Fourier Transform Rheology: A New Tool to Characterize Material Properties, InTech, 2011.

[367] K. Bijma, J. B. F. N. Engberts, Effect of counterions on properties of micelles formed by alkylpyridinium surfactants. 1. conductometry and h-nmr chemical shifts, Langmuir 1997 (1997) 4843–4849.

[368] K. Bijma, E. Rank, J. B. F. N. Engberts, Effect of counterion structure on micellar growth of alkylpyridinium surfactants in aqueous solution, J. Colloid Interface Sci. 205 (1998) 245–256.

[369] D. Balasubramanian, V. Srinivas, V. G. Gaikar, M. M. Sharma, Aggregation behavior of hydrotropic compounds in aqueous solution, J. Phys. Chem. 93 (1989) 3865–3870.

[370] J.-F. Berret, Rheology of Wormlike Micelles: Equilibrium Properties and Shear Banding Transitions, Springer Netherlands, 2006.

[371] D. W. Mead, R. G. Larson, M. Doi, A molecular theory for fast flows of entangled polymers, Macromolecules 31 (1998) 7895–7914.

[372] M. Smith, Y. L. Joo, R. C. Armstrong, R. A. Brown, Linear stability analysis of flow of an oldroyd-b fluid through a linear array of cylinders, J. Non-Newtonian Fluid Mech. 109 (2003) 13–50.

[373] M. Grilli, A. Vázquez-Quesada, M. Ellero, Transition to turbulence and mixing in a viscoelastic fluid flowing inside a channel with a periodic array of cylindrical obstacles, Phys. Rev. Lett. 110 (2013) 174501.

[374] S. Kefi, J. Lee, T. Pope, P. Sullivan, E. Nelson, A. Hernandez, T. Olsen, M. Parlar, B. Powers, A. Roy, A. Wilson, A. Twynam, Expanding applications for viscoelastic surfactants, Oileld Review (2004) 10–16.

[375] O. G. Harlen, The negative wake behind a sphere sedimenting through a viscoelastic fluid, J. Non-Newtonian Fluid Mech. 108 (2002) 411 – 430.

[376] S. Majumdar, A. K. Sood, Universality and scaling behavior of injected power in elastic turbulence in wormlike micellar gel, Phys. Rev. E 84 (2011) 015302.

[377] C. Perge, M. A. Fardin, S. Manneville, Surfactant micelles: Model systems for flow instabilities of complex fluids, Eur. Phys. J. E 37.

[378] E. Groisman, V. Steinberg, Elastic turbulence in a polymer solution flow, Nature 405 (2000) 53–55.

[379] P. Sousa, P. Coelho, M. Oliveira, M. Alves, Effect of the contraction ratio upon viscoelastic fluid flow in three-dimensional squaresquare contractions, Chem. Eng. Sci. 66 (2011) 998–1009.